

Novel Synthetic Strategy and Reagents for the Synthesis of Gold Nanoparticles and Catalytically Active Fe₃O₄@M (M = Au, Ag, Pd and AuAg alloy) Core-Shell Nanostructures

THESIS

Submitted in partial fulfilment
of the requirements for the degree of

DOCTOR OF PHILOSOPHY

By
NALLURI SRINIVASA RAO
ID. No. 2012PHXF0501H

Under the Supervision of

Dr. BALAJI GOPALAN



BIRLA INSTITUTE OF TECHNOLOGY AND SCIENCE, PILANI

April , 2021

BIRLA INSTITUTE OF TECHNOLOGY AND SCIENCE, PILANI

CERTIFICATE

This is to certify that the thesis titled **Novel Synthetic Strategy and Reagents for the Synthesis of Gold Nanoparticles and Catalytically Active Fe₃O₄@M (M = Au, Ag, Pd and AuAg alloy) Core-Shell Nanostructures**

submitted by **_NALLURI SRINIVASA RAO_** ID No **2012PHXF0501H_** for award of Ph.D. of the Institute embodies original work done by him/her under my supervision.



Signature of the Supervisor:

Name in capital letters: Dr. BALAJI GOPALAN

Designation: ASSISTANT PROFESSOR

Date: 19.04.2021

Abstract

Since the seminal work of Haruta and Hutchings in late 80s, gold catalysis has become very important. And on the other hand, a plethora of synthetic modifications for the preparation gold nanoparticles emerged. The understanding of nucleation and growth mechanism has led also to other gold nanostructures like twinned and anisotropic gold nanomaterials. However, the search for novel reducing agents have been an on-going process. From functionality perspective, core-shell nanoparticles has taken a special place. In state of the art research, the wet-chemical methods involve involves the coating of shell materials on the pre-formed core. Although, the mechanism is well understood, the large scale synthesis and use of harmful solvents cannot be avoided. Thus, new reagents and synthetic strategy are required which can address some issues in the existing methods.

In the first chapter, basic concepts of nanoscience and an overview of synthetic procedures for the preparation of gold nanosystems and core-shell nanomaterials are discussed. The properties and application of such materials in general have also have been highlighted. In the chapter 2, the reagents and chemicals used for the synthesis and applications are given. Various analytical instruments that were utilized for the characterization of materials have also been listed in this chapter.

We hypothesized that those organic molecules can lose H moieties in order to achieve aromaticity can be a good reducing agent for gold salts. In chapter 3, we present the results of gold nanoparticle synthesis. For the Au nanoparticle synthesis, three hydrocarbon molecules were used reducing agents for Au^{3+} ions in aqueous medium. The hydrocarbon molecules used are cycloheptatriene, 1,2 hexadiene and 1,4 hexadiene. The Au nanoparticle synthesis were carried out at room temperature. The synthetic procedure was optimized for the molar ratio of reducing agent to Au^{3+} as 3:1. The products were characterized by XRD, TEM, UV-Vis and NMR instrumental techniques. The results indicated that there is a difference in the reactivity between the molecules studied. The cycloheptatriene molecule reduced Au^{3+} ions with in a duration of 3 minutes, leading to the formation of red color which a typical color is observed aqueous Au nanoaparticle solution. The reducing agent molecule attain aromaticity by converting to tropylium ion which was confirmed from ^1H NMR. Besides, the formed tropylium ion also acts as a weak stabilizer yielding red colored twinned Au nanoparticles

which was confirmed by XRD and TEM. The other two molecules showed a weak reactivity- by appearance of a pale blue color in the reactant solution in approximately 8 min reaction duration.

Core-shell nanoparticles were prepared by using a solvent-less solid-state approach. We hypothesized that a surfactant based precursor coated on a preformed core followed by high temperature heat-treatment would yield core-shell nanoparticles. In chapter 4, we have demonstrated successful formation of $\text{Fe}_3\text{O}_4@Au$ nanostructures. Gold tetraoctylammonium bromide surfactant-based precursor (Au-TOAB) was prepared by using the procedure reported in the literature. The Au-TOAB precursor was coated onto the Fe_3O_4 purchased commercially. The melting point of the precursor is 50°C . And so this feature enables a smooth coating of precursor during solid-state grinding. The grinding was performed for 10 min. On heating at 250°C for 2 h in autoclave, the precursor decomposes and result in melting, thereby enabling the coating of Au shell. The Au in the shell do not ball-up due to the presence of alkyl chain surfactant which reduces the surface energy of the melt resulting in the smooth coverage. This was confirmed when the samples were quenched from 250°C . A wavy features rather than a smooth surface supports our explanation. The important salient features of this procedure is the composition is governed by the initial precursor to Fe_3O_4 feed ratio. The initial content of the precursor was varied from 10 mg to 40 mg by keeping the core weight as 100 mg. The as-synthesized $\text{Fe}_3\text{O}_4@Au$ were characterized by ED-XRF, XRD, BET, XPS, FE-SEM, HRTEM, STEM and SAXS. To exhibit the applicability of the method, $\text{SiO}_2@Au$ was also prepared by using the same gold precursor. A clear Au shell of thickness $\sim 5\text{-}9$ nm was formed which was confirmed by STEM results. And in XRD, the intensity of Au (111) plane for Au increased with increasing Au content, the uniformity of thickness of the shell layer could not be controlled. While, a local variation of shell thickness may present, the average increase in thickness with increasing Au amount can be confirmed from SAXS results.

We applied the solvent-less solid-state approach for the synthesis of $\text{Fe}_3\text{O}_4@Ag$ nanostructures. In chapter 5, we have demonstrated successful formation of $\text{Fe}_3\text{O}_4@Au$ nanostructures. Silver N-Lauryl sarcosinate(Ag-NLS) surfactant-based precursor was prepared in the lab and was used as precursor. The melting point of the precursor is 60°C . And so this feature enables a smooth coating of precursor on the commercial Fe_3O_4 during solid-state grinding. The solid-state grinding was carried out for 10 min. The resultant mixture was heated at 250°C for 2 h in an autoclave. During the heat-treatment, the precursor decomposed and

resulted in smooth formation of Ag shell. The thickness of the Ag was ~ 5 nm which was smooth when compared to the Au counterpart. Ag shell do not ball-up like Au due lower surface energy and slight surface oxidation. The initial content of the precursor was varied from 10 mg to 40 mg by keeping the core weight as 100 mg. Similar to results presented in chapter 4, the as-synthesized $\text{Fe}_3\text{O}_4@\text{Ag}$ were characterized by ED-XRF, XPS, BET, XRD, FE-SEM. HRTEM, STEM and SAXS. To exhibit the applicability of the method, $\text{SiO}_2@\text{Ag}$ was also prepared by using the same silver precursor. A clear Ag shell formation was confirmed by STEM results and in XRD, the intensity of Ag (111) plane for Au increased with increasing Ag content while the uniformity of thickness of the shell layer could not be controlled. A local variation of shell thickness was present, however, the average increase in thickness with increasing Ag amount can be confirmed from interpretation of SAXS results.

In chapter 6, we present the results of AuAg alloy shell formation over commercially purchased Fe_3O_4 sample. The alloy composition was changed by varying the weight ratio of Au and Ag precursor in the initial feed. We have used Au-TOAB and Ag-NLS as precursor for Au and Ag respectively. A known amount of precursors was added to Fe_3O_4 and the resultant mixture was grounded for 10 min and followed by the heat-treatment at 250 °C for 2 h in an autoclave. Despite the presence of Au the surface of the alloy shell was smooth indicating the properties of Ag dominates due to surface oxidation. Similar to results presented in chapter 4 and 5, we found a variable thickness in the samples. Both ED-XRF and SAXS results were found to be sensitive to the composition. In SAXS, especially at higher “q”, intensity was less when the gold content was increased. To determine whether shell formation depends on composition and shape of the core, $\text{SiO}_2@\text{Ag-Au}$ nanostructures were also prepared. In XRD, the position of (111) plane was dependent on the composition of the alloys thus confirming the successful preparation of core-shell nanostructures and the applicability of solid-state approach to various core and shell materials.

Ammonia borane is an important molecule in green and sustainable hydrogen storage. In chapter 7, we present the catalytic H_2 generation from ammonia borane using the as-synthesized catalysts. The rate of H_2 generation was found to be higher when a combination of sodium borohydride and ammonia borane was used. The kinetic parameters for H_2 generation have been determined. The catalytic activity of silver and silver-rich catalysts showed better catalytic activity. In the case of alloys, the rate of hydrogen generation with all the alloy catalysts

remained almost constant throughout the reaction, which was not the case with pure Ag catalyst that slowed down towards the end of the reaction. The leaching was attributed to the formation of $\text{Ag}[(\text{NH}_3)_2]^+$ complex. From the sustainable perspective, magnetic recoverability was also demonstrated due the presence of magnetic Fe_3O_4 core. The recycled catalyst was characterized by ED-XRF, XRD, FE-SEM, and HR-TEM. However, on increasing the recycle, the catalytic activity was found to reduce due to the formation of polyborazylene by-product. This was evident from the FE-SEM images. The saturation magnetization of Fe_3O_4 decreased from its pristine value on addition of Au, Ag and AuAg shell due to diamagnetic nature of the noble metal shells.

Chapter 8 deals with the synthesis, characterization and catalytic activity studies of $\text{Fe}_3\text{O}_4@\text{Pd}$ nanostructures prepared by solid state approach using a non-surfactant precursor. Palladium acetate was mixed with Fe_3O_4 core and grounded for 10 min. The resultant mixture was heat-treated at 250 °C for 2 h in an autoclave. The as-synthesized $\text{Fe}_3\text{O}_4@\text{Pd}$ were characterized by XPS, BET, XRD, FE-SEM. HRTEM. The FE-SEM results indicated that at low Pd loading, Pd was dispersed as nanoislands on the surface of Fe_3O_4 whose number density increased with increasing Pd loading. Interestingly, the coalescence of Pd was not observed. Only at relatively higher Pd loading, coalescence Pd to form shell-like feature was observed. A heat treatment was required to the complete shell formation. HR-TEM showed an amorphous layer which was assigned to $\alpha\text{-Fe}_2\text{O}_3$ layer on the surface of Fe_3O_4 due to the metal-support interaction. XRD results corroborated the formation of Fe_2O_3 phase. The heat-treatment at 900 °C lead to complete mixing of core and shell aspects of nanosystems. The catalytic efficacy of $\text{Fe}_3\text{O}_4@\text{Pd}$ was studied for 4-nitrophenol reduction. Magnetic recoverability of the catalysts was also demonstrated.

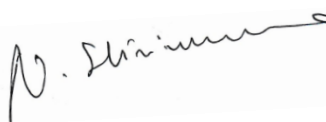
The conclusions of this work and the future scope of the present work are discussed in chapter 9.

BIRLA INSTITUTE OF TECHNOLOGY AND SCIENCE, PILANI

DECLARATION

I hereby declare that the thesis entitled **Novel Synthetic Strategy and Reagents for the Synthesis of Gold Nanoparticles and Catalytically Active $\text{Fe}_3\text{O}_4@M$ ($M = \text{Au, Ag, Pd}$ and AuAg alloy) Core-Shell Nanostructures**, is conducted under the supervision of Prof. Dr. BALAJI GOPALAN, Department of Chemistry, Birla Institute of Technology and Science-Pilani, Hyderabad Campus.

I also declare that this thesis represents my own work which has been done after registration for the degree of Ph.D. at Birla institute of Technology and Science-Pilani, Hyderabad Campus, and has not been previously included in any thesis or dissertation submitted to this or any other institution for a degree, diploma or other qualifications.

Signature: 

Name: Nalluri Srinivasa Rao

Date: 19th April 2021

Place: Hyderabad

Acknowledgements

It is a pride moment to show the gratification with a sense of pleasure at the long travelled journey, to be able to recapture some of the fine moments and to be able to thank some of whom were with me from the beginning, some who joined me at some stage during the journey, whose rally round kindness, love, and blessings have brought me to this day. I wish to thank each and every one of them with all my heart.

Foremost, I owe thanks to a very special person, my supervisor, Dr. Balaji Gopalan for his continuous support of my Ph.D. study and research, for his enormous patience, motivation, enthusiasm, and immense knowledge. I consider myself fortunate to be associated with him who gave a decisive turn and a significant boost to my career. His valuable guidance helped me in all the time of my research and writing of this thesis.

I would like to thank many people who helped me in this entire tenure of my Ph.D. with their valuable time, suggestions and encouragement. I am thankful to acknowledge my doctoral advisory committee (DAC) members, Prof. Krishnan Rangan and Prof. Kannan Ramaswamy for their tremendous support and encouragement during this period. I thank DRC convener, Dr. Durba Roy and former DRC convenor, Prof. Jayanthi Subbalakshmi for their valuable suggestions.

I am thankful to Head of the Department (HOD), Prof. Sounak Roy, and previous Head Prof. Manab Chakravarty, Prof. Anupam Bhattacharya and entire chemistry department faculty members for their valuable interaction and discussions throughout the journey. I sincerely acknowledge Prof. Ramakrishnan Ganesan for his remarkable support and inputs to carry out the research.

I am grateful to vice-chancellor Prof. Souvik Bhattacharyya of BITS Pilani, former director Prof. V. S. Rao and Prof. G Sundar, present director of BITS Pilani Hyderabad Campus for giving me an opportunity to pursue and to carry out my Doctoral research work.

I would like to express my sincere thanks to Prof. V. V. Vamshi Krishna, Dean, Academic-Graduate Studies and Research Division (Ph.D. Programme) and former dean Prof. Vidya Rajesh for their continuous support and encouragement during my research work. And I extend my thanks to Mr. Praveen, AGSRD for his help and information to complete the course formalities in time.

My sincere thanks to BITS Pilani Hyderabad Campus for providing financial assistance in the form of institute fellowship.

I am truly grateful to my friends, Dr. Ravikiran Nagarjuna, Mr. Dinabandhu Patra, who have unconditionally helped me during various stages of my work. I would like to thank my ex-lab mate Dr. Sathish for his support.

I thank chemistry department non-teaching staff Mr. Ashok, Mr. Sudheer, Mr. Gangadar and Mrs. Shanti and Central Analytical Lab (CAL) technicians Mr. Mallesh, Mr. Upalayya for their excellent cooperation throughout my research work.

I sincerely acknowledge the research scholars in chemistry and other departments for the time they had spent for me and making my stay at campus a memorable one. I take this opportunity to thank one and all who helped me directly or indirectly.

My heart felt regards goes to my parents late Mr. yallamandiah and Mrs. Kamalama who have given their blessings for the great desire to see me succeed and get the highest degree in education. I must specially thank my wife, assistsnt professor Mrs. Sharmila sure for the support and encouragement which helped me in keeping my moral high and daughterMs. Kavaya and my son Master karthik for giving joyful environment. I would like to do that by dedicating this thesis to my family. Special thanks to my uncle justice Ananda Reddy garu and my aunty Nirmala garu who are standing beside me with their love and unconditional support. I really consider myself the luckiest in the world to have such a lovely and caring family.

I thank the Almighty, The Lord Venkateswara for giving me the strength and patience to work through all these years.

As much as my doctoral research work has been a personal pursuit, the story would not have been completed without the efforts and help from my co-workers, friends and well-wishers who have been an integral part of this saga for the last seven years. My heartfelt thanks and deep sense of appreciation to all the people mentioned here and others whose names I might have omitted unwittingly.

Date

Nalluri Srinivasa Rao

Table of contents

Contents	Page No.
Certificate	ii
Acknowledgements	iii
Abstract	v
Table of contents	ix
List of tables	xiv
List of figures	xiv
List of schemes	xvii
Abbreviations /Symbols	xviii
Chapter 1: Introduction	1 – 17
1.1 Nanocrystalline materials ²	
1.2 Gold nanoparticles	3
1.3 Core-shell nanostructures	6
1.4 Catalysis: H ₂ generation and 4-nitrophenol reduction	10
1.5 Scope of the present study	11
1.6 References	13
CHAPTER 2 Materials and Methods	18-22
2.1 Instrumental methods ¹⁹	
2.1.1 X-ray diffraction	19
2.1.2 Thermal analysis	19
2.1.3 Surface area measurements	20
2.1.4 X-ray photoelectron spectroscopy	20
2.1.5 Energy-dispersive X-ray fluorescence	20
2.1.6 Electron Microscopy	21
2.1.7 Scanning transmission electron microscopy	21
2.1.8 Small-angle X-ray scattering	21

2.1.9	Magnetic measurements	22
2.2	Catalysis	22

CHAPTER 3 Synthesis of Aunanoparticles by hydrocarbon based reducing agents

		23-31
3.1	Introduction	24
3.2	Experimental details	25
3.3	Results and discussion	25
3.4	Conclusion	29
3.5	References	30

CHAPTER 4 Solid-state synthetic approach for the fabrication of Fe₃O₄@Au core-shell

nanostructures		32-46
4.1	Introduction	33
4.2	Experimental details	35
	4.2.1 Materials	35
	4.2.2 Synthesis procedure	35
4.3	Results and discussion	35
	4.3.1 TGA-DTA results	35
	4.3.2 XRF studies	38
	4.3.3 XRD studies	39
	4.3.4 XPS studies	39
	4.3.5 FE-SEM studies	40
	4.3.6 HR-TEM studies	42
	4.3.7 STEM studies	43
	4.3.8 BET studies	43
	4.3.9 SAXS studies	44
4.4	Conclusion	45
4.5	References	45

CHAPTER 5 Solid state synthetic approach for the fabrication of Fe₃O₄@Ag core-shell

nanostructures	47-58
5.1 Introduction	48
5.2 Experimental details	48
5.2.1 Materials	48
5.2.2 Synthesis procedure	49
5.3 Results and discussion	49
5.3.1 TGA-DTA results	49
5.3.2 XRF studies	50
5.3.3 XRD studies	51
5.3.4 XPS studies	51
5.3.5 FE-SEM studies	52
5.3.6 HR-TEM studies	54
5.3.7 STEM studies	55
5.3.8 BET studies	55
5.3.9 SAXS studies	56
5.4 Conclusion	57
5.5 References	57

CHAPTER 6 Solid state synthetic approach for the fabrication of Fe₃O₄@AuAg alloy core-

shell nanostructures	59-68
6.1 Introduction	60
6.2 Experimental details	60
6.2.1 Materials	60
6.2.2 Synthesis procedure	60
6.3 Results and discussion	61
6.3.1 XRF studies	61
6.3.2 XRD studies	62
6.3.3 FE-SEM studies	63
6.3.4 HR-TEM studies	65

6.3.5	STEM studies	66
6.3.6	SAXS studies	66
6.4	Conclusion	67
6.5	References	68

CHAPTER 7 Catalytic applicability of the core-shell nanostructures Fe₃O₄@M (where M = Au, Ag and AuAg alloy) 69-78

7.1	Results and Discussion	70
7.1.1	Catalytic studies	70
7.1.2	Magnetic studies	75
7.2	Conclusions	76
7.3	References	77

CHAPTER 8 Solid-state synthesis, characterization and catalytic applicability of Fe₃O₄@Pd core-shell nanostructures 79-93

8.1	Introduction	80
8.2	Experimental details	81
8.2.1	Materials	81
8.2.2	Synthesis procedure	81
8.2.3	Catalysis	81
8.3	Results and discussion	82
8.3.1	TGA-DTA studies	82
8.3.2	XRD studies	82
8.3.3	XPS studies	84
8.3.4	FE-SEM studies	85
8.3.5	HR-TEM studies	87
8.3.6	BET studies	88
8.3.7	Magnetic studies	88
8.3.8	Catalytic studies	89
8.4	Conclusions	91

8.5	References	91
Chapter 9	Conclusions Future prospects	94-98
9.1	Conclusion	95
9.2	Future Prospects	97
	List of Publications and conference attended	99
	Biography of Candidate	101
	Biography of the Supervisor	101

List of tables

Table No.	Caption	Page No.
4.1	The calculated and experimentally obtained residual mass in different Fe ₃ O ₄ @Au-X samples	37
5.1	Calculated and experimental metal content (wt.%) in the Au and Ag precursors used in this study	50
8.1	Calculated and experimental metal content (wt.%) in the Pd precursor used in this study	82

List of figures

Figure No.	Caption	Page No.
1.1	Schematic representation of Au nanoparticle synthesis	4
1.2	Synthesis of Fe ₃ O ₄ @Au core-shell nanoparticles by iterative hydroxylamine seeding the direct deposition method	8
1.3	Synthesis of Fe ₃ O ₄ @Au core-shell NPs via Au-seeded growth methods using APTMS	9
1.4	A schematic representation of 4-nitrophenol reduction reaction in the presence of a catalyst surface	11
3.1	(a) UV-Vis spectra of reaction mixture (i) CHTE (ii) 1,3-CHDE and (iii) 1,4-CHDE and (b) powder x-ray pattern of solid obtained by centrifuging reaction mixture (CHTE) at 2000 rpm for 20 min	26
3.2	UV-spectra for (i) CHTE (ii) 1,3-CHDE and (iii) 1,4-CHDE	27
3.3	TEM images of Au nanoparticles obtained by (a) CHTE supernatant (b) CHTE solid (c) 1,3-CHDE and (d) 1,4 CHDE	27
3.4	¹ H NMR spectra of reaction mixture, the reaction being the reduction of Au ³⁺ by CHTE. The reaction was conducted in NMR tube with D ₂ O	28
3.5	¹ H NMR spectrum of CHTE in CDCl ₃	28
4.1	Thermogravimetric and differential thermal analyses of the Au-TOAB used in this study. Black, red and blue lines represent thermogravimetry, differential thermogravimetry, and differential thermal analysis curves, respectively	36
4.2	Thermogravimetric analyses of the physically grounded samples of Fe ₃ O ₄ core with Au-TOAB precursor before calcination	36
4.3	Morphology and structural characteristics of commercial Fe ₃ O ₄ . Top row is FESEM images at different magnification and bottom row is the XRD and XRF data	37
4.4	ED-XRF spectra of Fe ₃ O ₄ @Au-X. The respective dges are marked for Fe and Au. The y-axis on the left is for Fe and the one on the right is for Au	38
4.5	XRD patterns of Fe ₃ O ₄ @Au-X after calcination at 250 °C for 2 h	39
4.6	(a) Survey scan and (b) Au narrow 4f scanXPS of Fe ₃ O ₄ @Au-10	39
4.7	FE-SEM images of Fe ₃ O ₄ @Au-10 under different magnification	40
4.8	Low magnification FE-SEM images of Fe ₃ O ₄ @Au-X, where X = (a, b) 20, (c, d) 30, (e, f) 40, and (g, h) 50. Scale bar = 500 nm	41
4.9	FE-SEM images of Fe ₃ O ₄ @Au-X, where X = (a, b) 20, (c, d) 30, (e, f) 40, and (g, h) 50. Scale bar = 500 nm	41
4.10	HR-TEM images of Fe ₃ O ₄ @Au-10 (a-c) and Fe ₃ O ₄ @Au-40 at different magnifications	42
4.11	STEM images of (a-c) pristine Fe ₃ O ₄ (d-f) SiO ₂ (g-i) Fe ₃ O ₄ @Au-20 (j-l) SiO ₂ @Au-40. The first column are bright field images. The second and third column are composite images obtained in different magnifications	43

4.12	SAXS data for Fe ₃ O ₄ , Fe ₃ O ₄ @Au-10, Fe ₃ O ₄ @Au-40 samples	44
5.1	Thermogravimetric and differential thermal analysis of the metal precursors used in this study. Black, red and blue lines represent thermogravimetry, differential thermogravimetry, and differential thermal analysis curves, respectively	49
5.2	ED-XRF spectra of Fe ₃ O ₄ @Ag-X. The respective edges are marked for Fe and Au. The y-axis on the left is for Fe and the one on the right is for Au	50
5.3	XRD patterns of Fe ₃ O ₄ @Ag-X obtained after calcination at 250 °C for 2 h	51
5.4	XPS survey (top panel) and narrow (bottom panel) scan of Fe ₃ O ₄ @Ag-10	52
5.5	Field emission scanning electron microscopy (FE-SEM) images of and Fe ₃ O ₄ @Ag-10	53
5.6	FE-SEM images of Fe ₃ O ₄ @Ag-20 Fe ₃ O ₄ @Ag-30, Fe ₃ O ₄ @Ag-40, and Fe ₃ O ₄ @Ag-50	53
5.7	Low magnification FE-SEM images of Fe ₃ O ₄ @Ag-X, where X = (a, b) 20, (c, d) 30, (e, f) 40, and (g, h) 50. Scale bar = 500 nm	54
5.8	HR-TEM images of Fe ₃ O ₄ @Ag-10 (a-c) and Fe ₃ O ₄ @Ag-10 (d-f) at different magnifications	54
5.9	STEM images of (a-c) Fe ₃ O ₄ @Ag-20 (j-l) SiO ₂ @Ag-40. The first column are bright field images. The second and third column are composite images obtained in different magnifications	55
5.10	SAXS data for Fe ₃ O ₄ , Fe ₃ O ₄ @Ag-10, Fe ₃ O ₄ @Ag-40 samples	56
6.1	ED-XRF spectra of the three different alloy-based core-shell nanostructures	61
6.2	The calculated theoretical and observed variation of intensity at respective Au and Ag edge as a function of corresponding composition in the core-shell nanostructures	62
6.3	XRD patterns of the three different alloy-based core-shell nanostructures	63
6.4	FE-SEM AuAg alloy as a shell layer on top of the Fe ₃ O ₄ core (a) Fe ₃ O ₄ @AuAg-15:5, (b) Fe ₃ O ₄ @AuAg-10:10 and (c) Fe ₃ O ₄ @AuAg-5:15 nanostructures.	63
6.5	(A) The XRD patterns of SiO ₂ @AgAu-10:10, SiO ₂ @Ag-40, SiO ₂ @Au-40 and pristine SiO ₂ . (B) The magnified plot of (111) XRD planes for each catalyst to compare the variation of peak position with composition. (C), (D) and (E) ED-XRF spectra of SiO ₂ @Ag-40, SiO ₂ @Au-40, and SiO ₂ @AgAu-10:10, respectively	64
6.6	Low magnification FE-SEM images of (a, b) Fe ₃ O ₄ @AuAg-15:5, (c, d) Fe ₃ O ₄ @AuAg-10:10 and (e, f) Fe ₃ O ₄ @AuAg-5:15 alloy core-shell nanostructures. Scale bar = 500 nm	65
6.7	HR-TEM images (d-f) with various magnifications of Fe ₃ O ₄ @AuAg-10:10 under various magnifications	65
6.8	Composite STEM images of (A-C) Fe ₃ O ₄ @AuAg-10:10 and (D-F) SiO ₂ @Ag-10:10 under different magnifications	66

6.9	Small angle X-ray scattering (SAXS) Fe ₃ O ₄ @X-10, Fe ₃ O ₄ @X-40, Fe ₃ O ₄ @AuAg-20 (for different composition)	67
7.1	Hydrogen generation studies with Fe ₃ O ₄ @Au-20 and Fe ₃ O ₄ @Ag-20 from a 20 mL of a solution containing (a) 50 mM of AB and (b) 25 mM of NaBH ₄ as the hydrogen sources	70
7.2	(a) Hydrogen generation studies for different catalysts using a mixture of AB and NaBH ₄ as the hydrogen sources: (i) Fe ₃ O ₄ @Au-20, (ii) Fe ₃ O ₄ @AuAg-15:5, (iii) Fe ₃ O ₄ @AuAg-10:10, (iv) Fe ₃ O ₄ @AuAg-5:15 and (v) Fe ₃ O ₄ @Ag-20. (b) Recyclability studies under same conditions using Fe ₃ O ₄ @AuAg-10:10. In all cases, [AB] = 50 mM; [NaBH ₄] = 25 mM; Total volume of the solution = 20 mL, Catalyst loading = 50 mg	71
7.3	Kinetic studies with respect to (a, b) catalyst loading and (c, d) AB + NaBH ₄ mixture	72
7.4	Kinetic studies with respect to (A) catalyst loading and (B) AB + NaBH ₄ mixture using Fe ₃ O ₄ @SiO ₂ @AgAu-10:10	73
7.5	Temperature-dependent hydrogen generation studies (a) to estimate the energy of activation from Arrhenius plot (b)	73
7.6	Control experiments for hydrogen generation from AB and SBH mixture using pristine Fe ₃ O ₄ , SiO ₂ , and no-catalyst conditions	74
7.7	FE-SEM (a, b), HR-TEM (c) and ED-XRF (d) analyses on recycled Fe ₃ O ₄ @AuAg-10:10 alloy catalyst. The arrows indicate the polyborazylene regions	75
7.8	Low magnification FE-SEM images of Fe ₃ O ₄ @AuAg-10:10 alloy catalyst after 5 cycles. Scale bar = 500 nm	75
7.9	Magnetization as a function of external applied magnetic field for three samples as indicated in the figure	76
8.1	Thermogravimetric and differential thermal analyses of the metal precursors used in this study. Black and red represent thermogravimetry and differential thermogravimetry, curves, respectively	82
8.2	XRD patterns of Fe ₃ O ₄ @Pd-X obtained after calcination at 250 °C for 2 h	83
8.3	(a) XPS profile of Fe ₃ O ₄ @Pd-X (X=10,20,30) and Pd 3d narrow scan spectra for 10, 20 and 30 respectively	84
8.4	(a) XPS profile of Fe ₃ O ₄ @Pd-10, Fe ₃ O ₄ @Pd-10 heat treated at 900 °C and the duplicate spectra of the heat treated sample	85
8.5	High magnification FE-SEM images of Fe ₃ O ₄ @Pd-X, where X = normally cooled (A) 20, (B) 30, (C) 50 (D) 60 (E) 70 (F) 80 (G) 10 – heat treated at 500 °C, and (H) 10 – heat treated at 900 °C	86
8.6	HR-TEM images with various magnifications Fe ₃ O ₄ @Pd-10: (A-C) – heat treated at 250 °C, and (D-F) – heat treated at 900 °C	87
8.7	Plot of saturation magnetization (emu/g) vs external applied field for Commercial Fe ₃ O ₄ , Fe ₃ O ₄ @Pd-10 – heat treated at 250 °C, Fe ₃ O ₄ @Pd-10 – heat treated at 500 °C, and Fe ₃ O ₄ @Pd-10 – heat	89

	treated at 900 °C	
8.8	Plot of absorbance versus time. The decrease in the absorbance of 400 nm indicate the consumption of 4-nitrophenolate species. The appearance of peak at 300 nm is due to formation of 4-aminophenol product	90
8.9	Plot of C/C_0 versus time for the five successive cycles	90

List of schemes

Scheme No.	Caption	Page No.
3.1	Schematic representation of reducing molecule attaining aromaticity and thereby leading to the formation of Au nanoparticles. The red square denotes H atoms that is donated for the Au^{3+} reduction	24
4.1	Schematic representation of the solid state synthesis methodology to obtain $Fe_3O_4@M$ (M=Au, Ag, AuAg, Pd) core-shell nanostructures. The right-hand side images are representative SEM images of the core-shell systems reported in this thesis. For Au, Ag and AuAg surfactant based precursor was used and for Pd a non-surfactant based precursor was used. The applicability of the scheme was also demonstrated for spherical SiO_2 particles	34

Abbreviations

eV	Electron volt
keV	Kilo electron volts
V	Volts
nm	Nanometre
μm	Micrometre
cm	Centimetre
m	Metre
μL	Microliter
mL	Millimetre
L	Litre
mg	Milligram
g	Gram
mmol	Millimole
mol	Mole
sec	seconds
min	Minutes
hr	Hours
\AA	Angstroms
M	Molar
mM	Millimolar
W	Watt
%	Percentage
ppm	Parts per million
ppb	Parts per billion
R	Reflectance

Chapter 1

Introduction

The objective behind the search for new materials or improving the properties of existing materials is to find a suitable applications for practical purposes. In order to achieve the objective, it is necessary to tailor or manipulate the composition, alter the electronic, atomic and micro- structures. The manipulation becomes interesting and intriguing if the properties depends on the other finer details such as particle size and shape. In this regard, study and research on nanomaterials has become imminent as the properties depends on physical attributes such as particle size and shape. The properties of nanomaterials combined with their preparation methods play a critical role in contributing to the objective mentioned above. Besides the synthetic methods, the functionalization of nanomaterials have also become important due to the enhanced suitability of materials for a particular study or application. This thesis report novel synthetic approach for the synthesis of gold (Au) nanoparticles and core-shell nanostructures. Core-shell nanostructures are a class of materials denoted by core@shell, indicating the encapsulation of core by shell materials. A brief introduction to the concept of “nano” is given which is followed by a brief review various synthetic techniques that have been applied for the synthesis of Au nanoparticles and core-shell nanostructures. Along with the review of synthesis, the applications of these materials is also mentioned.

1.1 Nanocrystalline materials

Nanocrystalline materials are single crystalline or multiphase polycrystalline materials with crystallite size in the range of few nm, 1-100 nm.¹ The structures of these materials deviate from the structures of corresponding ideal crystals. These materials consist of high fraction of defects of about 50% with crystallites whereas the conventional materials have fraction of defects in the order of $10^{-4}\%$.² The large fraction of defects results in reduced atomic density, different local atomic arrangement and a broad distribution of interatomic spacings.³ At the surface of nanocrystalline materials, the atoms experience forces or potential that is altogether different from the atoms present in the crystallites. Thus, the arrangement of atoms at the surface happens in such a way that it leads to minimum energy configuration. As the particle size is decreased, the ratio of surface area/volume increases and this results in the change in the fraction of atoms present at the surface. This ultimately leads to a different configuration progressively on decreasing particle size. Hence, the properties of nanocrystalline materials are also governed

by the size of the particles. Both the defect concentration and the particle size have to be tuned to get interesting desirable host properties.

- 1) Cluster – A collection of units (atoms or reactive molecules) of up to about 50 units. Cluster compounds are such moieties surrounded by a ligand shell that allows isolation of molecular species (stable / isolable / soluble).
- 2) Colloid – A stable liquid phase containing particles in the particle size range of 1-1000 nm range. A colloidal particle is one such 1-1000 nm sized particle.
- 3) Nanoparticle – A solid particle in the 1-1000 nm range that could be noncrystalline, an aggregate of crystallites, or a single crystallite.
- 4) Nanocrystal – A solid particle that is a single crystal in the nanometer size range (1-to 10 nm).
- 5) Nanostructured or nanoscale material – Any solid material that has a nanometer dimension; three dimensions→particles; two dimensions→thin films; one dimension→thin wire
- 6) Nanophase material – The same as nanostructured material.
- 7) Quantum dot – A particle that exhibits a size quantization effect in at least one dimension.

It is important to know that quantum chemistry works in individual atoms and molecules whereas condensed matter theory works in conventional materials. Since, the microstructure is different in nanocrystalline systems, it can be expected to show unusual properties when compared to amorphous or conventional materials having same composition. Hence, the nanocrystalline solids can be represented as a class of compounds with a unique solid-state structure and their properties are always intriguing.

1.2 Gold Nanoparticles

The use of noble metal particles dates back to ancient times. Not much thought was given until late 1800s when Michael Faraday chemically synthesized colored Au nanoparticles. Although, the properties of Au nanoparticles were fascinating, the interesting applications drove the field⁴⁻⁶ The state of the art of Au nanoparticle synthesis have been reported by Astruc et. al.⁷ Another excellent review on Au nanoparticle synthesis focusing on chemical reduction synthesis mechanisms⁸ It can be summarized that Au nanoparticle synthesis involve reduction of Au³⁺ or

Au^+ by suitable reducing agents. The typical reaction parameter variations are i) Temperature, ii) Concentration of ions, iii) Nature of reducing agents, and iv) Stabilizing ligands. As huge number of literature is available on the synthesis, it is not possible to quote all the reports. We present the general synthetic methodology based on bottom-up approach for synthesis of Au nanoparticles which also present the subject from hierarchical evolution in the field of Au nanoparticle synthesis. The following are the important bottom-up methods that were reported at various stages of development of synthetic strategies: 1) Turkevich method; synthesis with sodium borohydride with/without citrate; 2) Seeding- growth; 3) synthesis by ascorbic acid; 4) green synthesis; 5) Brust-Schiffrin; and 6) synthesis using other reducing agents. A schematic representation of Au nanoparticle synthesis is given in Fig. 1.1.

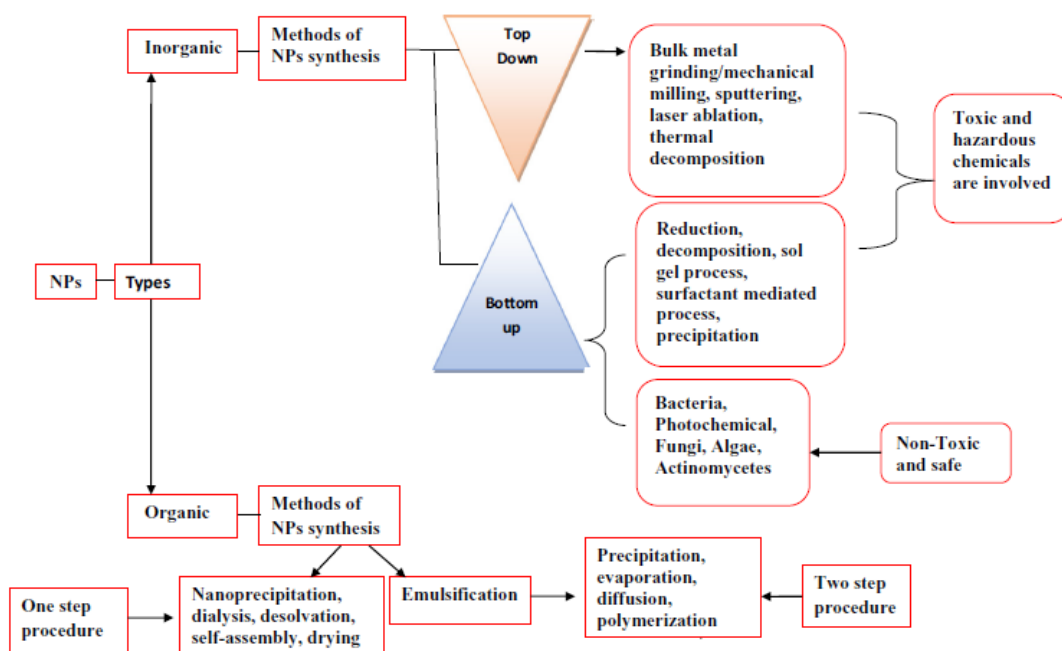


Figure 1.1: Schematic representation of Au nanoparticle synthesis adapted from⁹.

In a typical Turkevich based procedure¹⁰ for Au nanoparticle synthesis, a known volume of 34.0 mM (1.0 wt.%) trisodium citrate solution was rapidly injected to a known volume of 0.25 mM aqueous HAuCl_4 solution which is already kept at its boiling point.

Frens¹¹ reported that when a boiling solution of H₂AuCl₄ (0.2%) mixed with 0.5 mL of 1% sodium citrate for 5 min yielded nanoparticles with 16 nm. The colors varied from faintly blue to red.

Brust method involve a bi-phase reaction. An aqueous H₂AuCl₄ solution was mixed with tetraoctylammonium bromide (TOAB) (80 mL). During the vigorous stirring, the Au³⁺ species gets transferred into the organic layer and then dodecanethiol ligand (170 mg) was added. And a freshly prepared 0.4 M aqueous solution of sodium borohydride (25 mL) was slowly added with vigorous stirring. The reactant solution was stirred for 3 h, and the organic phase was separated and the solvent was evaporated. The resulting mixture was washed with 400 mL ethanol to remove excess thiol. This washing was carried out for another time. The particle size of 1.8 – 2.5 nm can be obtained by manipulating the ligand amount.¹²

In the seeded-growth method, a reducing agent was used to form in a first stage Au(0) nanoseeds from a Au precursor. These seeds were induced to grow into anisotropic Au in a second stage by using molecules (usually cationic surfactants) that adsorb preferentially on specific crystal facets showing high surface energies. A small concentrations of additional ions (such as or halides) are used as surface passivation components in a structure-directing role that enables control on the nanorod aspect ratio.¹³

In ascorbic acid method, a 4.0 mL of 0.01 M of aqueous solution of ascorbic acid was added to a series of solution containing 0.001 M H₂AuCl₄ (4.0 mL) and 0.01 M cetyltrimethyl ammonium bromide (CTAB) (1.0 to 8.0 mL). The reaction was performed at room temperature. The yellow colored reaction mixture became purple after the addition of ascorbic acid. The shape controlled anisotropic Au nanoparticles have been of great interest.^{14, 15} Novel reducing agents and stabilizing agents have been used. In the past four decades, there is a large volume of work exploring several synthetic strategies for the preparation of Au nanoparticles and solvents.¹⁶ Few strategic modifications that can be summarized into: 1) reducing agents 2) starting precursor 3) capping agent 4) dispersion in aqueous and organic phases. white phosphorus,¹⁷ cysteine.¹⁸ A green method was devised by Sadeghi et al.¹⁹ who used *Stevia rebaudiana* leaves extract to produce Au nanoparticles ranging from 5 to 20 nm. A 0.1 g of dried extract of stevia leaf to 50 mL deionized water and then stirred for 1 h in a magnetic stirrer. Clear stevia leaf extract was

mixed immediately into a 0.1 mM AuCl₄ solution of equal volume leading to the formation of Au nanoparticles with size ranging between 5 and 20 nm.

Dendrimers are three-dimensional, highly-branched and monodispersed polymeric nanostructures have been used in drug delivery systems.^{20, 21} They are synthesized via an iterative sequence of reactions such as Michael addition, alkylation and reduction.^{22, 23} Their shape and macromolecular characteristics allow ideal drug delivery by encapsulating drugs in their interior or covalently conjugating drugs on their surfaces. In particular, the application of dendrimers as versatile platforms for targeted cancer therapeutics.²¹ Another important modification is the solid state synthesis of Au nanosystems to control the size.²⁴⁻²⁶

To summarize, from the review of synthesis of Au nanoparticles, we note the following: 1) while it is desirable to have stabilizing to control size, the occupancy of ligands leads to the reduction in the catalytic active sites at the surface, 2) and similar detrimental effects observed for surface enhanced Raman scattering experiments, and 3) the presence of strong ligands such dodecanethiol ligands inhibits the formation of anisotropic structures. Recently, it was shown that a surfactant/polymer-free approach to achieving high-performance Au nanoparticles is reported.²⁷ With in a theoretical framework for the growth mechanism of nanoparticles without surfactant, strategies for shape-controlled synthesis based on a simple, green-chemistry synthesis of the four most commonly used morphologies: nanostars, nanospheres, nanorods, and nanoplates were applied. The nanoparticles obtained as result of implementing this strategy were showed superior performance than the particles coated with surfactants and polymers.

Using the above observations, our objective is to prepare Au nanoparticles by using reducing molecule for Au³⁺ ions which is a relatively a strong agent, and at the same time, the oxidized form of the reducing agent would acts as a weak stabilizer allowing the growth of Au nanoparticles, a strategy similar to that proposed in reference 27.

1.3 Core-shell nanostructures

Core-shell nanoparticles are of great interest to a various disciplines and applications. These core-shell nanoparticles find applications in a lot of areas including catalysis,²⁸⁻³¹ energy conversion, biological separation, medical imaging,³²⁻³⁴ and sensing. Therefore, important reviews have been reported. In 2012, a comprehensive review was performed by Paria et

al.,³⁵ covering all aspects of core-shell nanoparticles including synthesis, properties, characterization and applications. As mentioned earlier, the manipulating properties of materials is possible through composition, size, and shape. Thus, the synthetic aspects along with chemistry of functionalization play a critical role in the applications of core-shell nanoparticles.

The bottom-up approach can be classified into following concepts: wet-chemical synthesis, chemical-vapor deposition, laser-induced assembly (i.e., laser tapping), self-assembly, colloidal aggregation, film deposition and growth.³⁶⁻³⁸ These concepts give better control over particles attributes like size, shape and composition. Although various types of core-shell nanoparticles are present with chemical, and structural attributes with diversity, we concentrate on metal-oxide@metal nanostructures. And show that the synthetic scheme presented in this thesis can be extended to other types also. The synthesis of core-shell nanoparticles involve two steps: 1) the synthesis of core materials and 2) the formation of shell over the synthesized core. The synthesis of core oxide- nanoparticles itself is a subject which can be prepared by wet-chemical co-precipitation, precursor decomposition, hydrothermal reaction. The second step of metal deposition can be achieved by chemical reduction of salts or decomposition of shell salt precursor, both in the presence of core materials and suitable ligands.

In seed growth method, specific to Fe₃O₄@Au, the Au atoms are deposited onto Au-seeded Fe₃O₄ NPs in which Au seeds act as nucleation sites to facilitate the growth of Au shell. While the Au-seeded growth method requires an extra step than the direct-deposition method, but it also provides a possibility to tune the morphology of Au shell. Here, we list out details about the procedures that can be adopted for the synthesis of Fe₃O₄@Au nanoparticles.

Au shell were formed onto magnetic iron oxide nanoparticles in an aqueous solution via hydroxylamine seeding.³⁹ The hydroxylamine shells reduce Au³⁺ using a modification of Brown and Natan's iterative method and subsequently Au deposit onto the iron oxide surfaces yielding ~ 60 nm particles. A dilute iron oxide aqueous solutions of concentration 1.1 mM and stirred with an equal volume of 0.1 M sodium citrate for 10 min. In this way, the exchange of the adsorbed OH⁻ with citrate anions was achieved. This solution was further diluted and small volume of 1% HAuCl₄ were incrementally added along with an excess of 0.2 M NH₂OH·HCl. A total of five additions were performed; the clear solution became purple upon addition of Au³⁺ and gradually changed to deep pink during the successive iterations.

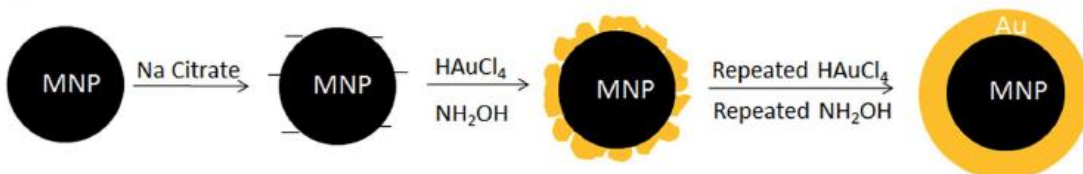


Figure 1.2: Synthesis of $\text{Fe}_3\text{O}_4@Au$ core-shell nanoparticles by iterative hydroxylamine seeding the direct deposition method.³⁹

Using micelle capped pre-prepared Fe_3O_4 and 1.0 M NaBH_4 , followed by an addition of aqueous 0.1 M HAuCl_4 solution core-shell nanoparticles can be prepared. The coating thickness can be varied by addition of different amount of Au ⁴⁰ and in this way, gold (silver)-coated magnetite⁴¹ nanoparticles have also been synthesized.

A microemulsion that was prepared from octane, cyclohexane, CTAB, and an aqueous mixture of ferric chloride, ferrous chloride, and HAuCl_4 solutions. The concentration of the stock solutions was maintained for instance, 1×10^{-1} M for FeCl_3 , 5×10^{-2} M for FeCl_2 , 0.8 M for NaBH_4 , and 1×10^{-1} M for HAuCl_4 aqueous solution. The assembly of Au nanoparticles on SiO_2 cores has been shown to be an approach to the formation of core-shell $\text{SiO}_2@Au$ nanoparticles.⁴²

A diluted Au nanoparticle solution was mixed with a known volume of pre-prepared SiO_2 nanoparticle solution that required to provide a surface area of silica equal to the total cross-sectional area of the Au nanoparticles. The solutions were stirred for 30–90 min. A similar approach has been demonstrated for the formation of Au-coated Fe_3O_4 nanoparticles, which involved the attachment of 2-3-nm-sized Au nanoparticles via 3-aminopropyltrimethoxysilane (APTMS) onto 10-nm-sized SiO_2 coated Fe_3O_4 nanoparticles.⁴³ The second step involved the attachment of 2–3 nm size Au nanoparticles onto APTMS-coated Fe_3O_4 nanoparticles. For this purpose, negatively charged Au are required which was then prepared by a modification of the method of Duff et al.⁴⁴

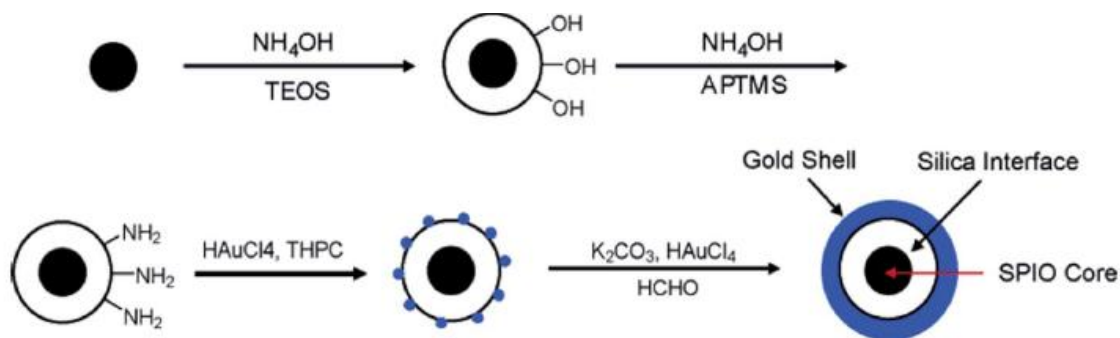


Figure 1.3: Synthesis of $\text{Fe}_3\text{O}_4@Au$ core-shell NPs via Au-seeded growth methods using APTMS.⁴⁵ In the figure, TEOS refers to tetraethyl orthosilicate.

Wang et al. reported Au shell formation in organic molecule (oleic acid/oleyl amine) encapsulated Fe_3O_4 nanoparticles.⁴⁶ The second step is described here. A phenyl ether pre-prepared Fe_3O_4 nanoparticle solution was mixed with gold acetate ($\text{Au}(\text{OOCCH}_3)_3$), 1,2-hexadecanediol. A 1:1 molar ratio of oleic acid and oleylamine was added to the reaction mixture. In this case, the mole ratio of the Au precursor to the iron oxide nanoparticles was approximately 7:1. The reaction solution was heated to 180–190 °C under argon atmosphere and vigorous stirring for 1.5 h. This synthesis procedure for $\text{Fe}_3\text{O}_4@Au$ nanoparticles leads to very high monodispersity and controllable surface capping properties.

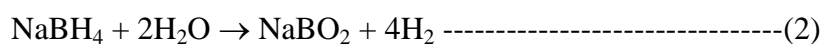
To summarize, from the introduction for core-shell nanoparticles we note the following: 1) while it is desirable to have stabilizing to control aggregation and deposit shell material, the diversity of shell materials is limited by the shell material precursor, and 2) such chemical methods use extensive solvent, the products need purification, and control of feed ratio are difficult. It can be seen from the above scheme that if the nucleation and seed growth of Au do not happen on the surface then it leads to separated Au nanoparticles thereby control of the composition of the product and thereby control of thickness is also difficult. Also, from the above scheme, it is clear the presented scheme offers a limitation in the choice of shell materials. The metal ions which can be reduced easily like Au and Ag can be used as shell material thereby limiting the choice of shell. Besides, the presence of ligands affects the applicability especially the bio-compatibility, the sensing and catalytic properties.

In order to address the above research gaps, we propose a solvent-less solid-state method. By applying a solid-state strategy during the shell formation step, the applicability of the

synthetic strategy to diverse shell materials will be enhanced. A solid-state chloride free method was used⁴⁷ prepare supported nanoparticles, however, the synthetic work did not represent core-shell nanoparticles.

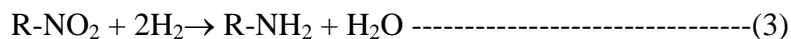
1.4 Catalysis: H₂ generation and 4-nitrophenol reduction

H₂ is a green and sustainable fuel. Therefore, the studies on storing and generating H₂ has been an intense topic of research. The potential candidates for hydrogen storage have been identified and they are sodium borohydride⁴⁸ and ammonia borane.⁴⁹ An excellent review on the potential of these molecules was given by Balaji Jagirdar.⁵⁰ The hydrolysis of ammonia borane gives H₂ as a product based on the equation below:



The core-shell nanoparticles prepared by solid-state approach were tested for their catalytic activity towards H₂ generation and 4-nitrophenol reduction. The volume of H₂ generated was followed by burette reading connected to the reaction vessel. There are other H₂ sources which are being studied but not discussed as it is beyond the scope of this introduction.

4-nitrophenol reduction reaction is considered as a benchmark reaction.⁵¹ A comprehensive kinetic analysis of this reaction is given by Ballauf et al.⁵² The reaction was shown to follow Langmuir-Hinshelwood mechanism.



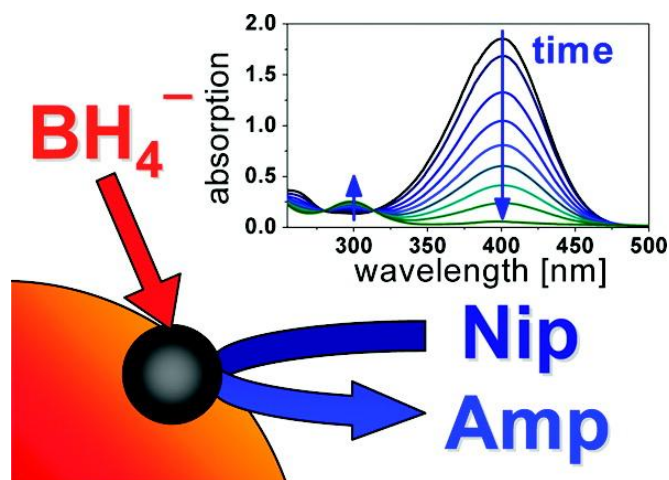


Figure 1.4: The schematic representation of 4-nitrophenol reduction reaction in the presence of a catalyst surface.⁵² In the figure, Nip and Amp refers to 4-nitrophenol and 4-aminophenol respectively.

The reaction is performed typically under excess borohydride conditions, say concentration of borohydride is 100 times more than the concentration of 4-nitrophenol which would enable the researchers to study the reaction kinetics using pseudo-first order model with respect to 4-nitrophenol. The reaction do not proceed in the absence of the catalyst. In the presence of sodium borohydride the 4-nitrophenol (colorless) gets converted to 4-nitrophenolate (yellow) exhibiting a UV-visible spectral peak at 400 nm. The decrease in the absorbance value of 400 nm peak (due to 4-nitrophenolate species) in the UV-spectra was monitored and considered as the progress of the reaction.

In recent times, the magnetic recoverability concept has been shown as a green and sustainable option.⁵³ The core-shell nanostructures with magnetic core would give another advantage of catalyst retrieval using a magnet post the reaction completion.⁵⁴

1.5 Scope of the Present Study

In the present study, Au nanoparticles are prepared by using hydrocarbon based reducing agent. The driving force for such reduction reaction is the driving force for the reducing molecules to attain aromaticity by donating H/H species from it. The reaction products were analyzed using NMR, TEM, XRD and UV-visible spectroscopy. The Au nanoparticles were found to possess a diameter of approximately 15 nm with twinned structure. As the thesis reports

novel reducing agents for the synthesis of Au nanoparticles, the Au nanoparticle formation and particle growth studies are beyond the scope of this thesis. The application studies of Au nanoparticles thus synthesized, for instance, catalysis may be a part of future studies.

A strategy for solvent-less solid-state process have been developed for the synthesis of $\text{Fe}_3\text{O}_4@\text{M}$ (M=Au, Ag, Pd and AuAg) core-shell nanoparticles. To demonstrate the versatility of the solid-state strategy, synthesis of $\text{SiO}_2@\text{M}$ (M=Au, Ag, AuAg) have also been performed. This rationally designed strategy is scalable, eco-friendly, cost-effective, and the composition of products is as per the initial feed ratio. Both surfactant (only Au, Ag, AuAg) and non-surfactant (only for Pd shell system) based metal precursors were coated on the pre-formed core uniformly in solid-state. The dispersion of the precursor aided by its melting lead to a uniform coating and on precursor decomposition, the core-shell nanostructures are formed. The composition of the product was controlled by the initial metal precursor content. The synthesis process have been studied by using TGA/DTA and the structural features and size/shape attributes of the products have been characterized by XRD, FE-SEM, HR-TEM, SAXS, ED-XRF, STEM and XPS. A lot of parameters like temperature gradient, heating and cooling rate during the synthesis may a significant role in the formation of uniform shell layer thickness. This aspect may be considered in our future studies. The as-synthesized $\text{Fe}_3\text{O}_4@\text{M}$ (M=Au, Ag, and AuAg) core-shell nanostructures have been tested for their catalytic activity towards hydrogen generation reaction using ammonia borane and sodium borohydride as sources. A detailed kinetic analysis have been performed of H_2 generation reaction have been performed. $\text{Fe}_3\text{O}_4@\text{Pd}$ nanoparticles were tested for 4-nitrophenol reduction using sodium borohydride reaction. For $\text{Fe}_3\text{O}_4@\text{Pd}$ systems, the catalytic studies were performed to illustrate the effectiveness of the synthetic strategy, the comparison of catalytic activity with the reported materials and structure catalytic-activity correlation have not been conducted.

1.6 References

1. Gleiter, H., Nanocrystalline materials. In *Advanced Structural and Functional Materials*, Springer: 1991; pp 1-37.
2. Zhu, X.; Birringer, R.; Herr, U.; Gleiter, H., X-ray diffraction studies of the structure of nanometer-sized crystalline materials. *Physical Review B* **1987**,*35* (17), 9085.
3. Mørup, S., Magnetic Properties of Fine Particles ed JL Dormann and D Fiorani. Amsterdam: Elsevier: 1992.
4. Li, N.; Zhao, P.; Astruc, D., Anisotropic gold nanoparticles: synthesis, properties, applications, and toxicity. *Angewandte Chemie International Edition* **2014**,*53* (7), 1756-1789.
5. Yeh, Y.-C.; Czeran, B.; Rotello, V. M., Gold nanoparticles: preparation, properties, and applications in bionanotechnology. *Nanoscale* **2012**,*4* (6), 1871-1880.
6. Zhang, J.; Mou, L.; Jiang, X., Surface chemistry of gold nanoparticles for health-related applications. *Chemical Science* **2020**,*11* (4), 923-936.
7. Zhao, P.; Li, N.; Astruc, D., State of the art in gold nanoparticle synthesis. *Coordination Chemistry Reviews* **2013**,*257* (3-4), 638-665.
8. De Souza, C. D.; Nogueira, B. R.; Rostelato, M. E. C., Review of the methodologies used in the synthesis gold nanoparticles by chemical reduction. *Journal of Alloys and Compounds* **2019**,*798*, 714-740.
9. Kumari, Y.; Kaur, G.; Kumar, R.; Singh, S. K.; Gulati, M.; Khursheed, R.; Clarisse, A.; Gowthamarajan, K.; Karri, V. N. R.; Mahalingam, R., Gold nanoparticles: New routes across old boundaries. *Advances in Colloid and Interface Science* **2019**,*274*, 102037.
10. Turkevich, J.; Stevenson, P. C.; Hillier, J., A study of the nucleation and growth processes in the synthesis of colloidal gold. *Discussions of the Faraday Society* **1951**,*11*, 55-75.
11. Frens, G., Controlled nucleation for the regulation of the particle size in monodisperse gold suspensions. *Nature physical science* **1973**,*241* (105), 20-22.
12. Brust, M.; Walker, M.; Bethell, D.; Schiffrin, D. J.; Whyman, R., Synthesis of thiol-derivatised gold nanoparticles in a two-phase liquid-liquid system. *Journal of the Chemical Society, Chemical Communications* **1994**, (7), 801-802.
13. Uson, L.; Sebastian, V.; Arruebo, M.; Santamaria, J., Continuous microfluidic synthesis and functionalization of gold nanorods. *Chemical Engineering Journal* **2016**,*285*, 286-292.

14. Pérez-Juste, J.; Pastoriza-Santos, I.; Liz-Marzán, L. M.; Mulvaney, P., Gold nanorods: synthesis, characterization and applications. *Coordination chemistry reviews* **2005**,*249* (17-18), 1870-1901.
15. Grzelczak, M.; Pérez-Juste, J.; Mulvaney, P.; Liz-Marzán, L. M., Shape control in gold nanoparticle synthesis. *Chemical Society Reviews* **2008**,*37* (9), 1783-1791.
16. Hussain, M. H.; Bakar, N. F. A.; Mustapa, A. N.; Low, K.-F.; Othman, N. H.; Adam, F., Synthesis of Various Size Gold Nanoparticles by Chemical Reduction Method with Different Solvent Polarity. *Nanoscale research letters* **2020**,*15* (1), 1-10.
17. Horisberger, M.; Rosset, J., Colloidal gold, a useful marker for transmission and scanning electron microscopy. *Journal of Histochemistry & Cytochemistry* **1977**,*25* (4), 295-305.
18. Ma, Z.; Han, H., One-step synthesis of cystine-coated gold nanoparticles in aqueous solution. *Colloids and Surfaces A: Physicochemical and Engineering Aspects* **2008**,*317* (1-3), 229-233.
19. Sadeghi, B.; Mohammadzadeh, M.; Babakhani, B., Green synthesis of gold nanoparticles using *Stevia rebaudiana* leaf extracts: characterization and their stability. *Journal of Photochemistry and Photobiology B: Biology* **2015**,*148*, 101-106.
20. Kesharwani, P.; Jain, K.; Jain, N. K., Dendrimer as nanocarrier for drug delivery. *Progress in Polymer Science* **2014**,*39* (2), 268-307.
21. Zhu, J.; Shi, X., Dendrimer-based nanodevices for targeted drug delivery applications. *Journal of Materials Chemistry B* **2013**,*1* (34), 4199-4211.
22. Samadaei, F.; Salami-Kalajahi, M.; Roghani-Mamaqani, H., Grafting of poly (acrylic acid) onto poly (amidoamine)-functionalized graphene oxide via surface-mediated reversible addition-fragmentation chain transfer polymerization. *International Journal of Polymeric Materials and Polymeric Biomaterials* **2016**,*65* (6), 302-309.
23. Golshan, M.; Salami- Kalajahi, M.; Roghani- Mamaqani, H.; Mohammadi, M., Synthesis of poly (propylene imine) dendrimers via homogeneous reduction process using lithium aluminium hydride: Bioconjugation with folic acid and doxorubicin release kinetics. *Applied Organometallic Chemistry* **2017**,*31* (11), e3789.
24. Patra, D.; Nalluri, S. R.; Tan, H. R.; Saifullah, M. S.; Ganesan, R.; Gopalan, B., New gold standard: weakly capped infant Au nanoclusters with record high catalytic activity for 4-

nitrophenol reduction and hydrogen generation from an ammonia borane–sodium borohydride mixture. *Nanoscale Advances* **2020**.

25. Rao, T. U. B.; Nataraju, B.; Pradeep, T., Ag₉ quantum cluster through a solid-state route. *Journal of the American Chemical Society* **2010**,*132* (46), 16304-16307.

26. Bera, A.; Busupalli, B.; Prasad, B. L., Solvent-Less Solid State Synthesis of Dispersible Metal and Semiconducting Metal Sulfide Nanocrystals. *ACS Sustainable Chemistry & Engineering* **2018**,*6* (9), 12006-12016.

27. Wall, M. A.; Harmsen, S.; Pal, S.; Zhang, L.; Arianna, G.; Lombardi, J. R.; Drain, C. M.; Kircher, M. F., Surfactant- Free shape control of gold nanoparticles Enabled by Unified Theoretical Framework of Nanocrystal Synthesis. *Advanced Materials* **2017**,*29* (21), 1605622.

28. Zhang, Q.; Lee, I.; Joo, J. B.; Zaera, F.; Yin, Y., Core–shell nanostructured catalysts. *Accounts of Chemical Research* **2013**,*46* (8), 1816-1824.

29. Gawande, M. B.; Goswami, A.; Asefa, T.; Guo, H.; Biradar, A. V.; Peng, D.-L.; Zboril, R.; Varma, R. S., Core–shell nanoparticles: synthesis and applications in catalysis and electrocatalysis. *Chemical Society Reviews* **2015**,*44* (21), 7540-7590.

30. Neri, G.; Bonavita, A.; Milone, C.; Galvagno, S., Role of the Au oxidation state in the CO sensing mechanism of Au/iron oxide-based gas sensors. *Sensors and Actuators B: Chemical* **2003**,*93* (1-3), 402-408.

31. Andreeva, D., Low temperature water gas shift over gold catalysts. *Gold Bulletin* **2002**,*35* (3), 82-88.

32. Coelho, B.; Siqueira, E.; Ombredane, A.; Joanitti, G.; Chaves, S.; Da Silva, S. W.; Chaker, J.; Longo, J. P. F.; Azevedo, R.; Morais, P., Maghemite–gold core–shell nanostructures (γ -Fe₂O₃@ Au) surface-functionalized with aluminium phthalocyanine for multi-task imaging and therapy. *RSC advances* **2017**,*7* (19), 11223-11232.

33. O'Grady, K., Biomedical applications of magnetic nanoparticles. *Journal of Physics D: Applied Physics* **2002**,*36* (13), 701.

34. Cui, Y.; Wang, Y.; Hui, W.; Zhang, Z.; Xin, X.; Chen, C., The synthesis of GoldMag nano-particles and their application for antibody immobilization. *Biomedical microdevices* **2005**,*7* (2), 153-156.

35. Ghosh Chaudhuri, R.; Paria, S., Core/shell nanoparticles: classes, properties, synthesis mechanisms, characterization, and applications. *Chemical reviews* **2012**,*112* (4), 2373-2433.

36. Sneh, O.; Clark-Phelps, R. B.; Londergan, A. R.; Winkler, J.; Seidel, T. E., Thin film atomic layer deposition equipment for semiconductor processing. *Thin solid films* **2002**,402 (1-2), 248-261.
37. Wang, Y.; Cai, K.; Yao, X., Facile synthesis of PbTe nanoparticles and thin films in alkaline aqueous solution at room temperature. *Journal of Solid State Chemistry* **2009**,182 (12), 3383-3386.
38. Yoo, S.-H.; Liu, L.; Park, S., Nanoparticle films as a conducting layer for anodic aluminum oxide template-assisted nanorod synthesis. *Journal of Colloid and Interface Science* **2009**,339 (1), 183-186.
39. Lyon, J. L.; Fleming, D. A.; Stone, M. B.; Schiffer, P.; Williams, M. E., Synthesis of Fe oxide core/Au shell nanoparticles by iterative hydroxylamine seeding. *Nano Letters* **2004**,4 (4), 719-723.
40. Carpenter, E. E.; Sangregorio, C.; O'Connor, C. J., Effects of shell thickness on blocking temperature of nanocomposites of metal particles with gold shells. *IEEE transactions on magnetics* **1999**,35 (5), 3496-3498.
41. Mikhaylova, M.; Kim, D. K.; Bobrysheva, N.; Osmolowsky, M.; Semenov, V.; Tsakalakos, T.; Muhammed, M., Superparamagnetism of magnetite nanoparticles: dependence on surface modification. *Langmuir* **2004**,20 (6), 2472-2477.
42. Westcott, S. L.; Oldenburg, S. J.; Lee, T. R.; Halas, N. J., Formation and adsorption of clusters of gold nanoparticles onto functionalized silica nanoparticle surfaces. *Langmuir* **1998**,14 (19), 5396-5401.
43. Caruntu, D.; Cushing, B. L.; Caruntu, G.; O'Connor, C. J., Attachment of gold nanograins onto colloidal magnetite nanocrystals. *Chemistry of Materials* **2005**,17 (13), 3398-3402.
44. Duff, D. G.; Baiker, A.; Edwards, P. P., A new hydrosol of gold clusters. 1. Formation and particle size variation. *Langmuir* **1993**,9 (9), 2301-2309.
45. Kwizera, E. A.; Chaffin, E.; Wang, Y.; Huang, X., Synthesis and properties of magnetic-optical core-shell nanoparticles. *RSC advances* **2017**,7 (28), 17137-17153.
46. Wang, L.; Luo, J.; Fan, Q.; Suzuki, M.; Suzuki, I. S.; Engelhard, M. H.; Lin, Y.; Kim, N.; Wang, J. Q., Monodispersed core-shell Fe₃O₄@ Au nanoparticles. *The Journal of Physical Chemistry B* **2005**,109 (46), 21593-21601.

47. Kondrat, S. A.; Shaw, G.; Freakley, S. J.; He, Q.; Hampton, J.; Edwards, J. K.; Miedziak, P. J.; Davies, T. E.; Carley, A. F.; Taylor, S. H., Physical mixing of metal acetates: a simple, scalable method to produce active chloride free bimetallic catalysts. *Chemical Science* **2012**,*3* (10), 2965-2971.
48. Demirci, U. B.; Miele, P., Reaction mechanisms of the hydrolysis of sodium borohydride: a discussion focusing on cobalt-based catalysts. *Comptes Rendus Chimie* **2014**,*17* (7-8), 707-716.
49. Metin, O.; Ozkar, S., Hydrogen generation from the hydrolysis of ammonia-borane and sodium borohydride using water-soluble polymer-stabilized cobalt (0) nanoclusters catalyst. *Energy & Fuels* **2009**,*23* (7), 3517-3526.
50. Sanyal, U.; Demirci, U. B.; Jagirdar, B. R.; Miele, P., Hydrolysis of ammonia borane as a hydrogen source: fundamental issues and potential solutions towards implementation. *ChemSusChem* **2011**,*4* (12), 1731-1739.
51. Pradhan, N.; Pal, A.; Pal, T., Silver nanoparticle catalyzed reduction of aromatic nitro compounds. *Colloids and Surfaces A: Physicochemical and Engineering Aspects* **2002**,*196* (2-3), 247-257.
52. Wunder, S.; Polzer, F.; Lu, Y.; Mei, Y.; Ballauff, M., Kinetic analysis of catalytic reduction of 4-nitrophenol by metallic nanoparticles immobilized in spherical polyelectrolyte brushes. *The Journal of Physical Chemistry C* **2010**,*114* (19), 8814-8820.
53. Polshettiwar, V.; Luque, R.; Fihri, A.; Zhu, H.; Bouhrara, M.; Basset, J.-M., Magnetically recoverable nanocatalysts. *Chemical reviews* **2011**,*111* (5), 3036-3075.
54. Baig, R. N.; Nadagouda, M. N.; Varma, R. S., Magnetically retrievable catalysts for asymmetric synthesis. *Coordination Chemistry Reviews* **2015**,*287*, 137-156.

Chapter 2

Materials and methods

This chapter present details with various experimental techniques that were used for chemical analyses, characterization of the synthesized Au nanoparticle samples and Fe₃O₄@M (where M = Au, Ag, Pd and AuAg alloy) and SiO₂@M (where M = Au, Ag, AuAg alloy) core-shell nanostructures.

2.1 Instrumental methods

2.1.1 X-ray diffraction

X-ray diffraction (XRD) patterns have been recorded using Rigaku Ultima IV with Cu K α radiation ($\lambda = 1.5418 \text{ \AA}$) at a scan rate of 1°/min and Ni filter. This technique has been used to ascertain the amorphous and crystalline nature of Au nanoparticles, and Fe₃O₄@M (where M = Au, Ag and AuAg alloy) core-shell nanostructures. The XRD pattern of Fe₃O₄, Fe₂O₃, Au, Ag, AuAg and Pd were assigned using the reported literature values. In a similar way, SiO₂@M (where M = Au, Ag and AuAg alloy) nanostructures were also characterized.

The crystallite size of ferrite nanoparticles was estimated from the XRD line broadening. The extent of broadening is expressed as

$$\beta = k \lambda / D \cos\theta$$

where β = broadening of diffraction line measured at half of its maximum intensity (radians), $\beta^2 = \beta_M^2 - \beta_S^2$, D is the mean diameter of the particles, β_M is the measured breadth of the diffraction line of the sample, β_S is the measured breadth of the line of the standard, k = 0.9 constant referred as shape factor, and λ is the wavelength of the x-rays used and is 1.5418 \AA .

2.1.2 Thermal analysis

Thermal analysis has been used to study the thermal decomposition of surfactant based metal precursor by recording weight loss vs temperature, ΔT (difference in the temperature between the sample and reference) vs temperature at different heating rates. Thermogravimetric analysis (TGA) and differential thermal analysis (DTA) of the ferric citrate precursor was performed in Shimadzu DTG-60 instrument from 30 to 700 °C with a heating rate of 10 °C/min in a nitrogen atmosphere to understand the mass loss and decomposition temperature. The

samples were placed in a platinum crucible and ignited alumina was used as the reference material. Using TGA mass loss analysis, the sample synthesis temperature was fixed.

2.1.3 Surface area measurements

Surface area measurements of the samples reported in this study were carried out by using single point BET (Brunauer, Emmett, Teller) method. BET surface area measurements on the samples were measured using Micromeritics ASAP 2020 surface area analyzer. The effect of shell formation on the porosity of core-shell nanostructures can be inferred from the magnitude of surface area.

2.1.4 X-ray photoelectron spectroscopy

The chemical composition and oxidation states of component elements were determined by X-ray photoelectron spectroscopy (XPS) at the respective core level XPS using PHI 5000 Versa Prob II (FEI Inc.). Both survey and narrow scans have been performed. The narrow scans were performed at the respective element edges. XPS is used to find the binding energy of the atoms except hydrogen and helium in the periodic table. From the binding energy values obtained from the surface of the material, one would be able to identify the elemental composition and their oxidation states

2.1.5 Energy-Dispersive X-Ray Fluorescence measurements

Energy-Dispersive X-Ray Fluorescence measurements (ED-XRF) experiments on the core-shell nanostructures were conducted on Panalytical Epsilon-1 instrument. This technique was useful to check the chemical composition of products is whether as per the feed ratio. The leaching studies of catalytically active constituents from the catalyst surface were also performed by ED-XRF. X-ray fluorescence is an emission phenomenon of the secondary X-rays that come from the element when it is bombarded with high energy radiation. Sodium to uranium can be easily detected from sub-ppm level to percentage level with the help of XRF. Elements with higher atomic number are easier for the detection as compared to the elements with lower atomic number. Hence, the technique is highly useful for studying the composition of metal oxides, doped samples and composite materials. XRF compares the spectral intensity of unknown samples to the standard samples.

2.1.6 Electron microscopy

The finer details of nanocrystalline ferrite particles have been determined using electron microscopy. The particle size and the morphology of the samples were studied using Field-Emission Scanning Electron Microscope (FE SEM) fitted with energy dispersive spectroscopy [Carl-Zeiss ULTRA-55] and High Resolution Transmission Electron Microscope (HR-TEM) images were obtained using JEOL, JEM 2100 at an accelerating voltage of 100 kV.

The scanning electron microscopy is an important characterization technique that uses a focused electron beam. In FE-SEM secondary electrons are emitted from the solid sample, which are collected to create an area map of the secondary emission. The technique is used to determine the surface morphology (texture) and chemical composition (in energy dispersive spectroscopy mode) of the material samples. For the SEM measurements, the samples in powder form were mounted on carbon tape. The samples were not subjected to sputtering due to the presence of metal shell.

In HR-TEM, the contrast between transmitted and non-transmitted e- beams is used and the image is created. This technique provides very high resolution image to the extent of 0.2 Å. One would be able to measure the inter-planar distance for the crystalline materials using this technique. A tiny speck of sample was suspended in about 10 ml of spectroscopic grade acetone and ultrasonicated for 30 s. A drop of this solution was spread on a 3 mm carbon coated copper grid.

2.1.7 Scanning Transmission Electron Microscope

Bright and dark-field scanning transmission electron microscopy (STEM) images were taken by using the FE-SEM (Apreo S, FEI) instrument with retractable STEM 3+ detector.

2.1.8 Small angle X-ray Scattering:

Small Angle X-ray Scattering (SAXS) measurements have been performed using a Rigaku Ultima IV instrument. The measurements have been made from 2θ ($q=4\pi\sin\theta/\lambda$) value of 0.06° to 2° at a scanning speed of $0.03^\circ/\text{min}$. The sample was placed and spread over a scotch tape and data were recorded in transmission geometry. Only the intensity analysis were performed using the equation, $\mu = -\ln(I_s/I_0) \times t$, where μ is the linear absorption coefficient, I_s is

the maximum scattering intensity of the sample, I_0 is the maximum intensity without the sample and t is the thickness of the sample.

2.1.9Magnetic measurements

Room temperature magnetization curves were measured using vibrating sample magnetometer (VSM) (Lakeshore 665).

2.2 Catalysis

For the hydrogen generation reaction studies, a two necked round bottomed flask was used the reactor vessel. One neck of the flask was connected to the gas burette and the other one was sealed with a rubber septum. The pH of the reaction medium was observed to be in the range of 9.2-9.7. The generated hydrogen was collected in the gas burette and the volume of hydrogen was measured as a function of time. The control experiments were also performed in this identical way except the usage of the catalyst.

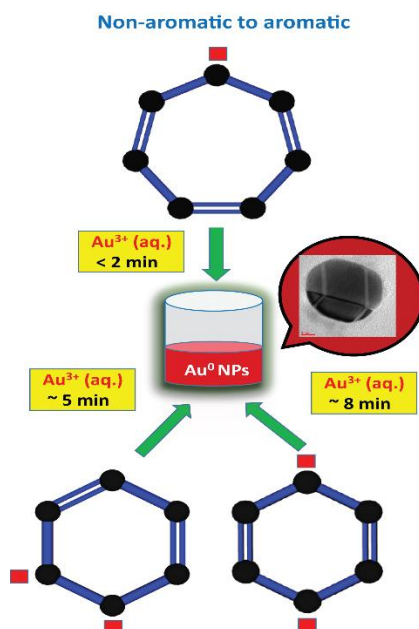
4-nitrophenol reduction reaction was monitored by using UV-visible spectrometer (JASCO-V650). The reaction was followed by monitoring the absorbance of 400 nm peak corresponding to 4-nitrophenolate peak as a function of time.

Chapter 3
**Synthesis of Au nanoparticles by hydrocarbon based
reducing agents**

3.1 Introduction

A rich chemistry, physics and application exhibited by Au nanoparticles have led to a plethora of studies.^{1,2} As a consequence, not only various synthetic strategies have been developed, which evolved through the years but functionalities were also attributed to suit the applications. Various organic molecules that were used in the synthesis of Au nanoparticles include citric acid,³⁻⁵ sodium borohydride,⁶ fungus *Verticillium* sp.,⁷ polyols,⁸ aldehydes⁹ and ketones.¹⁰ In the same way, citrates,⁴ thiols,⁶ and polymers^{11, 12} have been used as capping or encapsulating agents. Pure hydrocarbon based acetylide group has also been used to stabilize the Au nanoparticles by performing ligand exchange on the Au-PVP with phenyl acetylide.¹³

Conventionally, most of the synthetic methods reported involve the reduction of Au^{3+} salts using compounds or reducing agents that provide a course for hydride ion or organic compounds that can be easily oxidized.⁸⁻¹⁰ In this chapter, we reveal that Au nanoparticles in the size range of ~ 15 nm can be synthesized at room temperature using aromaticity as the driving force.



Scheme 3.1: Schematic representation of reducing molecule attaining aromaticity and thereby leading to the formation of Au nanoparticles. The red square denotes H atoms that is donated for the Au^{3+} reduction.

By this way, a stabilized and twinned nanoparticles can be obtained. The mechanism for the formation of nanoparticles has been discussed. A schematic diagram that explain the reaction between reducing agents used in this study is given below:

3.2 Experimental details

The hydrocarbon based molecules such as cycloheptatriene (CHTE), 1,3 cyclohexadiene (1,3-CHDE) and 1,4 cyclohexadiene (1,4-CHDE) have been used as the reducing agents. At room temperature, to a 70 mL of 8 mM HAuCl₄ aqueous solution, 5 μL of CHTE was added in one lot using a micropipette. The molar ratio of Au³⁺ to CHTE was 1:3. The pale yellow color solution turned into characteristic wine red within two minute indicating the formation of Au nanoparticles. The color change was instantaneous and there was no deepening of color later than this period. The synthetic protocol for Au nanoparticles remained same when diene systems was the same except the amount of reducing agent used was 10 μL. The time taken for the complete reaction with 1,3-CHDE and 1,4-CHDE was 6 and 8 minutes, respectively. A faint blue color appearance indicated the reaction completion.

3.3 Results and Discussion

Figure 3.1 (a) shows the UV-visible spectra of reaction mixtures at the end of the reaction, carried out using (i) CHTE (ii) 1,3-CHDE and (iii) 1,4-CHDE as reducing agents. A maximum in the absorbance (intensity) is observed in all the systems, indicating the presence of Au nanoparticles. While the λ_{max} for Au-CHTE system was 520 nm, the λ_{max} for 1,3-CHDE and 1,4-CHDE was red-shifted and was observed around 620 nm. Higher λ_{max} values can be attributed to the aggregated state of formed Au nanoparticles. The color intensity of the reaction solution was weak in diene systems than the CHTE system. The presence of a strong peak at 240 nm corresponding to the unreacted CHTE and the emergence of a new peak at 320 nm can be attributed to the presence of tropylium ion in solution (Figure 3.2). A black solid was obtained (Au-CHTE-precipitate) by centrifuging reaction mixture at 2000 rpm for 20 min.

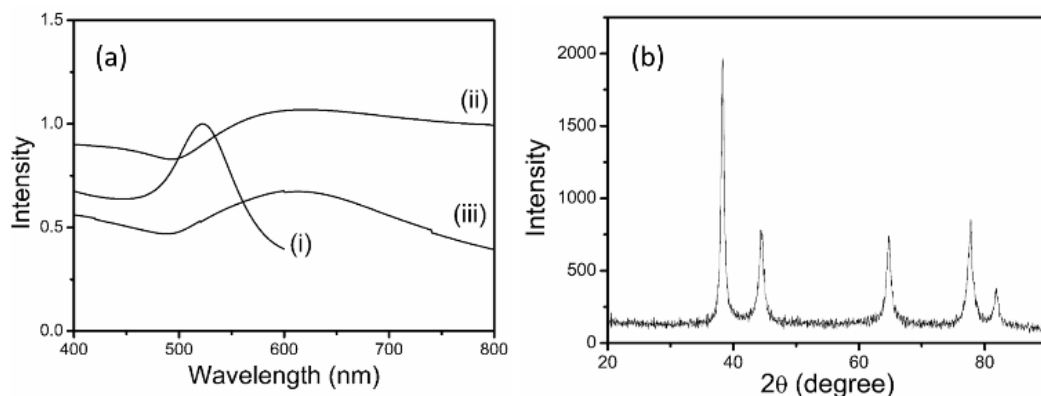


Figure.3.1: (a) UV-Vis spectra of reaction mixture (i) CHTE (ii) 1,3-CHDE and (iii) 1,4-CHDE and (b) powder x-ray pattern of solid obtained by centrifuging reaction mixture (CHTE) at 2000 rpm for 20 min.

After centrifugation, the color intensity of the supernatant solution was observed to be lesser than that of the original reaction mixture. This indicated that the reaction mixture consisted of stabilized and unstabilized Au nanoparticles. Fig. 1(b) shows the powder x-ray pattern of black solid obtained (Au-CHTE-ppte). The pattern clearly indicated the sample to be gold (JCPDS file: 04-0784) and the broadened peaks indicated that the sample was composed of nanocrystallites. Figure 3.3 displays the TEM of Au nanoparticles obtained from (a) Au-CHTE (supernatant) (b) Au-CHTE-(ppte) (c) Au-1,3-CHDE and (d) Au-1,4-CHDE. Fig. 3.3(a) showed that the Au nanoparticles that were formed have a size of ~15 nm. The inter-planar spacing determined from lattice fringes was 0.236 nm, which corresponds to the value for Au (111) plane. The Au-CHTE-(ppte) consists of agglomerates of 5 nm particles. In the case of dienes, (Fig. 3.3 (c) and (d)), the particle size was found to be around 15 nm and 5 nm, respectively. Also from images, the twinning in nanoparticles were observed in Au-CHTE (supernatant) and 1,3-CHDE but not in 1,4-CHDE system.

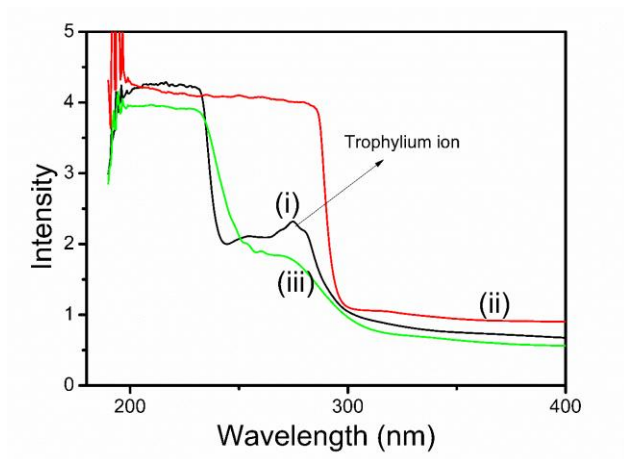


Figure 3.2: UV-spectra for (i) CHTE (ii) 1,3-CHDE and (iii) 1,4-CHDE

Figure 3.4 shows the ^1H NMR spectrum of reaction mixture measured in D_2O . The peaks at δ 1.2, 4.4 and 5.5 indicated the presence of unreacted CHTE left over in the reaction mixture (Figure 3.5). The appearance of peak at δ 9.5 confirmed the formation of trophylium ion in the reaction mixture. A spurious peak was also observed at around δ 7.3. As, at the end of the NMR measurement, the solid got settled at the bottom, this spurious peak may be due to any other organic side product or a complex between CHTE and Au^{3+} ions.

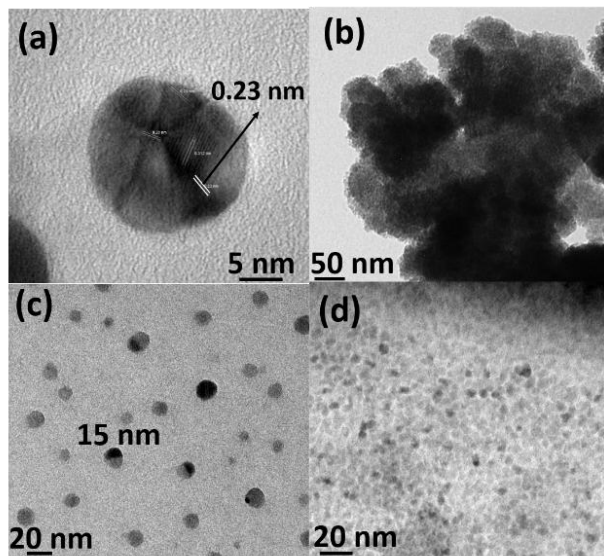


Figure 3.3: TEM images of Au nanoparticles obtained by (a) CHTE supernatant (b) CHTE solid (c) 1,3-CHDE and (d) 1,4-CHDE.

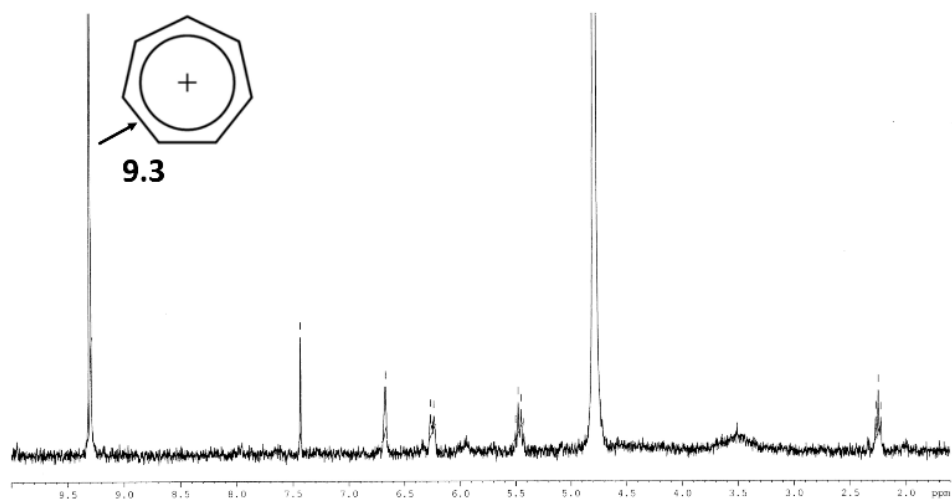


Figure 3.4: ¹H NMR spectra of reaction mixture, the reaction being the reduction of Au³⁺ by CHTE. The reaction was conducted in NMR tube with D₂O.

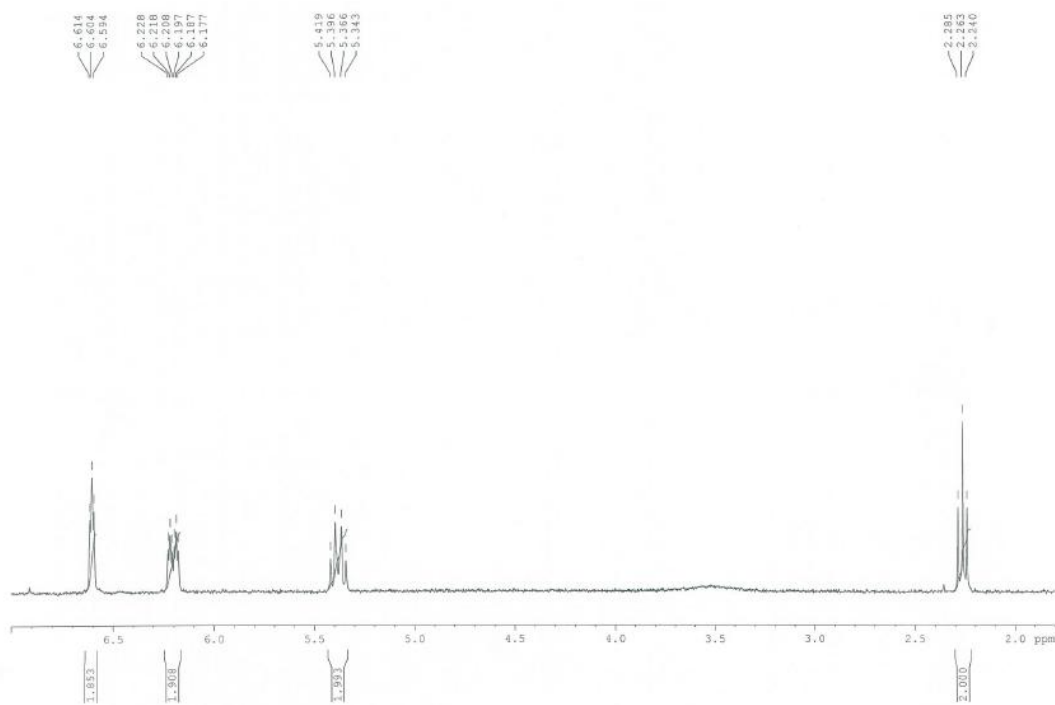


Figure 3.5: NMR spectrum of CHTE in CDCl₃.

From the UV-visible spectra, TEM, XRD the formation of Au nanoparticles can be ascertained. Despite the very less reaction time (below 1 min) for Au³⁺ reduction by CHTE, it is interesting to note the formation of twinned crystals. We propose that the first step is the

interaction of π electrons of CHTE and CHDE with metal ions which is followed by the second step of reduction of metal ions by the same molecules. Further, the formed nanoparticles nucleate and grow in this environment resulting in twinning to yield such nanoparticles. The reduction reaction is not complete as evident from the UV-spectra and NMR, which showed the presence of unreacted CHTE.

The reaction of CHTE is faster than dienes that are considered in this study. The pK_b of CHTE is 36, indicating that it can readily give out H^- species. In the process of giving H^- species, CHTE can attain aromaticity readily.¹⁴ The H^- species thus generated reduce the Au^{3+} ions to Au leading to the formation of nanoparticles. Although, the resonance energy for 1,3 and 1,4-CHDE is same which is about 10 kJ/mol, a difference in reactivity between two dienes was observed. 1,3-CHDE is higher in energy over 1,4-CHDE by 1.6 kJ/mol.¹⁵ Hence, 1,3-CHDE reacts slightly faster and lead to the formation of benzene. Typically, the λ_{max} for Au nanoparticles was reported to be around 520 nm and here in the case of dienes it is 620 nm. From the TEM images, the sizes were determined to be below 20 nm, thus higher λ_{max} may indicate that there is agglomeration or the formation of super lattice structures.

In conclusion, we have demonstrated that Au nanoparticles can be prepared by using non-aromatic compounds as reducing agents. Thereby, these non-aromatic molecules attain a stable aromatic state. The synthesis is rapid and occur at room temperature in water as the solvent. This opens up the avenue for design of synthetic methods for such Au nanoparticle synthesis with a variety of substituted systems and water soluble derivatives that still have the tendency to attain aromaticity.

3.4 Conclusions

We have demonstrated that driving force towards aromaticity can be exploited for the synthesis of Au nanoparticles. Cycloheptatriene readily loses H^- which can be used a reducing agent that the reaction is completed in 3 min yielding 15 nm twinned Au nanoparticles. The interesting point is that CHTE is not soluble in water giving a turbidity which was not observed when Au^{3+} was present. Thus, this reaction takes place at the interface and the reaction proceeds the CHTE goes into reaction solution as trophylum ion. The reaction and Au nanoparticles formation needs further detailed investigation.

3.5 References:

1. Daniel, M.-C.; Astruc, D., Gold nanoparticles: assembly, supramolecular chemistry, quantum-size-related properties, and applications toward biology, catalysis, and nanotechnology. *Chemical reviews* **2004**,*104* (1), 293-346.
2. Yeh, Y.-C.; Creran, B.; Rotello, V. M., Gold nanoparticles: preparation, properties, and applications in bionanotechnology. *Nanoscale* **2012**,*4* (6), 1871-1880.
3. Turkevich, J.; Stevenson, P. C.; Hillier, J., The formation of colloidal gold. *The Journal of Physical Chemistry* **1953**,*57* (7), 670-673.
4. Frens, G., Controlled nucleation for the regulation of the particle size in monodisperse gold suspensions. *Nature physical science* **1973**,*241* (105), 20-22.
5. Kimling, J.; Maier, M.; Okenve, B.; Kotaidis, V.; Ballot, H.; Plech, A., Turkevich method for gold nanoparticle synthesis revisited. *The Journal of Physical Chemistry B* **2006**,*110* (32), 15700-15707.
6. Brust, M.; Walker, M.; Bethell, D.; Schiffrin, D. J.; Whyman, R., Synthesis of thiol-derivatised gold nanoparticles in a two-phase liquid-liquid system. *Journal of the Chemical Society, Chemical Communications* **1994**, (7), 801-802.
7. Mukherjee, P.; Ahmad, A.; Mandal, D.; Senapati, S.; Sainkar, S. R.; Khan, M. I.; Ramani, R.; Parischa, R.; Ajayakumar, P.; Alam, M., Bioreduction of AuCl₄⁻ ions by the fungus, *Verticillium* sp. and surface trapping of the gold nanoparticles formed. *Angewandte Chemie International Edition* **2001**,*40* (19), 3585-3588.
8. Sun, Y.; Xia, Y., Shape-controlled synthesis of gold and silver nanoparticles. *science* **2002**,*298* (5601), 2176-2179.
9. Nath, S.; Ghosh, S. K.; Panigrahi, S.; Pal, T., Aldehyde assisted wet chemical route to synthesize gold nanoparticles. **2004**.
10. Peveler, W. J.; Parkin, I. P., Rapid synthesis of gold nanostructures with cyclic and linear ketones. *RSC advances* **2013**,*3* (44), 21919-21927.
11. Shan, J.; Tenhu, H., Recent advances in polymer protected gold nanoparticles: synthesis, properties and applications. *Chemical Communications* **2007**, (44), 4580-4598.
12. Ogoshi, T.; Umeda, K.; Yamagishi, T.-a.; Nakamoto, Y., Synthesis of phenolic polymer-coated gold nanoparticles. *Polymer journal* **2008**,*40* (10), 942-943.

13. Maity, P.; Tsunoyama, H.; Yamauchi, M.; Xie, S.; Tsukuda, T., Organogold clusters protected by phenylacetylene. *Journal of the American Chemical Society* **2011**, *133* (50), 20123-20125.
14. Graham Solomons, T.; Fryhle, C., Organic chemistry 8th edition. John Wiley & Sons, Inc: 2004.
15. NIST webbook: <http://webbook.nist.gov/cgi/cbook.cgi?ID=C628411&Mask=8> (April 2017).

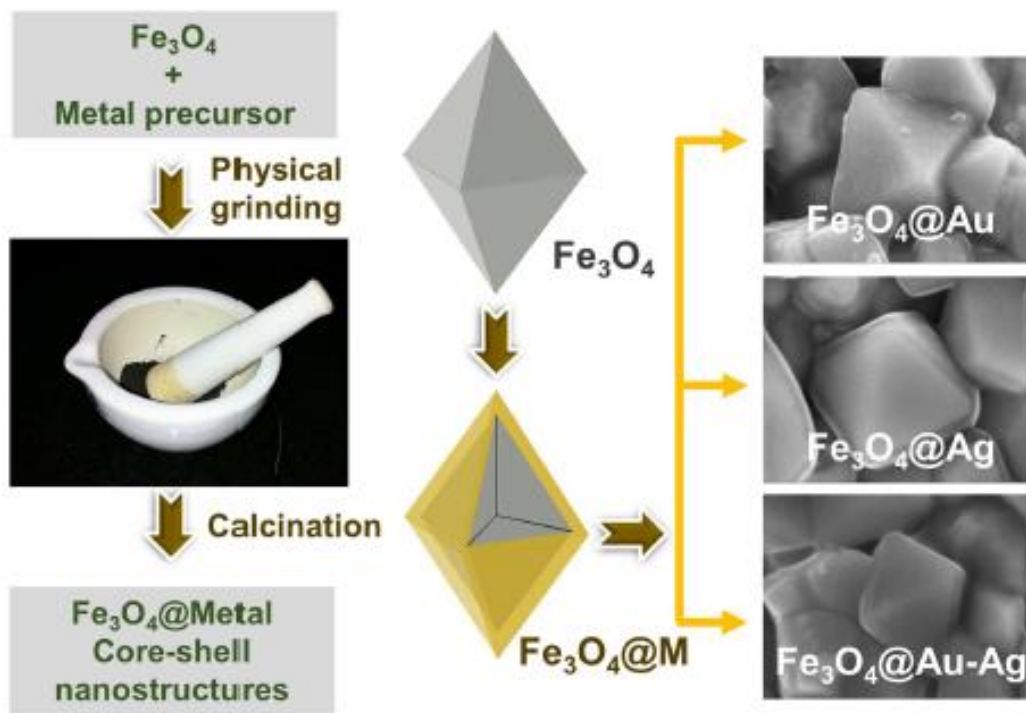
Chapter 4

Solid-state synthetic approach for the fabrication of $\text{Fe}_3\text{O}_4@Au$ core-shell nanostructures

4.1 Introduction

This chapter deals with the synthesis of $\text{Fe}_3\text{O}_4@Au$ nanostructures. The results obtained for structural, chemical, microstructural, magnetic characterization results by using TGA-DTA, XRD, XRF, XPS, FE-SEM, BET, HR-TEM, STEM, SAXS, VSM techniques are discussed. To demonstrate the versatility of the method, $\text{SiO}_2@Au$ nanostructures were prepared and the respective data are also presented.

In $\text{Fe}_3\text{O}_4@Au$ nanoparticles, researchers have utilized epitaxial growth approach, wherein Au^{3+} was reduced in the presence of Fe_3O_4 core using various reducing agents such as sodium citrate, sodium borohydride, glucose etc.¹ This method suffers a setback as individual self-nucleated Au nanoparticles may also be formed during the reaction and a separate purification step is needed. In another approach, a small amount of Au nanoparticles were adsorbed onto Fe_3O_4 nanoparticles that act as a seed layer for further growth of the metal shell. This approach requires the surface of the core to be chemically modified or pre-conditioned for favorable chemical or electrostatic interactions.¹ Despite the enormous potential offered by these type of core-shell nanostructures, their utility at the industrial level is limited by the solution-phase synthetic approaches that lack scalability, the requirement of further purification step, and the resulting high cost. Furthermore, some of the core-shell nanostructures e.g. metal sulfide@metal selenide, the syntheses are mainly carried out in harmful organic solvents like trioctylphosphine-trioctylphosphine oxide mixture.² Solid-state synthesis of metal nanoparticles (Pd and Au) anchored onto support (TiO_2 and carbon) has been reported by physically mixing the precursor with the support and subsequent calcination.³ Such systems studied in the literature do not represent core-shell nanostructures.⁴ On the other hand, the formation of a continuous metal film over oxide support from a molten metal at high temperatures is a long standing problem, wherein the uniform spreading of the metal film is inhibited by the formation of ridges on the oxide surface.^{5, 6} Therefore, any factor that decreases the formation of ridges or decreases the surface tension of the molten metal will lead to the formation of a continuous metal film. Here, we demonstrate the fabrication of $\text{Fe}_3\text{O}_4@Au$ nanostructures using solid state synthetic approach. This approach involves simple physical grinding of the metal precursor over commercial Fe_3O_4 core followed by calcination (Scheme 4.1).



Scheme 4.1: Figure 1. Schematic representation of the solid state synthesis methodology to obtain Fe_3O_4 @M (M=Au, Ag, AuAg, Pd) core-shell nanostructures. The right-hand side images are representative SEM images of the core-shell systems reported in this thesis. For Au, Ag and AuAg surfactant-based precursor was used. And for Pd a non-surfactant based precursor was used. The applicability of the scheme was also demonstrated for spherical SiO_2 particles.

The magnetite coated with Au nanosystems offers properties like magnetic recoverability in catalysis, magnetic hyperthermia, magnetoplasmonic etc.⁷⁻¹² In case of metal shells, Au has been chosen for its well-known plasmonic,¹³ catalytic and biological applications, We hypothesized that coating a noble metal-containing surfactant-based precursor over an oxide core as a thin film followed by metallization would result in a continuous metal shell formation. Therefore, keeping the coatability in mind, surfactant-based metal precursors such as gold-tetraoctylammonium bromide complex (Au-TOAB). The complex Au-TOAB is known for its film formability and therefore expected to yield a good coating over the magnetite core during the synthesis.¹⁴

4.2 Experimental details

4.2.1 Materials. Commercial Fe_3O_4 obtained from Aldrich was chosen to be the core particles. SiO_2 was prepared by adopting Stober's method. The commercial Fe_3O_4 had a regular octahedron and SiO_2 had a spherical morphology. The particle dimension was approximately around 250 nm in both core materials. The gold precursor, Au-TOAB was synthesized following the literature procedure.¹⁴

4.2.2 Synthesis procedure. In a typical core-shell synthesis using our solid-state approach, a calculated amount of the Au-TOAB was mixed with the magnetite core followed by thorough grinding for 10 min in order to achieve a uniform coating of the precursor over the Fe_3O_4 core. The obtained mixture was transferred to an autoclave and subjected to calcination 250 °C for 2 h. An autoclave was used in order to avoid any surface oxidation during metallization. Typically, the core-precursor assembly after the calcination step was allowed to cool naturally inside the furnace, thus ensuring a slow cooling, unless otherwise mentioned. The resultant products have been labelled as $\text{Fe}_3\text{O}_4\text{@M-X}$, where M and X represent the metal and the weight percent of its corresponding precursor with respect to the initial Fe_3O_4 content, respectively. The product obtained was $\text{Fe}_3\text{O}_4\text{@Au}$ and was used without any purification for characterization purposes.

4.3. Results and discussion

4.3.1 TGA-DTA results

The thermal stability of the precursors has been studied using thermogravimetric and differential thermal analyses. The differential thermal analyses revealed the low melting point of Au-TOAB to be 50 °C. The thermal decomposition and the corresponding derivative plot of the precursors are given in the Fig 4.1. The onset of the thermal decomposition in these precursors was found to be close to 200 °C and the major mass loss was found to occur between 230 and 270 °C. Based on the derivative plot, the lowest calcination temperature in this study had been fixed at 250 °C. The calculated and experimental residual mass of the metals in the corresponding precursors is given in the Table 4.1.

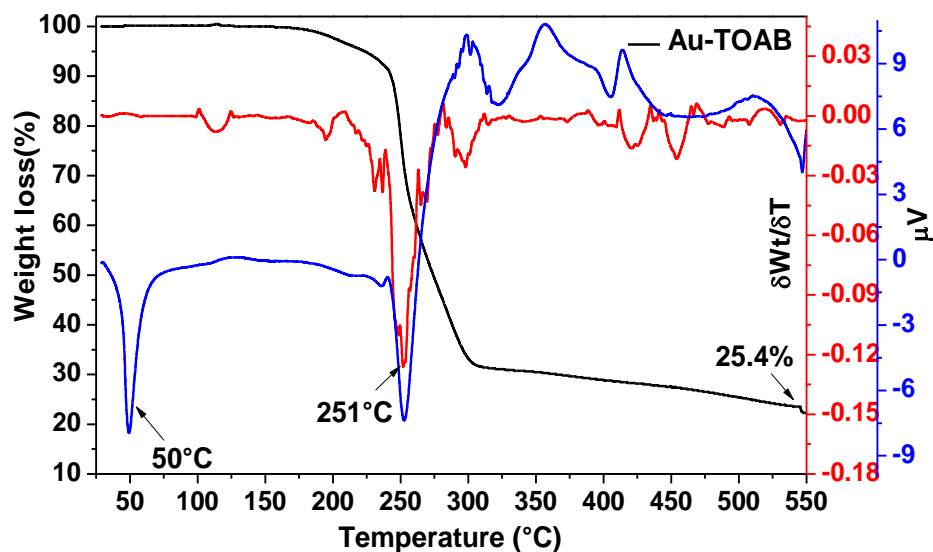


Figure 4.1. Thermogravimetric and differential thermal analyses of the Au-TOAB used in this study. Black, red and blue lines represent thermogravimetry, differential thermogravimetry, and differential thermal analysis curves, respectively.

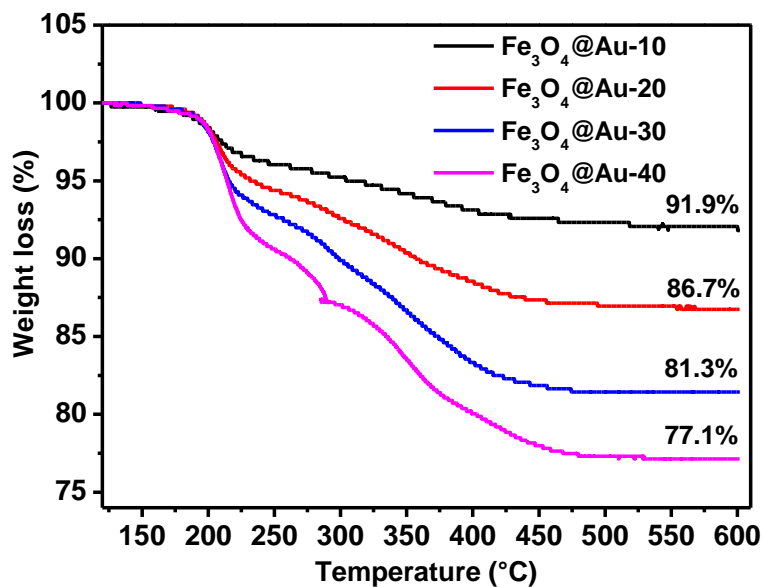


Figure 4.2 Thermogravimetric analyses of the physically grounded samples of Fe_3O_4 core with Au-TOAB precursor before calcination.

Table 4.1. The calculated and experimentally obtained residual mass in different Fe₃O₄@Au-X samples. The calculated values were obtained from TGA of pure Au-TOAB.

Sample	Calculated residual mass (wt.%)	Experimental residual mass (wt.%)
Fe ₃ O ₄ @Au-10	93.2	91.9
Fe ₃ O ₄ @Au-20	87.6	86.7
Fe ₃ O ₄ @Au-30	82.3	81.3
Fe ₃ O ₄ @Au-40	78.7	77.1

The structural and morphological characteristics of commercial Fe₃O₄ are given in Fig. 4.3. The powder X-ray diffraction (XRD) pattern clearly indicates the presence of cubic spinel phase of Fe₃O₄ core. The FE-SEM indicates the morphology of commercial samples is regular octahedron in nature.

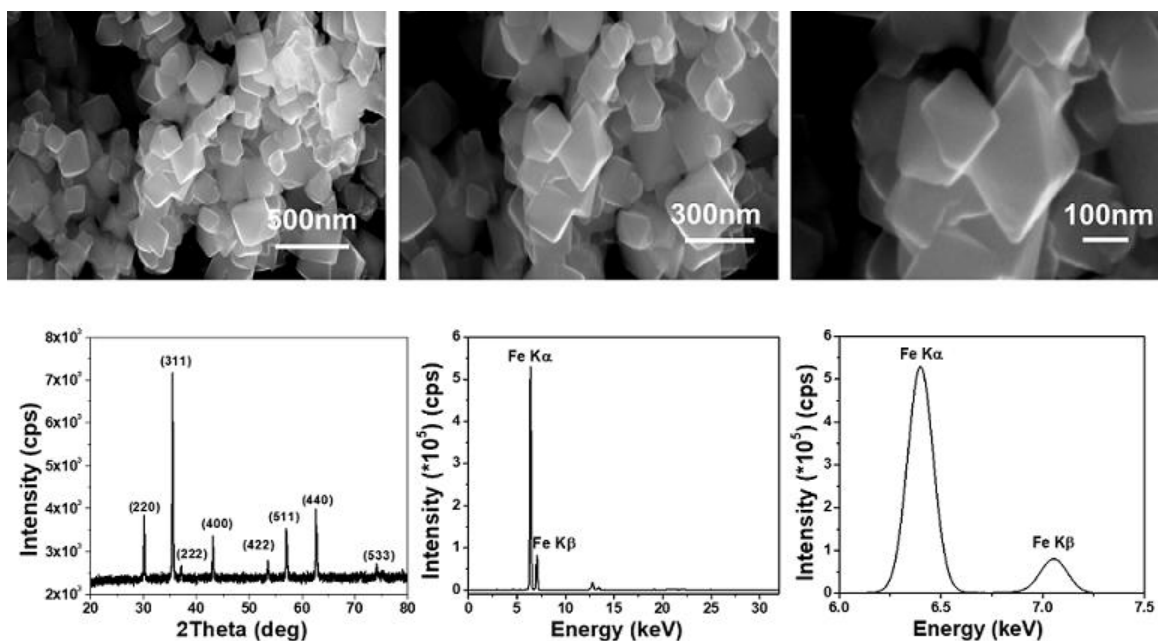


Figure 4.3 Morphology and structural characteristics of commercial Fe₃O₄. Top row is FESEM images at different magnification and bottom row is the XRD and XRF data.

4.3.2 XRF studies

To further validate and quantify the metal content against the precursor loading, the synthesized core-shell nanostructures were characterized using energy dispersive X-ray fluorescence (ED-XRF). ED-XRF was employed as X-rays in this technique have higher penetration depth (~1-2 μm) and therefore the elemental composition obtained using this technique would be close to the bulk composition. Figure 4.4 shows the ED-XRF spectra of $\text{Fe}_3\text{O}_4@Au-X$. As seen in figure, the intensity of Fe $K\alpha$ at 6.4 keV was decreasing with increasing Au content, while the intensity of Au $L\alpha$ at 9.7 keV was systematically increased. The peak intensities fit linearly with increasing the noble metal content, which confirms that the composition of the resultant core-shell nanostructures is as per the feed ratio.

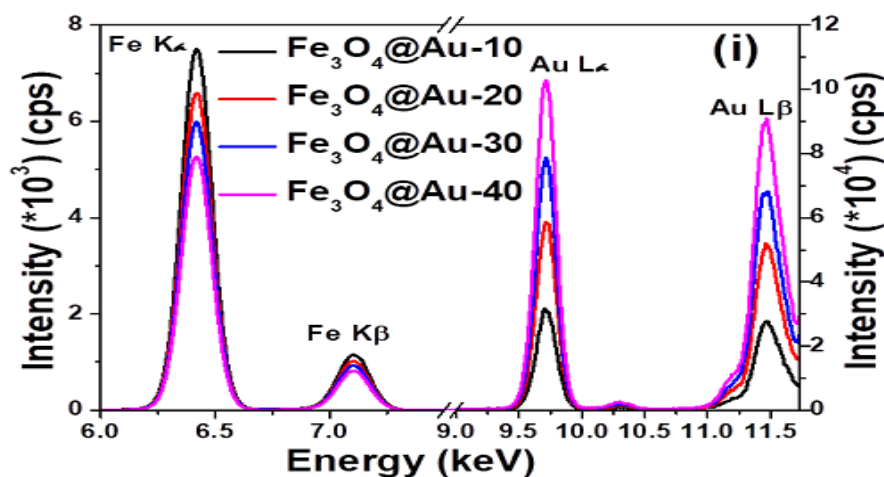


Figure 4.4 ED-XRF spectra of $\text{Fe}_3\text{O}_4@Au-X$. The respective edges are marked for Fe and Au. The y-axis on the left is for Fe and the one on the right is for Au.

4.3.3. XRD studies

The powder X-ray diffraction (XRD) patterns of the products obtained from the commercial Fe_3O_4 mixed with various loadings of Au-TOAB is shown in Fig. 4.5 (a-d). The products were obtained after calcination at 250 $^\circ\text{C}$ for 2 h. It can be observed from the figure that along with the inverse spinel magnetite phase, the characteristic peaks for (111) planes of Au were also observed. As expected, the relative intensity of (111) plane increased with increasing

metal precursor loading. This is indicative of the increase in Au content as per the increasing feed ratio.

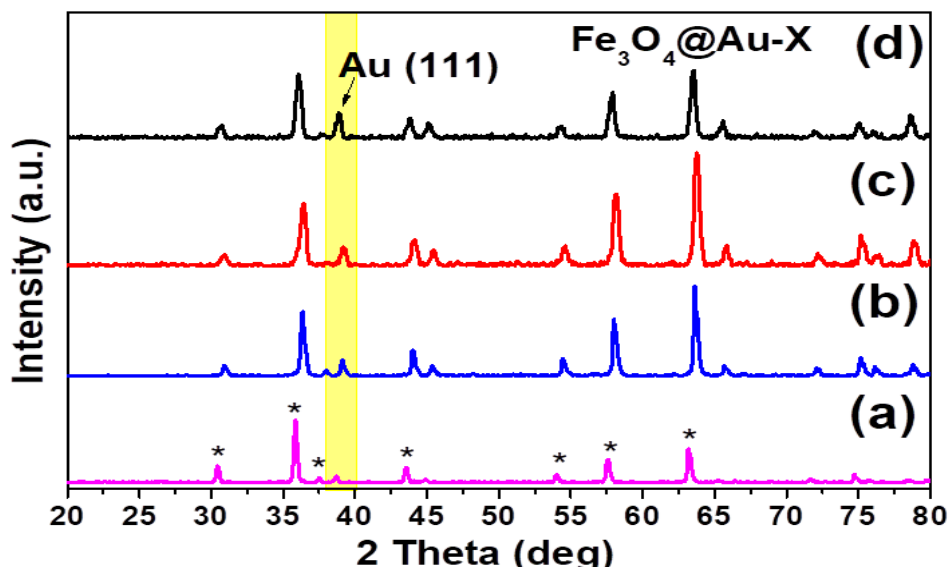


Figure 4.5 XRD patterns of $\text{Fe}_3\text{O}_4@Au-X$ after calcination at 250 °C for 2 h.

4.3.4 XPS studies X-ray photoelectron spectroscopy (XPS) studies were performed to determine the oxidation state of the metal in the calcined samples, and the results are shown in Fig. 4.6.

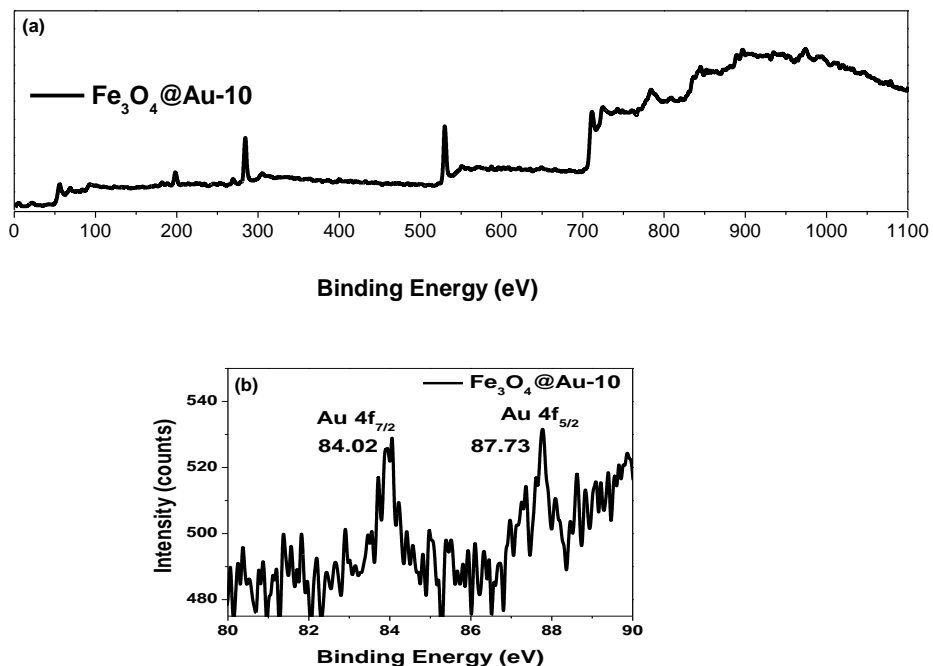


Figure 4.6 (a) Survey scan and (b) Au narrow 4f scan XPS of $\text{Fe}_3\text{O}_4@Au-10$.

The survey scan of the samples showed the presence of the respective metal as well as iron from the magnetite core. The Au 4f core level narrow scan of Fe₃O₄@Au-40 revealed two peaks at 84.02 and 87.73 eV corresponding to Au 4f_{7/2} and Au 4f_{5/2} levels, respectively. These binding energy values along with the separation value of 3.7 eV confirmed the oxidation state of Au to be zero

4.3.5 FE-SEM studies

The FE-SEM analysis of Fe₃O₄@Au-10 (Fig.4.7 (a-c)) clearly revealed the coating of metal over the magnetite core, thus forming a MO@M core-shell nanostructure. In addition to the wavy surface that substantiates the metallic shell formation, a fusion of several magnetite cores mediated by the metal was also observed.

These results confirm the successful fabrication of core-shell nanostructures through the physical grinding approach. The mechanism of the metal shell formation can be envisaged as follows: (i) the surfactant-based precursors possess relatively low melting points that assist in conformal precursor coating over the magnetite core. (ii) The surfactants present in the precursors also help in minimizing the surface energy during the metallization step.

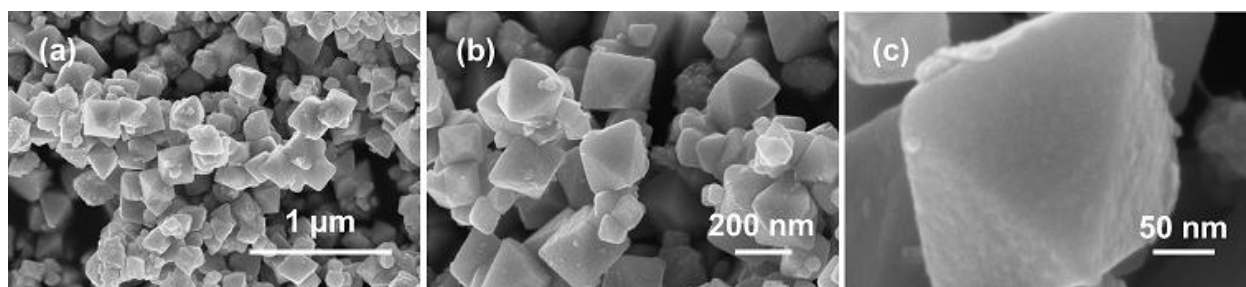


Figure 4.7 FE-SEM images of Fe₃O₄@Au-10 under different magnification

The surface morphology studies using FE-SEM with varying Au content have been shown in Fig 4.3.7. With increasing loading of the Au-TOAB, a few free metal nanoparticles had also been observed along with the core-shell structures (Fig. 4.8 (a and b)). In addition, more metal-mediated inter-particle conjunction was found with increasing precursor loading. In case of Fe₃O₄@Au-40 and Fe₃O₄@Au-50 (Fig. 4.8 (c and d)), several Au nanoneedles were found to

co-exist along with the core-shell nanostructures, indicating a large excess amount of the metal precursor over the magnetite. This excess amount of precursor that may have been segregated resulting in the nanoneedle formation upon decomposition.

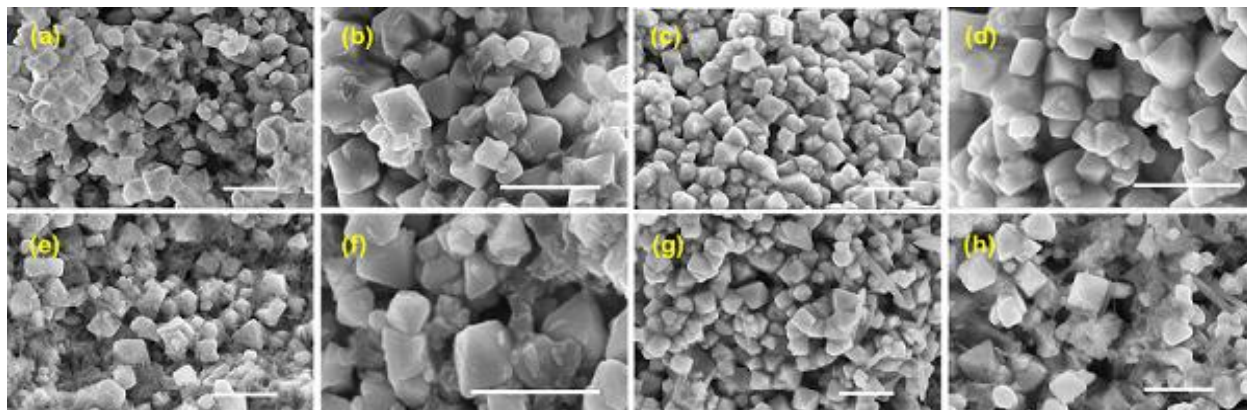


Figure 4.8 Low magnification FE-SEM images of $\text{Fe}_3\text{O}_4@Au-X$, where $X = (a, b) 20, (c, d) 30, (e, f) 40,$ and $(g, h) 50$. Scale bar = 500 nm.

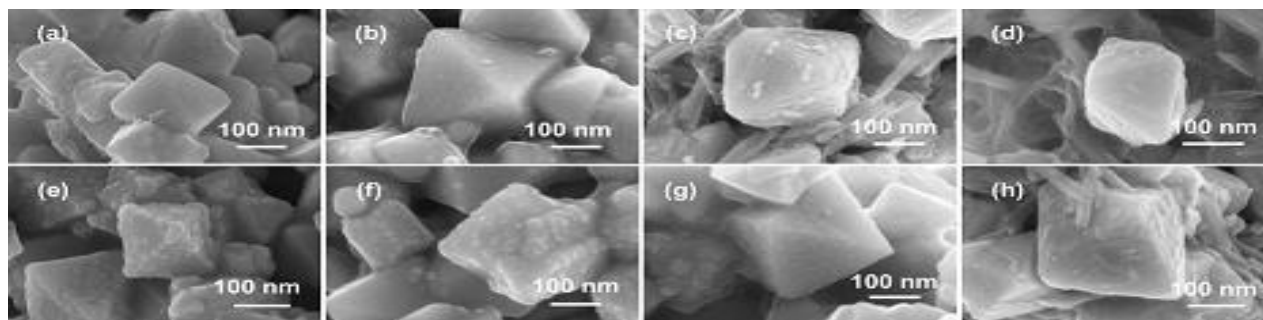


Figure 4.9 High magnification FE-SEM images of $\text{Fe}_3\text{O}_4@Au-X$. Naturally cooled (a) Au-20, (b) Au-30, (c) Au-40, and (d) Au-50; Rapidly cooled (e) Au-10, (f) Au-20, (g) Au-30, and (h) Au-40.

In order to gain insight to the shell formation mechanism, the core-gold precursor assembly was subjected to a rapid cooling by immersing the autoclave into an ice-cold water set up immediately after the 2 h calcination. In the case of $\text{Fe}_3\text{O}_4@Au-10$ (Fig.4.8(e)), several hump type structures in the shell layer of Au was visible over the shell, indicating that the Au-TOAB initially formed nanoparticles during the decomposition step, which further melted or diffused to

form a continuous thin film. With the increment of Au-TOAB as in $\text{Fe}_3\text{O}_4@Au-20$ (Fig.4.8(f)), the rapid cooling revealed relatively lesser amount of humps in the shell, but resulted in more metal-mediated particle aggregation, indicating the higher amount of the Au. In case of $\text{Fe}_3\text{O}_4@Au-40$ (Fig. 4.8(h)), the rapid cooling showed a small number of nanoneedles along with core-shell structures similar to the slow cooling process that reaffirmed the excess amount of Au-TOAB as discussed earlier. These observations can be interpreted in terms of surface energy. The surface energies of Au is 1500 mJ/m^2 .¹⁵ As Au has higher surface energy, it has an inherent tendency to ball up, leading to segregated nanoparticles at higher loadings. The high magnification FE-SEM images of the samples are presented in the Fig 4.9.

4.3.6 HR-TEM

High-resolution transmission electron microscopy (HR-TEM) analysis was performed over selected samples to investigate the surface coverage of the metal shell. The HR-TEM images of $\text{Fe}_3\text{O}_4@Au-10$ showed complete coverage of Fe_3O_4 with Au, confirming the core-shell formation (see in Fig 4.10). The higher magnification image revealed the shell thickness in the range of ~5-9 nm. In the case of $\text{Fe}_3\text{O}_4@Au-40$ core-shell nanostructures were clearly visible.

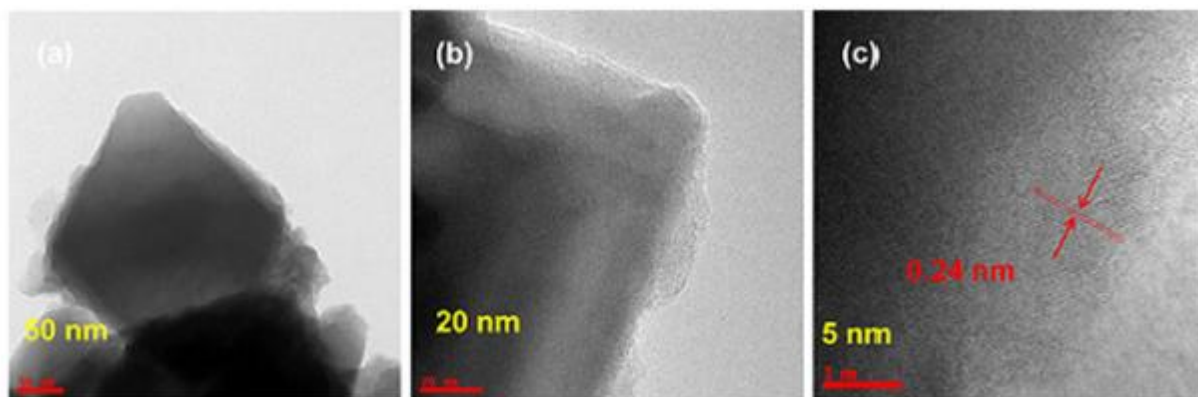


Figure 4.10 HR-TEM images of $\text{Fe}_3\text{O}_4@Au-40$ (a-c) at different magnifications

In these cases, the shell thickness was found to be slightly higher and rougher than that in $\text{Fe}_3\text{O}_4@Au-10$. The respective fringes with lattice spacing of 0.24 nm characteristic of (111) planes of Au corroborated the crystallinity of the metals as confirmed by XRD.

4.3.7 STEM

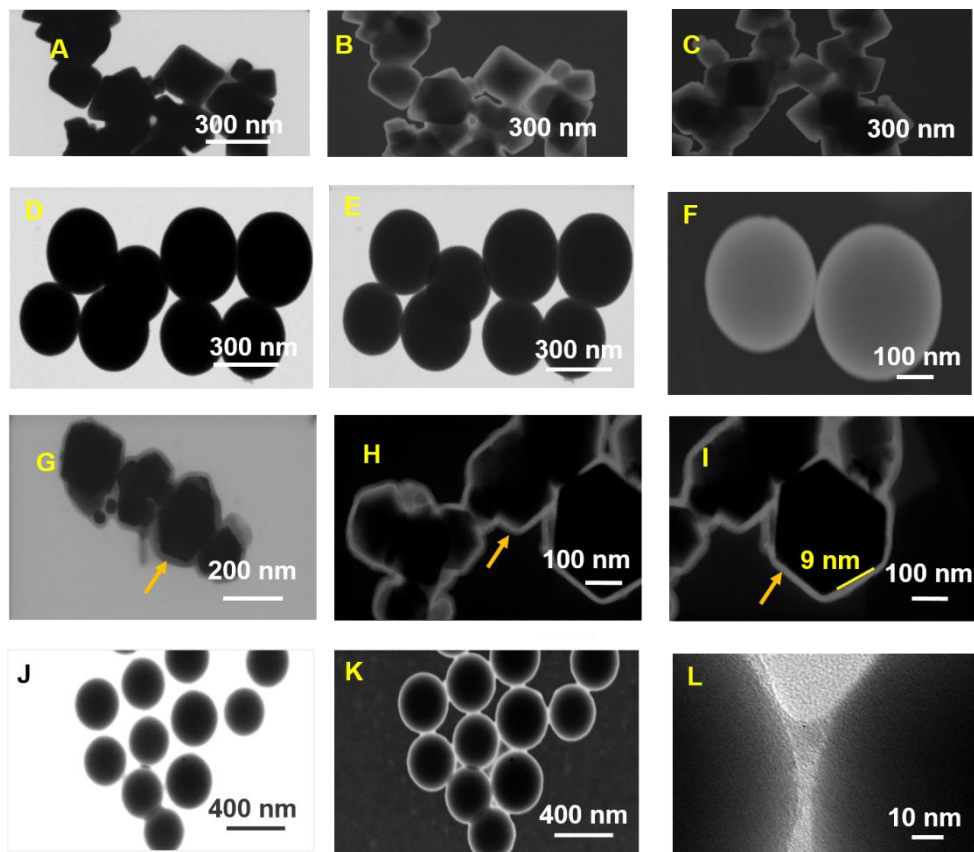


Figure 4.11 STEM images of (a-c) pristine Fe_3O_4 (d-f) SiO_2 (g-i) $\text{Fe}_3\text{O}_4@Au-20$ (j-l) $\text{SiO}_2@Au-40$. The first column are bright field images. The second and third column are composite images obtained in different magnifications.

The STEM analyses of Fe_3O_4 , $\text{Fe}_3\text{O}_4@Au-20$, SiO_2 , and $\text{SiO}_2@Au-40$ (Fig. 4.11) revealed and confirmed a smooth and continuous metal shell layer coating over the core. It is clear that the presence of shell is not evident in bright field images but when the images were made in dark field mode.

4.3.8 BET

Brunauer–Emmett–Teller (BET) surface area measurements on selected samples were performed to understand the effect of precursor loading in inter-particle aggregation. The surface area of the commercial Fe_3O_4 was determined to be $7.5 \text{ m}^2/\text{g}$. Compared to this, $\text{Fe}_3\text{O}_4@Au-10$ showed a decreased surface area of $4.6 \text{ m}^2/\text{g}$, respectively. When the precursor loading was

increased to 40%, the surface area of the corresponding Au samples further decreased to 2.6 m²/g. While the decrease in surface area with the Au metal reveal the occurrence of aggregation, the data also suggest that the aggregation is pronounced to a greater extent in case of Au. This observation is in line with our FE-SEM analyses.

4.3.9 SAXS

Small angle X-ray scattering (SAXS) is a powerful technique that reveals the microstructural information of the sample over a large area. In our study, qualitative SAXS analysis studies were performed for selected materials in order to ascertain the structural details in the nanoscale regime (Fig. 4.12).

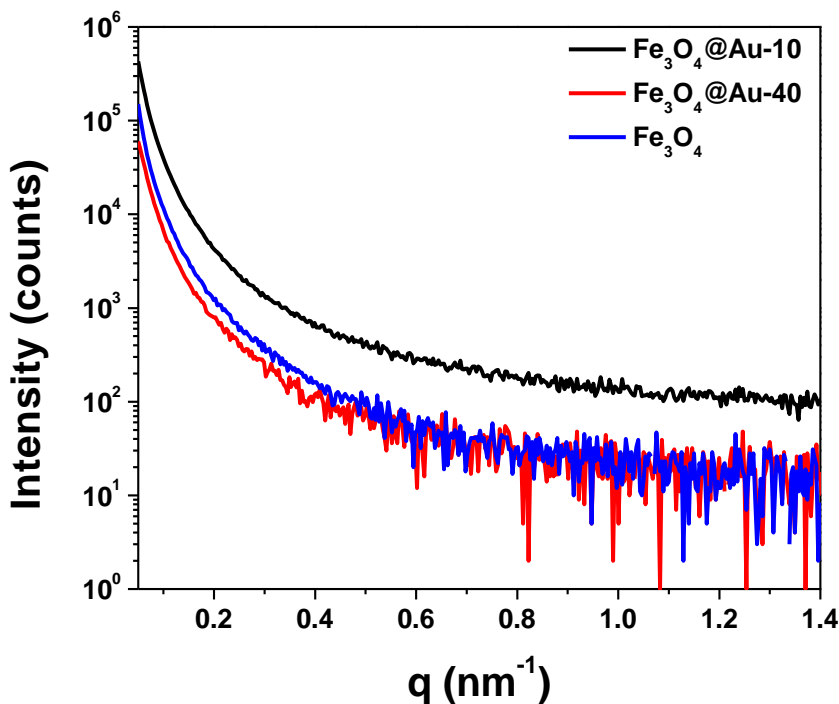


Figure 4.12 SAXS data for Fe₃O₄, Fe₃O₄@Au-10, Fe₃O₄@Au-40 samples.

The scattering intensity is dependent on two factors: the constituent elements present and the sample thickness. It is known that the scattering generally increases with increasing atomic number. Pristine Fe₃O₄ was used as the control material for discussion. In the case of Au shell materials, the scattering intensity of Fe₃O₄@Au-10 was more than the pristine Fe₃O₄ at all q

values. Au has a higher atomic number and therefore expected to have higher scattering. Thus, the observation indicates that the pristine Fe₃O₄ is completely modified on the surface due to the formation of the Au shell layer. With the increase in Au content further as in Fe₃O₄@Au-40, the scattering intensity was found to be less than both pristine Fe₃O₄ and Fe₃O₄@Au-10. And, at high q values, it was difficult to differentiate the scattering between the pristine Fe₃O₄ and Fe₃O₄@Au-10 samples. The linear absorption coefficient μ is defined as $-\ln(I_s/I_0)t$, where I_s is the maximum intensity of the sample, I_0 is the maximum intensity without the sample and t is the thickness of the sample. As the sample was smeared over the scotch tape, any change in I_s can be attributed to the change in the μ value. Thus, the observed decrease in the scattering intensity (I_s) with the increase in Au loading is due to the increase in μ , which signifies the increasing Au shell thickness.

4.4 Conclusion

We have shown a solid-state synthetic approach to fabricate Fe₃O₄@Au core-shell nanostructures leading to gram scale synthesis in the laboratory conditions. Extensive characterizations using XRD, XPS, ED-XRF, FE-SEM, and HR-TEM analyses have confirmed the successful synthesis of Fe₃O₄@M core-shell nanostructures. Furthermore, qualitative SAXS analyses have revealed continuous metal shell formation and thus confirming the core-shell architecture present over a large area of the sample.

4.5 References

1. Kwizera, E. A.; Chaffin, E.; Wang, Y.; Huang, X., Synthesis and properties of magnetic-optical core-shell nanoparticles. *RSC advances* **2017**,7 (28), 17137-17153.
2. Talapin, D. V.; Rogach, A. L.; Kornowski, A.; Haase, M.; Weller, H., Highly luminescent monodisperse CdSe and CdSe/ZnS nanocrystals synthesized in a hexadecylamine-trioctylphosphine oxide-trioctylphosphine mixture. *Nano letters* **2001**,1 (4), 207-211.
3. Kondrat, S. A.; Shaw, G.; Freakley, S. J.; He, Q.; Hampton, J.; Edwards, J. K.; Miedziak, P. J.; Davies, T. E.; Carley, A. F.; Taylor, S. H., Physical mixing of metal acetates: a simple, scalable method to produce active chloride free bimetallic catalysts. *Chemical Science* **2012**,3 (10), 2965-2971.
4. Gates, B., Supported metal clusters: synthesis, structure, and catalysis. *Chemical reviews* **1995**,95 (3), 511-522.

5. Saiz, E.; Tomsia, A.; Cannon, R., Ridging effects on wetting and spreading of liquids on solids. *Acta Materialia* **1998**,*46* (7), 2349-2361.
6. Saiz, E.; Cannon, R. M.; Tomsia, A. P., High-temperature wetting and the work of adhesion in metal/oxide systems. *Annu. Rev. Mater. Res.* **2008**,*38*, 197-226.
7. Chen, K.-L.; Yeh, Y.-W.; Chen, J.-M.; Hong, Y.-J.; Huang, T.-L.; Deng, Z.-Y.; Wu, C.-H.; Liao, S.-H.; Wang, L.-M., Influence of magnetoplasmonic γ -Fe₂O₃/Au core/shell nanoparticles on low-field nuclear magnetic resonance. *Scientific reports* **2016**,*6*, 35477.
8. Mohammad, F.; Balaji, G.; Weber, A.; Uppu, R. M.; Kumar, C. S., Influence of gold nanoshell on hyperthermia of superparamagnetic iron oxide nanoparticles. *The Journal of Physical Chemistry C* **2010**,*114* (45), 19194-19201.
9. Khashan, S.; Dagher, S.; Tit, N.; Alazzam, A.; Obaidat, I., Novel method for synthesis of Fe₃O₄@TiO₂ core/shell nanoparticles. *Surface and Coatings Technology* **2017**,*322*, 92-98.
10. Levin, C. S.; Hofmann, C.; Ali, T. A.; Kelly, A. T.; Morosan, E.; Nordlander, P.; Whitmire, K. H.; Halas, N. J., Magnetic– plasmonic core– shell nanoparticles. *ACS nano* **2009**,*3* (6), 1379-1388.
11. Sharma, R. K.; Dutta, S.; Sharma, S.; Zboril, R.; Varma, R. S.; Gawande, M. B., Fe₃O₄ (iron oxide)-supported nanocatalysts: synthesis, characterization and applications in coupling reactions. *Green Chemistry* **2016**,*18* (11), 3184-3209.
12. Efremova, M. V.; Naumenko, V. A.; Spasova, M.; Garanina, A. S.; Abakumov, M. A.; Blokhina, A. D.; Melnikov, P. A.; Prelovskaya, A. O.; Heidelmann, M.; Li, Z.-A., Magnetite-Gold nanohybrids as ideal all-in-one platforms for theranostics. *Scientific reports* **2018**,*8* (1), 1-19.
13. Ma, Y.; Li, W.; Cho, E. C.; Li, Z.; Yu, T.; Zeng, J.; Xie, Z.; Xia, Y., Au@Ag core– shell nanocubes with finely tuned and well-controlled sizes, shell thicknesses, and optical properties. *ACS nano* **2010**,*4* (11), 6725-6734.
14. Radha, B.; Kiruthika, S.; Kulkarni, G., Metal anion–alkyl ammonium complexes as direct write precursors to produce nanopatterns of metals, nitrides, oxides, sulfides, and alloys. *Journal of the American Chemical Society* **2011**,*133* (32), 12706-12713.
15. Vitos, L.; Ruban, A.; Skriver, H. L.; Kollar, J., The surface energy of metals. *Surface science* **1998**,*411* (1-2), 186-202.

Chapter 5

Solid-state synthetic approach for the fabrication of Fe₃O₄@Ag Nanostructures

5.1 Introduction

This chapter deals with the synthesis of $\text{Fe}_3\text{O}_4@Ag$ nanostructures. The results obtained for structural, chemical, microstructural, and magnetic characterization results by using TGA-DTA, XRD, XRF, XPS, FE-SEM, BET, HR-TEM, STEM, SAXS, VSM techniques are discussed. To demonstrate the versatility of the method, $\text{SiO}_2@Ag$ nanostructures were prepared and the respective data are also presented.

Solid-state synthetic approach for the fabrication of $\text{Fe}_3\text{O}_4@Ag$ core-shell nanostructures in nearly quantitative yields that involves a simple physical grinding of a metal precursor over Fe_3O_4 core, followed by calcination. The process involves smooth coating of low melting hybrid organic-inorganic precursor over the Fe_3O_4 core, which in turn facilitates a continuous shell layer post thermolysis. Silver has been chosen due to its dominant plasmonic and anti-microbial properties.¹⁻⁷ Anti-microbial properties, biocompatibility of silver nanoparticles (AgNP's) mainly due to release of Ag^+ ions into the surroundings^{8,9}. $\text{Ag}@Fe_3\text{O}_4$ core-shell structure has stronger bactericidal efficiency than $\text{Ag-Fe}_2\text{O}_3$ heterodimers or plain Ag ¹². The possible explanation of this finding is due to release of Ag^+ ions from amorphous thin oxide shell in comparison to organic-wrapped Ag nano particles

We hypothesized that coating a noble metal-containing surfactant-based precursor over an oxide core as a thin film followed by metallization would result in a continuous metal shell formation. Therefore, keeping the coatability in mind, silver N-lauryl sarcosinate (Ag-NLS) for Ag have been chosen. Since surfactants possessing amphiphilic properties are known to form good quality films, N-lauryl sarcosinate derivative of silver was synthesized.

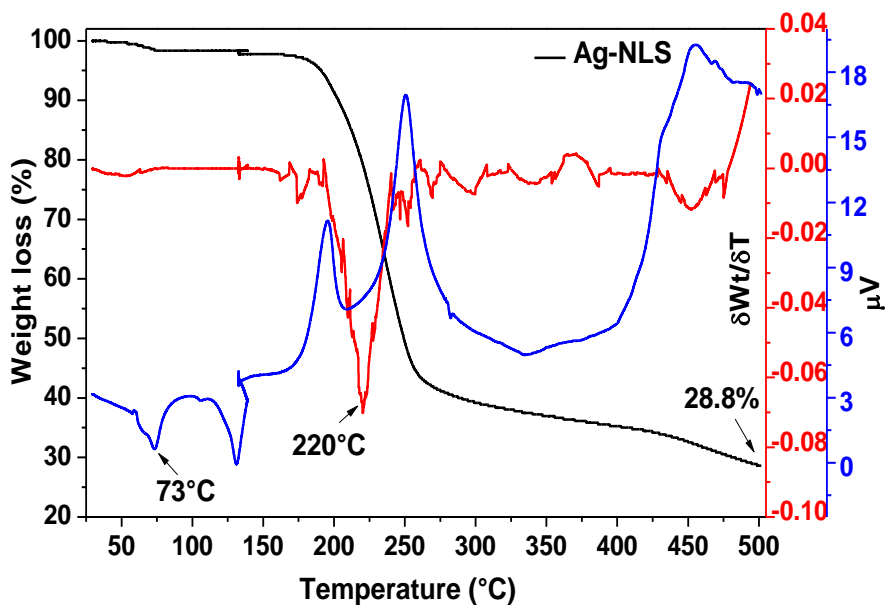
5.2 Experimental details

5.2.1 Materials. Commercial Fe_3O_4 obtained from Aldrich was chosen to be the core particles. SiO_2 was prepared by adopting Stober's method. The commercial Fe_3O_4 had a regular octahedron and SiO_2 had a spherical morphology. The particle dimension was approximately around 250 nm in both core materials. Ag-NLS was synthesized by adding a stoichiometric amount of saturated sodium N-lauryl sarcosinate solution to a solution of AgNO_3 in a water-ethanol mixture. The obtained white precipitate was washed thoroughly and dried under vacuum

for overnight. Since surfactants possessing amphiphilic properties are known to form good quality films, N-lauryl sarcosinate derivative of silver was synthesized.

5.2.2 Synthesis procedure. In a typical core-shell synthesis using our solid-state approach, a calculated amount of the metal precursor, Ag-NLS was mixed with the magnetite core followed by thorough grinding for 10 min in order to achieve a uniform coating of the precursor over the Fe_3O_4 core. The obtained mixture was transferred to an autoclave and subjected to calcination at different temperatures for 2 h. An autoclave was used in order to avoid any surface oxidation during metallization. Typically, the core-precursor assembly after the calcination step was allowed to cool naturally inside the furnace, thus ensuring a slow cooling, unless otherwise mentioned. The resultant products have been labeled as $\text{Fe}_3\text{O}_4@M-X$, where M and X represent the metal and the weight percent of its corresponding precursor with respect to the initial Fe_3O_4 content, respectively.

5.3 Results and Discussion



5.3.1 TGA-DTA studies

Figure 5.1. Thermogravimetric and differential thermal analysis of the metal precursors used in this study. Black, red and blue lines represent thermogravimetry, differential thermogravimetry, and differential thermal analysis curves, respectively.

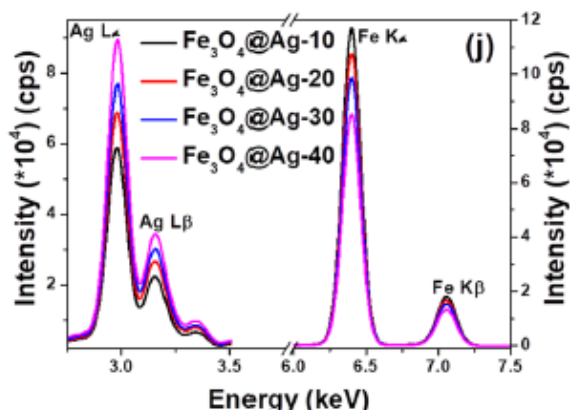
The thermal stability of the precursors has been studied using thermogravimetric and differential thermal analysis. The differential thermal analysis revealed the low melting points of Ag precursors 73 °C. The thermal decomposition and the corresponding derivative plot of the precursors are given in the Fig. 5.1. The onset of the thermal decomposition in these precursors was found to be close to 180 °C and the major mass loss was found to occur between 220 and 250 °C. Based on the derivative plot, the lowest calcination temperature in this study had been fixed at 250 °C. The calculated and experimental residual mass of the metals in the corresponding precursors is given in Table 5.1.

Table 5.1. Calculated and experimental metal content (wt.%) in the Ag precursor used in this study.

Sample Code	Calculated	Experimental
Ag-NLS	28.5	28.8

5.3.2 XRF studies

Figure 5.2 shows the ED-XRF spectra for Fe₃O₄@Ag-X. The intensity at the Ag L α at 2.98 keV was systematically increasing with Ag loading. The peak intensities fit linearly with



increasing the noble metal content, which confirms that the composition of the resultant core-shell nanostructures is as per the feed ratio.

Figure 5.2 ED-XRF spectra of $\text{Fe}_3\text{O}_4@\text{Ag-X}$. The respective edges are marked for Fe and Au. The y-axis on the left is for Fe and the one on the right is for Au.

5.3.3 XRD studies

The powder X-ray diffraction (XRD) patterns of the products obtained from the commercial Fe_3O_4 mixed with Ag-NLS (e-h) by calcining at 250 °C for 2 h is given in Fig. 5.3. It can be observed from the figure that along with the inverse spinel magnetite phase, the characteristic peaks for (111) planes of Ag was also observed. As expected, the relative intensity of (111) plane increased with increasing metal precursor loading. This is indicative of the increase in Ag content as per the increasing feed ratio.

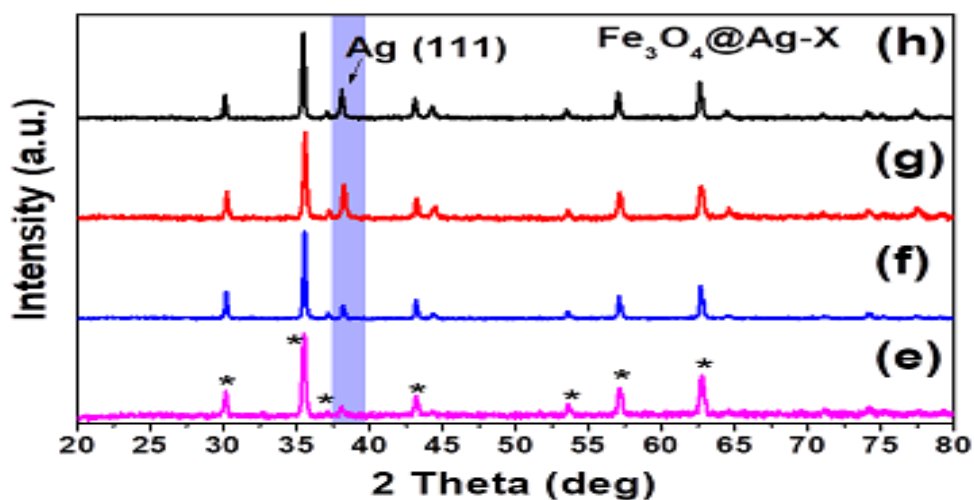


Figure 5.3 XRD patterns of $\text{Fe}_3\text{O}_4@\text{Ag-X}$ obtained after calcination at 250 °C for 2 h.

5.3.4 XPS studies

X-ray photoelectron spectroscopy (XPS) studies were performed to determine the oxidation state of the metal in the calcined samples, and the results are shown in Fig.5.4. The survey scan of the samples showed the presence of the respective metal as well as iron from the magnetite core. The Ag 3d core level narrow scan of $\text{Fe}_3\text{O}_4@\text{Ag-10}$ showed the characteristic Ag 3d_{5/2} and Ag 3d_{3/2} peaks at 367.6 and 373.52 eV, respectively. In this case, the binding energy

values and their separation (~6 eV) confirmed the presence of Ag in its (+1) oxidation state as in Ag₂O. It is known that the surface of silver gets oxidized upon exposure to air. Since XPS is a surface sensitive technique, it reveals the presence of silver oxide in the surface, while XRD ascertained the bulk film (in the shell layer) as metallic silver.

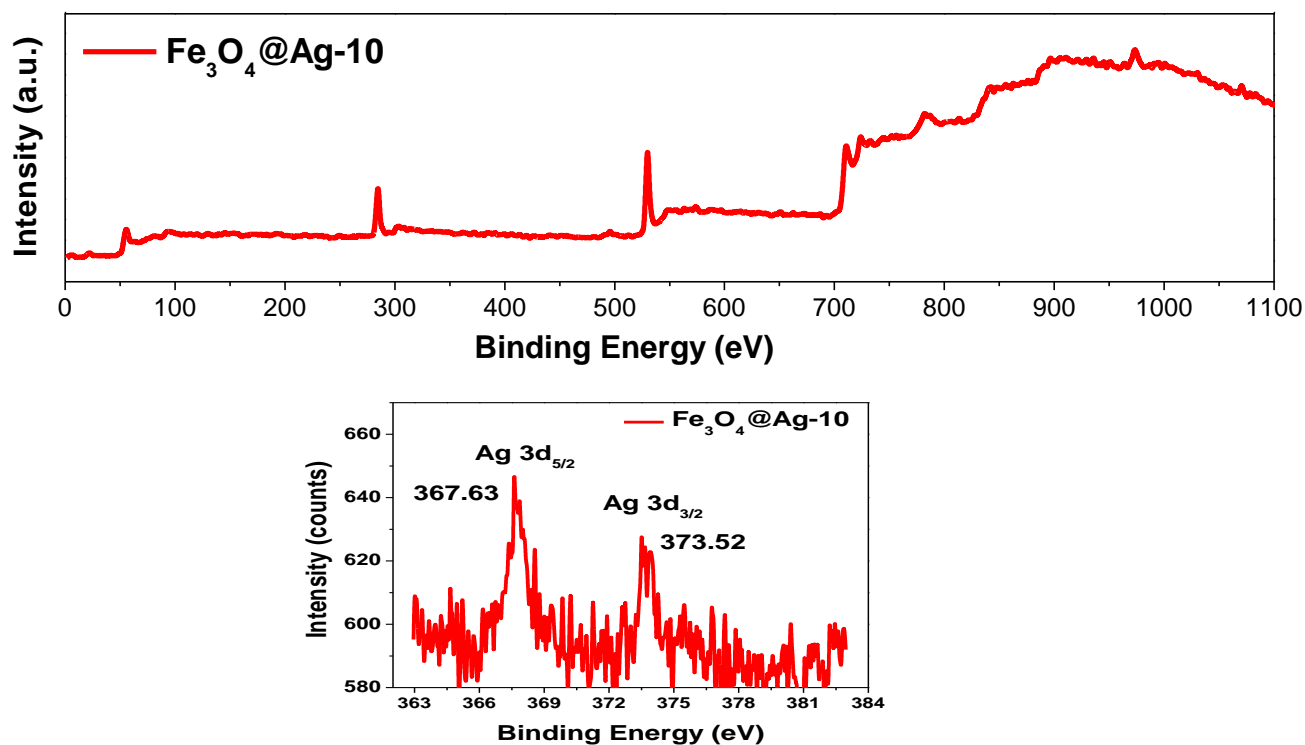


Figure 5.4. XPS survey (top panel) and narrow (bottom panel) scan of Fe₃O₄@Ag-10

5.3.5 FE-SEM studies

The field emission scanning electron microscopy (FE-SEM) images of and Fe₃O₄@Ag-10 (see Fig. 5.5) clearly revealed the coating of metal over the magnetite core, thus forming a MO@M core-shell nanostructure. In addition to the wavy surface that substantiates the metallic shell formation, a fusion of several magnetite cores mediated by the metal was also observed. These results confirm the successful fabrication of core-shell nanostructures through the physical grinding approach. The mechanism of the metal shell formation can be envisaged as follows: (i) the surfactant-based precursors possess relatively low melting points that assist in conformal

precursor coating over the magnetite core. (ii) The surfactants present in the precursors also help in minimizing the surface energy during the metallization step.

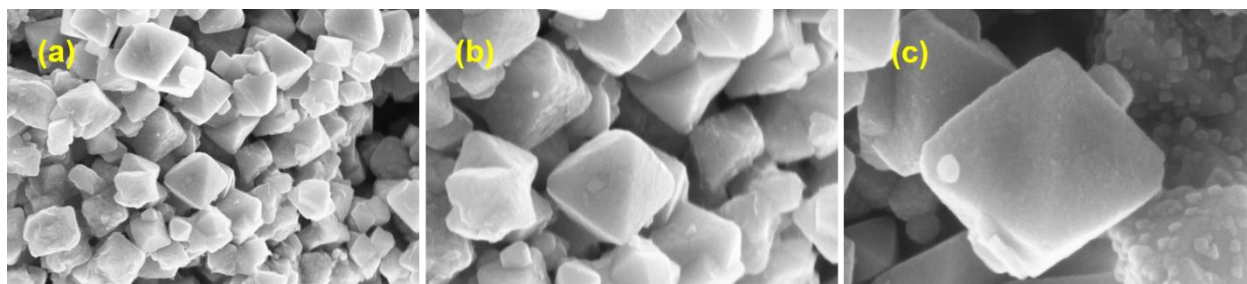


Figure 5.5 Field emission scanning electron microscopy (FE-SEM) images of $\text{Fe}_3\text{O}_4@Ag-10$ at different magnifications.

In the case of silver systems, the shell was found to be much smoother than in the case of gold (Fig. 4.7). It is noteworthy that the FE-SEM images of $\text{Fe}_3\text{O}_4@Ag-20$, $\text{Fe}_3\text{O}_4@Ag-30$, $\text{Fe}_3\text{O}_4@Ag-40$, and $\text{Fe}_3\text{O}_4@Ag-50$ (Fig. 5.6) revealed a much smoother Ag coating over the magnetite core even at this high loading.

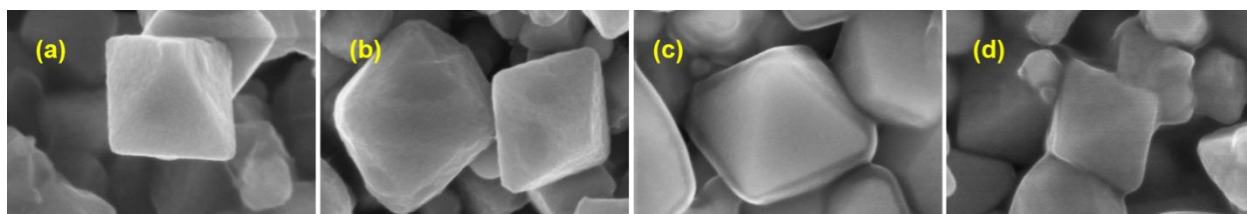


Figure 5.6 FE-SEM images of (a) $\text{Fe}_3\text{O}_4@Ag-20$, (b) $\text{Fe}_3\text{O}_4@Ag-30$, (c) $\text{Fe}_3\text{O}_4@Ag-40$, and (d) $\text{Fe}_3\text{O}_4@Ag-50$.

However, the metal-mediated aggregation of the core-shell nanostructures with an increase in metal precursor loading was evident. These observations can be interpreted in terms of surface energy. The surface energy of Ag is $\sim 1250 \text{ mJ/m}^2$.¹³ As Au has higher surface energy (section 4.3.5), it has an inherent tendency to ball up, leading to segregated nanoparticles at higher loadings. Although Ag also has a similar surface energy, its oxidized form is known to possess surface energy in the range of 30 to 50 mJ/m^2 .⁴³ Therefore, the formation of thin oxide layer (evidenced by XPS) on the very surface of Ag shell could have further assisted in minimizing the surface energy, which could have additionally contributed for a relatively smoother shell surface

with less aggregation, when compared to Au. The low magnification FE-SEM images of the samples are presented in the fig 5.7.

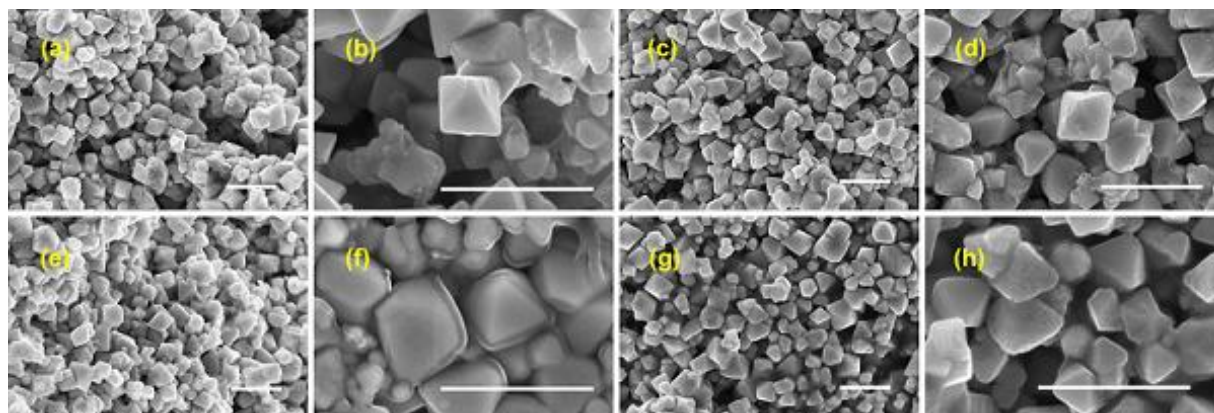


Figure 5.7 Low magnification FE-SEM images of $\text{Fe}_3\text{O}_4@Ag-X$, where $X = (a, b) 20, (c, d) 30, (e, f) 40,$ and $(g, h) 50$. Scale bar = 500 nm.

5.3.6 HR-TEM studies

High-resolution transmission electron microscopy (HR-TEM) analysis was performed over selected samples to investigate the surface coverage of the metal shell. The HR-TEM images of $\text{Fe}_3\text{O}_4@Ag-10$ (Fig, 5.8) showed complete coverage of Fe_3O_4 with Ag, confirming the core-shell formation. The higher magnification image revealed the shell thickness in the range of $\sim 5-9$ nm. $\text{Fe}_3\text{O}_4@Ag-40$, such core-shell nanostructures were clearly visible.

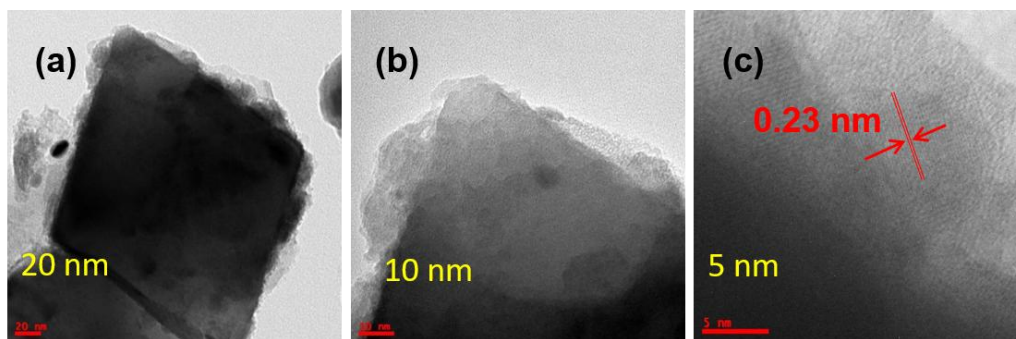


Figure 5.8. HR-TEM images of $\text{Fe}_3\text{O}_4@Ag-10$ (a-c) at different magnifications.

In these cases, the shell thickness was found to be slightly higher and rougher than that in $\text{Fe}_3\text{O}_4@\text{Ag}-10$. The respective fringes with lattice spacing of 0.23 nm characteristic of (111) planes of Ag corroborated the crystallinity of the metals as confirmed by XRD (see fig 5.8).

5.3.7 STEM studies

The STEM analyses of $\text{Fe}_3\text{O}_4@\text{Ag}-20$, and $\text{SiO}_2@\text{Ag}-40$ (Fig. 5.9) revealed and confirmed a smooth and continuous metal shell layer coating over the core. It is clear that the presence of shell is not evident in bright field images but when the images were made in dark field mode.

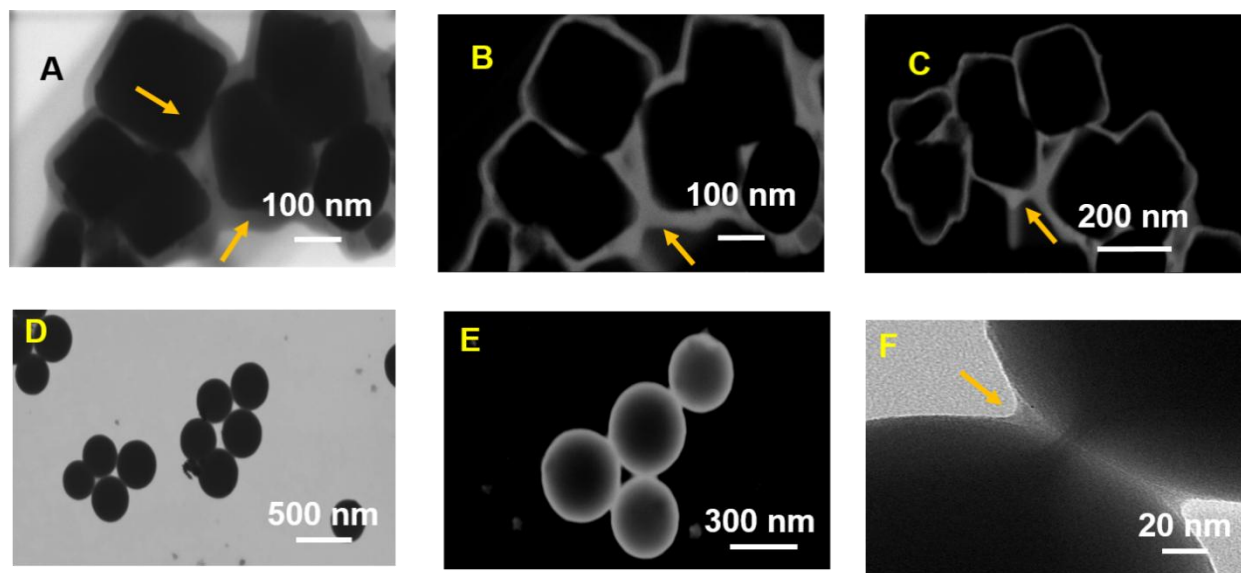


Figure 5.9 STEM images of (a-c) $\text{Fe}_3\text{O}_4@\text{Ag}-20$ (j-l) $\text{SiO}_2@\text{Ag}-40$. The first column are bright field images. The second and third column are composite images obtained in different magnifications.

5.3.8 BET studies

The surface area of the commercial Fe_3O_4 was determined to be $7.5 \text{ m}^2/\text{g}$. Compared to this, $\text{Fe}_3\text{O}_4@\text{Ag}-10$ showed a decreased surface area $4.9 \text{ m}^2/\text{g}$. When the precursor loading was increased to 40%, the surface area of the corresponding Ag samples further decreased to $3.9 \text{ m}^2/\text{g}$, respectively. While the decrease in surface area with both the metals reveal the occurrence

of aggregation, the data also suggest that the aggregation is pronounced to a greater extent in case of Au. This observation is in line with our FE-SEM analyses.

5.3.9 SAXS studies

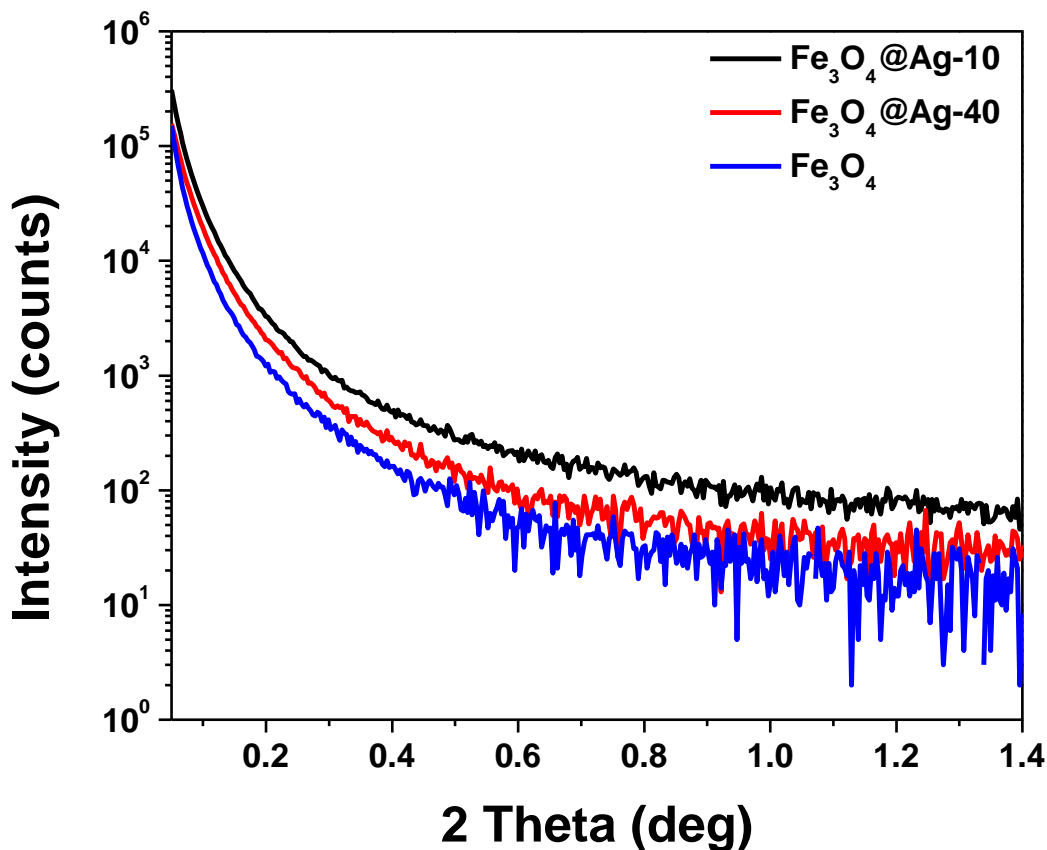


Figure 5.10 SAXS data for Fe_3O_4 , $\text{Fe}_3\text{O}_4@Ag-10$, $\text{Fe}_3\text{O}_4@Ag-40$ samples

As mentioned in section 4.2.9, the scattering intensity is dependent on two factors: the constituent elements present and the sample thickness. In the case of Ag shell materials, the scattering intensity of $\text{Fe}_3\text{O}_4@Ag-10$ was more than the pristine Fe_3O_4 at all q values. Ag has a higher atomic number and therefore expected to have higher scattering. Thus, the observation indicates that the pristine Fe_3O_4 is completely modified on the surface due to the formation of the Ag shell layer. With the increase in Ag content further as in $\text{Fe}_3\text{O}_4@Ag-40$ (Fig. 5.10), the scattering intensity was found to be in between pristine Fe_3O_4 and $\text{Fe}_3\text{O}_4@Ag-10$. And, at high q values, it was difficult to differentiate the scattering between the two Ag samples. The linear

absorption coefficient μ is defined as $-\ln(I_s/I_0)t$, where I_s is the maximum intensity of the sample, I_0 is the maximum intensity without the sample and t is the thickness of the sample. As the sample was smeared over the scotch tape, any change in I_s can be attributed to the change in the μ value. Thus, the observed decrease in the scattering intensity (I_s) with the increase in Ag loading is due to the increase in μ , which signifies the increasing Ag shell thickness.

5.4 Conclusion

We have shown a solid-state synthetic approach to fabricate $\text{Fe}_3\text{O}_4@Ag$ core-shell nanostructures leading to gram scale synthesis in the laboratory conditions. Extensive characterizations using XRD, XPS, ED-XRF, FE-SEM, and HR-TEM analyses have confirmed the successful synthesis of $\text{Fe}_3\text{O}_4@M$ core-shell nanostructures. A qualitative scattering intensity analysis of SAXS data have revealed continuous metal shell formation.

5.5 References

1. Park, H.-Y.; Schadt, M. J.; Wang, L.; Lim, I.-I. S.; Njoki, P. N.; Kim, S. H.; Jang, M.-Y.; Luo, J.; Zhong, C.-J., Fabrication of magnetic core@ shell Fe oxide@ Au nanoparticles for interfacial bioactivity and bio-separation. *Langmuir* **2007**,*23* (17), 9050-9056.
2. Hu, Y.; Wang, R.; Wang, S.; Ding, L.; Li, J.; Luo, Y.; Wang, X.; Shen, M.; Shi, X., Multifunctional $\text{Fe}_3\text{O}_4@Au$ core/shell nanostars: a unique platform for multimode imaging and photothermal therapy of tumors. *Scientific reports* **2016**,*6* (1), 1-12.
3. Huang, X.; Tang, S.; Liu, B.; Ren, B.; Zheng, N., Enhancing the photothermal stability of plasmonic metal Nanoplates by a core- shell architecture. *Advanced materials* **2011**,*23* (30), 3420-3425.
4. Xue, X.; Sukhotskiy, V.; Furlani, E. P., Optimization of optical absorption of colloids of $\text{SiO}_2@Au$ and $\text{Fe}_3\text{O}_4@Au$ nanoparticles with constraints. *Scientific reports* **2016**,*6*, 35911.
5. Yong, K.-T.; Sahoo, Y.; Swihart, M. T.; Prasad, P. N., Synthesis and plasmonic properties of silver and gold nanoshells on polystyrene cores of different size and of gold–silver core–shell nanostructures. *Colloids and Surfaces A: Physicochemical and Engineering Aspects* **2006**,*290* (1-3), 89-105.

6. Banerjee, M.; Sharma, S.; Chattopadhyay, A.; Ghosh, S. S., Enhanced antibacterial activity of bimetallic gold-silver core-shell nanoparticles at low silver concentration. *Nanoscale* **2011**,*3* (12), 5120-5125.
7. Byers, C. P.; Zhang, H.; Swearer, D. F.; Yorulmaz, M.; Hoener, B. S.; Huang, D.; Hoggard, A.; Chang, W.-S.; Mulvaney, P.; Ringe, E., From tunable core-shell nanoparticles to plasmonic drawbridges: Active control of nanoparticle optical properties. *Science advances* **2015**,*1* (11), e1500988.
8. Morones, J. R.; Elechiguerra, J. L.; Camacho, A.; Holt, K.; Kouri, J. B.; Ramírez, J. T.; Yacaman, M. J., The bactericidal effect of silver nanoparticles. *Nanotechnology* **2005**,*16* (10), 2346.
9. Xu, R.; Ma, J.; Sun, X.; Chen, Z.; Jiang, X.; Guo, Z.; Huang, L.; Li, Y.; Wang, M.; Wang, C., Ag nanoparticles sensitize IR-induced killing of cancer cells. *Cell research* **2009**,*19* (8), 1031-1034.
10. Sotiriou, G. A.; Pratsinis, S. E., Antibacterial activity of nanosilver ions and particles. *Environmental science & technology* **2010**,*44* (14), 5649-5654.
11. Seil, J. T.; Webster, T. J., Antimicrobial applications of nanotechnology: methods and literature. *International journal of nanomedicine* **2012**,*7*, 2767.
12. Chen, Y.; Gao, N.; Jiang, J., Surface Matters: Enhanced Bactericidal Property of Core-Shell Ag-Fe₂O₃ Nanostructures to Their Heteromer Counterparts from One- Pot Synthesis. *Small* **2013**,*9* (19), 3242-3246.
13. Vitos, L.; Ruban, A.; Skriver, H. L.; Kollar, J., The surface energy of metals. *Surface science* **1998**,*411* (1-2), 186-202.

Chapter 6

Solid-state Synthesis of Fe₃O₄@AuAg alloy Core-shell Nanostructures

6.1 Introduction

This chapter deals with the synthesis of $\text{Fe}_3\text{O}_4@AuAg$ nanostructures. The results obtained for structural, chemical, microstructural, magnetic characterization results by using XRD, XRF, XPS, FE-SEM, BET, HR-TEM, STEM, SAXS, VSM techniques are discussed. To demonstrate the versatility of the method, $\text{SiO}_2@Au$ nanostructures were prepared and the respective data are also presented.

The Au/Ag surfactant free core-shell NPs suited for biomedical applications because of higher plasmonic efficiency⁵ and superior electromagnetic enhancement in the visible⁴. Thus, it is important to prepare AuAg alloys with magnetic recoverable functionality stronger Raman^{7, 8} and fluorescence enhancements,¹ higher solar energy conversion efficiencies, and higher refractive index sensitivities. We hypothesized that coating a noble metal-containing surfactant-based precursor over an oxide core as a thin film followed by metallization would result in a continuous metal shell formation. Therefore, keeping the coatability in mind, we used Au-TOAB and Ag-NLS for Au and Ag respectively.

6.2 Experimental details

6.2.1 Materials. Commercial Fe_3O_4 obtained from Aldrich was chosen to be the core particles. SiO_2 was prepared by adopting Stober's method. The commercial Fe_3O_4 had a regular octahedron and SiO_2 had a spherical morphology. The particle dimension was approximately around 250 nm in both core materials. The gold precursor, Au-TOAB were procured from Aldrich. Ag-NLS was prepared as described in section 4.1.

6.2.2 Synthesis procedure. In a typical core-shell synthesis using our solid-state approach, a calculated amount of the Au-TOAB and Ag-NLS were with the magnetite core followed by thorough grinding for 10 min in order to achieve a uniform coating of the precursor over the Fe_3O_4 core. The obtained mixture was transferred to an autoclave and subjected to calcination at different temperatures for 2 h. An autoclave was used in order to avoid any surface oxidation during metallization. Typically, the core-precursor assembly after the calcination step was allowed to cool naturally inside the furnace, thus ensuring a slow cooling, unless otherwise mentioned. The resultant products have been labelled as $\text{Fe}_3\text{O}_4@M-X$, where M and X represent the metal and the weight percent of total precursor added with respect to the initial Fe_3O_4

content, respectively. We further continued to explore the potential of fabricating metal oxide@alloy core-shell nanostructures by making AuAg alloys of different compositions such as 1:3, 1:1 and 3:1 over the Fe_3O_4 core. The total amount of metal precursors was maintained as 20% with respect to Fe_3O_4 .

6.3 Results and Discussion

6.3.1 XRF studies

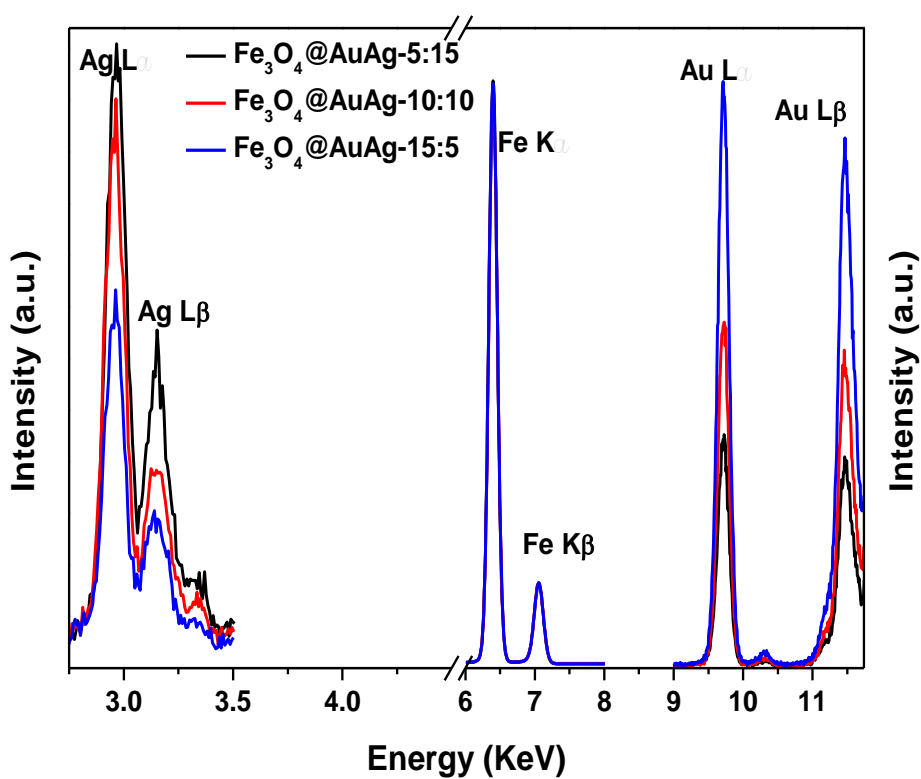


Figure 6.1. ED-XRF spectra of the three different alloy-based core-shell nanostructures.

As mentioned in section 4.2.2 and 5.2.2, ED-XRF was employed to study the composition and the peak intensities fit linearly with increasing the noble metal content, which confirms that the composition of the resultant core-shell nanostructures is as per the feed ratio.

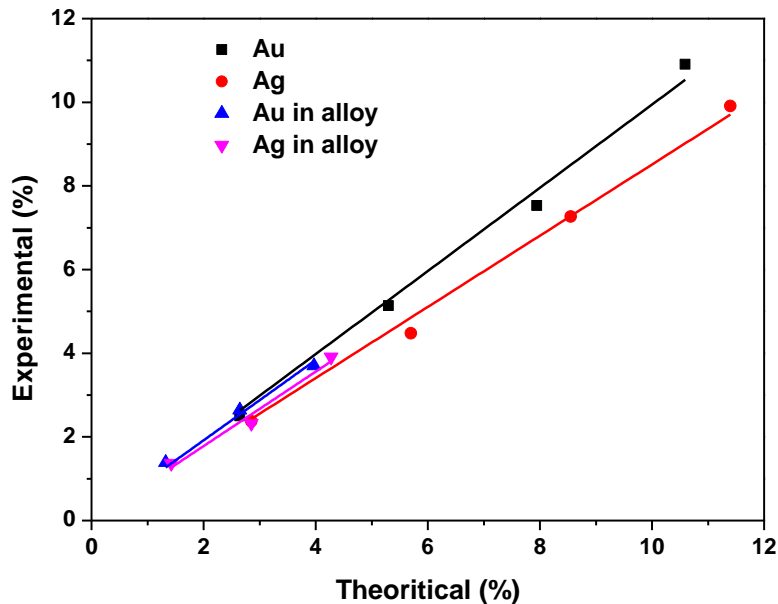


Figure 6.2 The calculated theoretical and observed variation of intensity at respective Au and Ag edge as a function of corresponding composition in the core-shell nanostructures.

The variation of intensity at respective Au and Ag edge as a function of corresponding composition in the core-shell nanostructures is shown in figure 6.2. The percentage determined from XRF almost matched with the calculated intensity. And in the case of AuAg alloy nanostructures the observed intensity matched well with expected value indicating again that the initial feed ratio is maintained.

6.3.2 XRD studies

The XRD results showed that the peak of (111) plane of the AuAg alloy was positioned between the 2θ values of pure Au and Ag (see Fig. 6.3). For these alloys, the ED-XRF showed that the Au $L\alpha$ peak was increasing with Au content in the alloy and simultaneously showing the decrease in the intensity of Ag $L\alpha$ peak (see Fig.6.1).

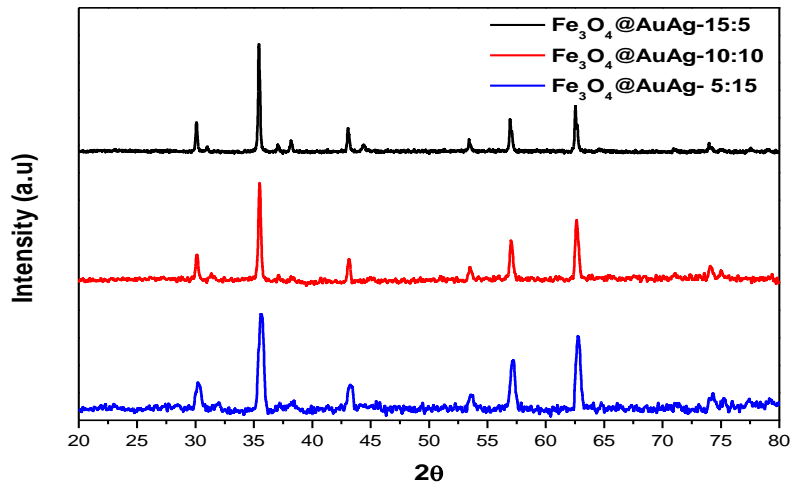


Figure 6.3. XRD patterns of the three different alloy-based core-shell nanostructures.

6.3.3 FE-SEM studies

The FE-SEM analyses (Fig 6.4) have shown smooth coverage (lower surface energy due to silver oxidation) of the AuAg alloy as a shell layer on top of the Fe_3O_4 core (Fig. 6.4(a-c)). To ascertain the reproducibility and credibility of this solid-state approach for alloys, we synthesized $\text{SiO}_2@AuAg-10:10$. The characterization details such as XRD, ED-XRF, STEM and surface area analyses have been presented in the Fig 6.5.

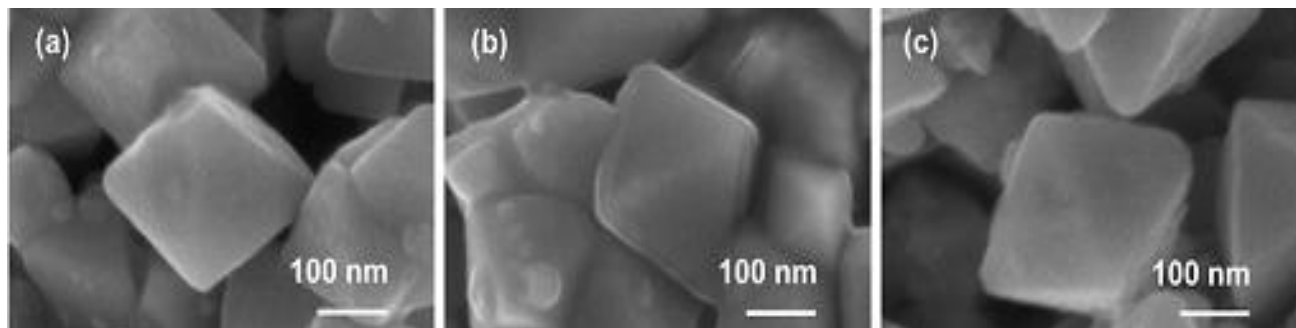


Figure 6.4. FE-SEM AuAg alloy as a shell layer on top of the Fe_3O_4 core (a) $\text{Fe}_3\text{O}_4@AuAg-15:5$, (b) $\text{Fe}_3\text{O}_4@AuAg-10:10$ and (c) $\text{Fe}_3\text{O}_4@AuAg-5:15$ nanostructures.

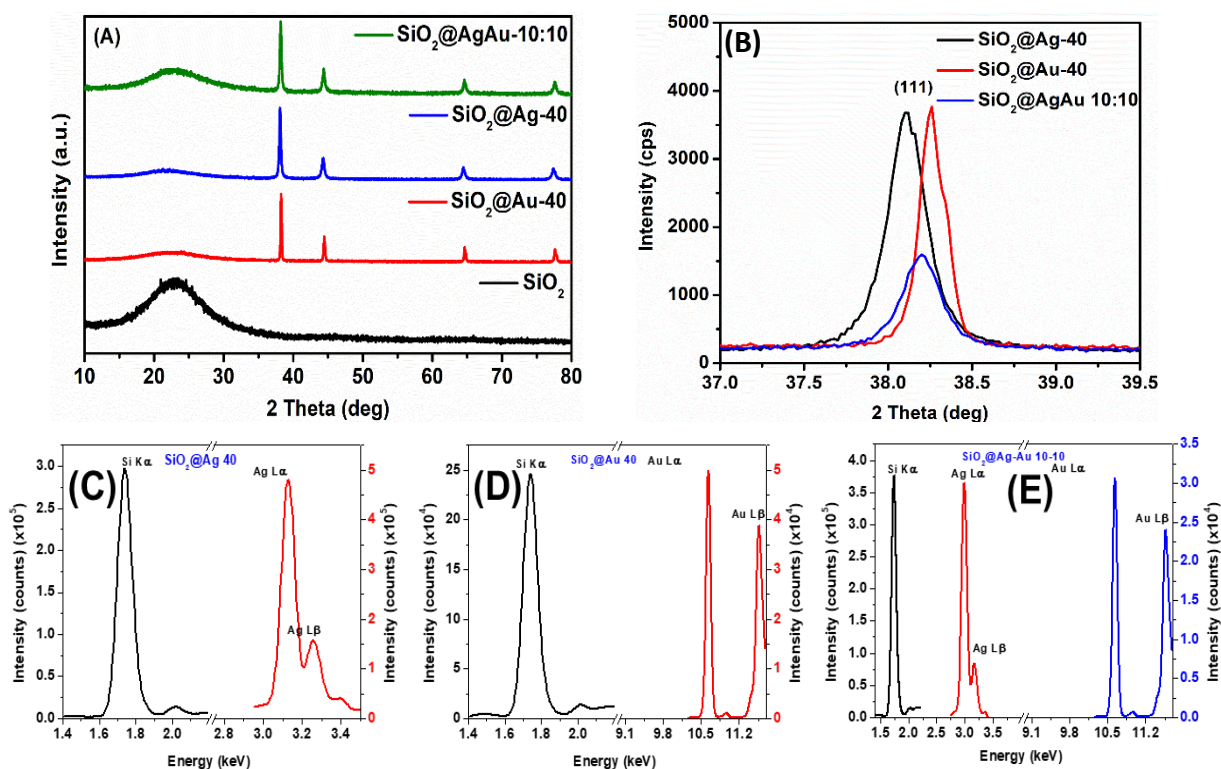


Figure 6.5. (A) The XRD patterns of $\text{SiO}_2\text{@AgAu-10:10}$, $\text{SiO}_2\text{@Ag-40}$, $\text{SiO}_2\text{@Au-40}$ and pristine SiO_2 . (B) The magnified plot of (111) XRD planes for each catalyst to compare the variation of peak position with composition. (C), (D) and (E) ED-XRF spectra of $\text{SiO}_2\text{@Ag-40}$, $\text{SiO}_2\text{@Au-40}$, and $\text{SiO}_2\text{@AgAu-10:10}$, respectively.

The XRD patterns of $\text{SiO}_2\text{@M}$ clearly revealed the presence of respective metals and alloys (after washing with aqueous ammonia). The magnified view of the (111) planes revealed a systematic shift in peak position with respect to the composition. The ED-XRF spectra confirmed the presence of metals with respect to the feed ratio. The low magnification images of $\text{Fe}_3\text{O}_4\text{@AuAg}$ alloy nanostructures have been given in Fig. 6.6.

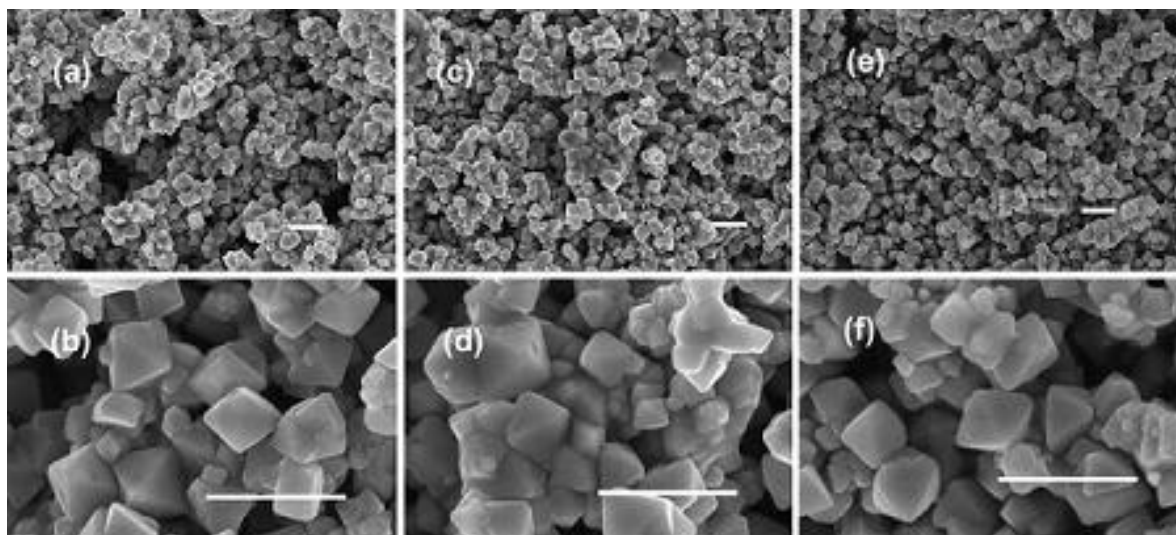


Figure 6.6. Low magnification FE-SEM images of (a, b) $\text{Fe}_3\text{O}_4@AuAg-15:5$, (c, d) $\text{Fe}_3\text{O}_4@AuAg-10:10$ and (e, f) $\text{Fe}_3\text{O}_4@AuAg-5:15$ alloy core-shell nanostructures. Scale bar = 500 nm.

6.3.4 HRTEM studies:

The HRTEM images for alloys $\text{Fe}_3\text{O}_4@AuAg-10:10$ is given in Fig. 6.7. A relatively smooth surface is visible and can be attributed due to the presence of Ag and the surface oxidation of Ag. These results corroborates FE-SEM data.

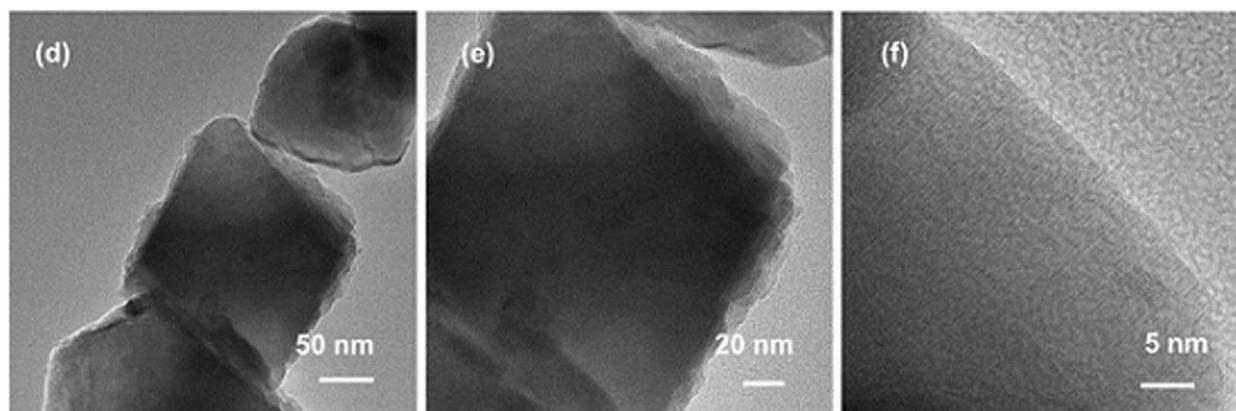


Figure 6.7. HR-TEM images (d–f) with various magnifications of $\text{Fe}_3\text{O}_4@ \text{AuAg-10:10}$ under various magnifications.

6.3.5 STEM studies

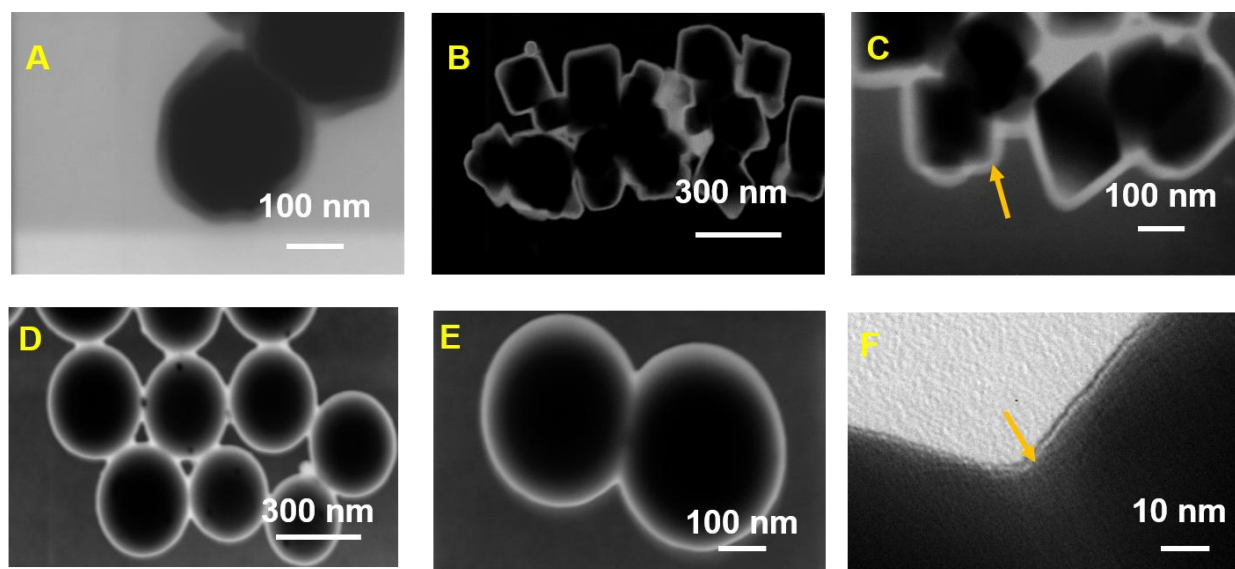


Figure 6.8. Composite STEM images of (A-C) $\text{Fe}_3\text{O}_4@ \text{AuAg-10:10}$ and (D-F) $\text{SiO}_2@ \text{Ag-10:10}$ under different magnifications.

The STEM analyses of Fe_3O_4 , $\text{Fe}_3\text{O}_4@ \text{AuAg-10:10}$ and $\text{SiO}_2@ \text{AuAg-10:10}$ (Fig. 6.8) revealed and confirmed a smooth and continuous metal shell layer coating over the core. It is clear that the presence of shell is not evident in bright field images but when the images were made in dark field mode the illumination at the surface indicates the metal shell. The uniformity indicates that Au and Ag do not segregate but form uniform alloy.

6.3.6 SAXS studies

The scattering intensity is dependent on two factors: the constituent elements present and the sample thickness. It is known that the scattering generally increases with increasing atomic number. Pristine Fe_3O_4 was used as the control material for discussion. Thus, in alloy system the pristine Fe_3O_4 is completely modified on the surface due to the formation of the AuAg alloy shell layer. Au has a higher atomic number than Ag and so it can be expected that Au based materials will have a higher scattering which is indeed the case (Fig. 6.9 (a)). However, on increasing the content, the linear absorption also increases by formula, $-\ln(I_s/I_0)t$, where I_s is the maximum

intensity of the sample, I_0 is the maximum intensity without the sample and t is the thickness of the sample. As the sample was smeared over the scotch tape, any change in I_s can be attributed to the change in the μ value. Thus, the observed decrease in Au-40 and Ag-40 (Fig. 6.9 (b)) in the scattering intensity (I_s) is due to the increase in μ , which signifies the increasing Au and Ag shell thickness in respective materials. Interestingly, in SAXS analyses for the AuAg alloy shell materials such as $\text{Fe}_3\text{O}_4@AuAg-5:15$, $\text{Fe}_3\text{O}_4@AuAg-10:10$ and $\text{Fe}_3\text{O}_4@AuAg-15:5$. As can be seen from Fig. 6.9(c), the scattering intensity of alloys is higher than the control Fe_3O_4 and similar amongst the compositions at lower q values. However, the scattering intensity, especially at higher q values, gently decreases with increasing Au content in the alloy. These results ascertain the continuous metal shell formation over the Fe_3O_4 core.

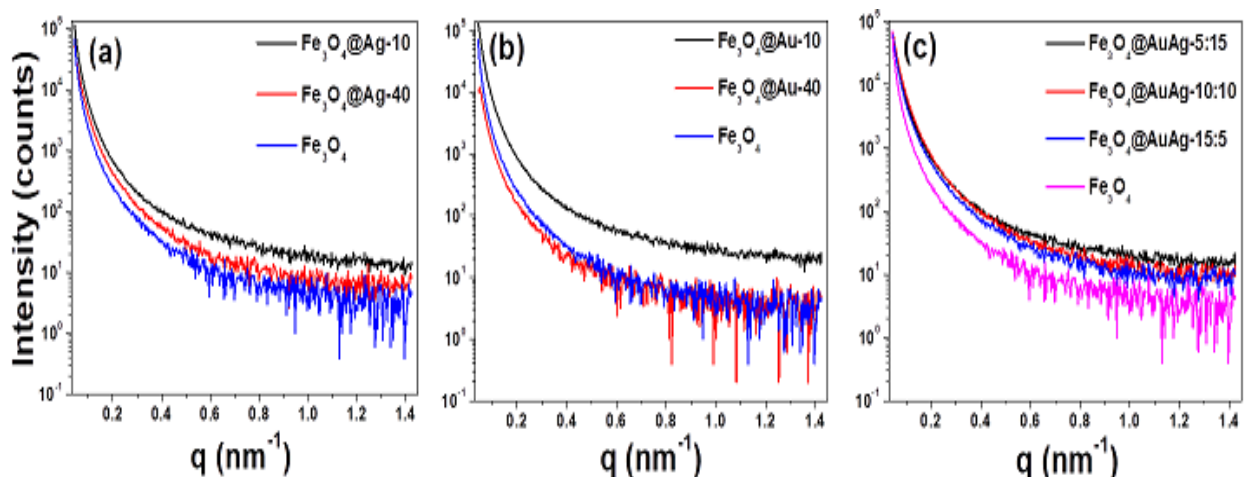


Figure 6.9. Small angle X-ray scattering (SAXS) $\text{Fe}_3\text{O}_4@X-10$, $\text{Fe}_3\text{O}_4@X-40$, $\text{Fe}_3\text{O}_4@AuAg-20$ (for different composition).

6.4 Conclusion

We have shown a solid-state synthetic approach to fabricate $\text{Fe}_3\text{O}_4@AuAg$ alloy core-shell nanostructures leading to gram scale synthesis in the laboratory conditions. Extensive characterizations using XRD, XPS, ED-XRF, FE-SEM, and HR-TEM analyses have confirmed the successful synthesis of $\text{Fe}_3\text{O}_4@M$ core-shell nanostructures. A qualitative SAXS intensity analyses have revealed the pattern is sensitive to the surface alloy composition especially at higher “ q ” which enable to confirm continuous metal shell formation with an average thickness over large area of the sample.

6.5 References

1. Wei, L.-Y.; Huang, K.-S.; Lin, H.-H.; Wu, Y.-P.; Tan, K.-T.; Lee, Y. Y.; Chen, I.-C., Kinetic mechanism of metal enhanced fluorescence by gold nanoparticle with avidin–biotin as spacer and by gold–silver core–shell nanoparticle using fluorescence lifetime image microscopy. *The Journal of Physical Chemistry C* **2018**,*122* (49), 28431-28438.
2. Arenal, R.; Henrard, L.; Roiban, L.; Ersen, O.; Burgin, J.; Treguer-Delapierre, M., Local plasmonic studies on individual core–shell gold–silver and pure gold nano-bipyramids. *The Journal of Physical Chemistry C* **2014**,*118* (44), 25643-25650.
3. Bastús, N. G.; Merkoçi, F.; Piella, J.; Puntès, V., Synthesis of highly monodisperse citrate-stabilized silver nanoparticles of up to 200 nm: kinetic control and catalytic properties. *Chemistry of Materials* **2014**,*26* (9), 2836-2846.
4. Fraire, J. C.; Stremersch, S.; Bouckaert, D.; Monteyne, T.; De Beer, T.; Wuytens, P.; De Rycke, R.; Skirtach, A. G.; Raemdonck, K.; De Smedt, S., Improved label-free identification of individual exosome-like vesicles with Au@ Ag nanoparticles as SERS substrate. *ACS applied materials & interfaces* **2019**,*11* (43), 39424-39435.
5. Farrokhpour, H.; Ghandehari, M., Theoretical Spectroscopic Study on the Au, Ag, Au/Ag, and Ag/Au Nanosurfaces and Their Cytosine/Nanosurface Complexes: UV, IR, and Charge-Transfer SERS Spectra. *The Journal of Physical Chemistry C* **2019**,*123* (26), 16345-16358.
6. Xing, L.; Xiahou, Y.; Zhang, P.; Du, W.; Xia, H., Size control synthesis of monodisperse, quasi-spherical silver nanoparticles to realize surface-enhanced Raman scattering uniformity and reproducibility. *ACS applied materials & interfaces* **2019**,*11* (19), 17637-17646.
7. Bhattacharjee, G.; Bhattacharya, M.; Roy, A.; Senapati, D.; Satpati, B., Core–Shell Gold@ Silver Nanorods of Varying Length for High Surface-Enhanced Raman Scattering Enhancement. *ACS Applied Nano Materials* **2018**,*1* (10), 5589-5600.
8. Moram, S. S. B.; Byram, C.; Shibu, S. N.; Chilukamarri, B. M.; Soma, V. R., Ag/Au nanoparticle-loaded paper-based versatile surface-enhanced Raman spectroscopy substrates for multiple explosives detection. *ACS omega* **2018**,*3* (7), 8190-8201.
9. Bregnhøj, M.; Rodal-Cedeira, S.; Pastoriza-Santos, I.; Ogilby, P. R., Light Scattering versus Plasmon Effects: Optical Transitions in Molecular Oxygen near a Metal Nanoparticle. *The Journal of Physical Chemistry C* **2018**,*122* (27), 15625-15634.

Chapter7

Catalytic catalytic applicability of the core-shell nanostructures $\text{Fe}_3\text{O}_4@M$ (where $M = \text{Au}, \text{Ag}$ and AuAg alloy)

This chapter deals with the catalytic activity of core-shell nanostructures synthesized by solid-state approach. The catalytic activity was tested for H₂ generation from ammonia borane and sodium borohydride with emphasis of role of Ag in alloys systems and magnetic recoverability.

7.1 Results and Discussion

7.1.1 Catalytic studies

The catalytic applicability of the core-shell nanostructures obtained through the solid-state synthetic approach has been studied by choosing catalytic hydrogen generation as a model reaction. Ammonia borane (AB) was chosen as the hydrogen source, as it possesses attractive properties like low molecular weight, easily transportable solid, safe and high gravimetric hydrogen storage.¹⁻³ The catalytic activity experiments were conducted in water. The catalytic activity of Fe₃O₄@Au-20 and Fe₃O₄@Ag-20 catalysts was found to be comparable and in both the cases ~16 mL of hydrogen was generated by ~1150 s (see Fig 7.1(a)).

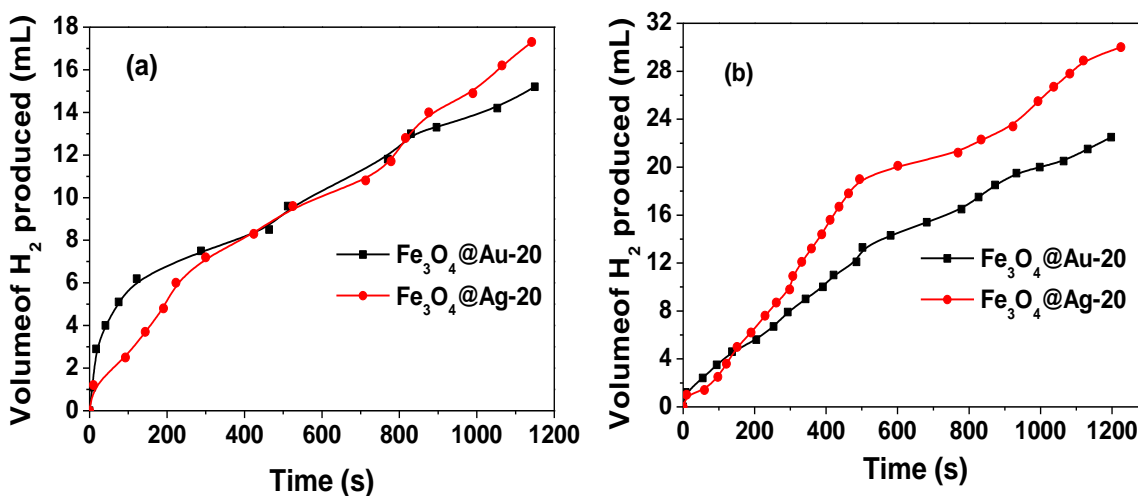


Figure 7.1.Hydrogen generation studies with Fe₃O₄@Au-20 and Fe₃O₄@Ag-20 from a 20 mL of a solution containing (a) 50 mM of AB and (b) 25 mM of NaBH₄ as the hydrogen sources.

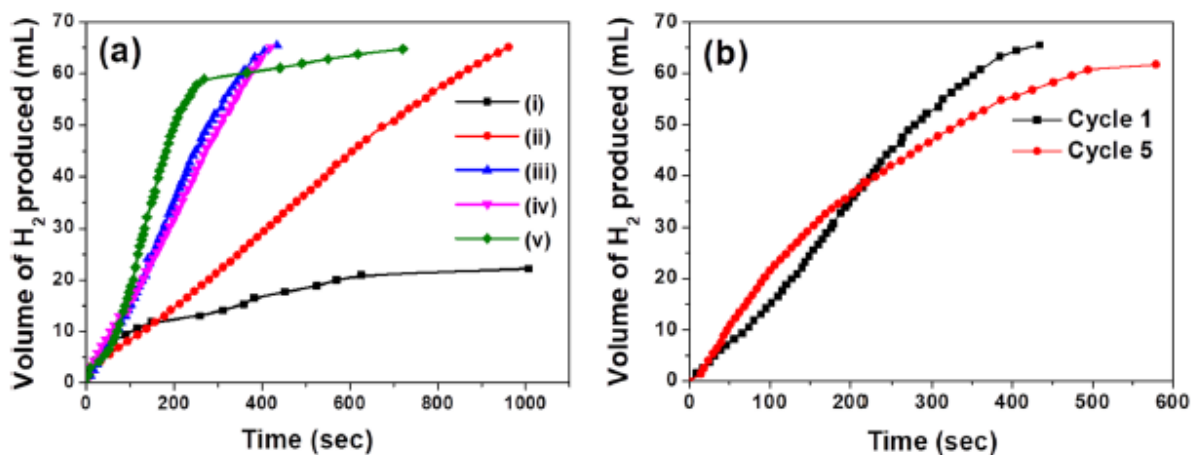


Figure 7.2. (a) Hydrogen generation studies for different catalysts using a mixture of AB and NaBH₄ as the hydrogen sources: (i) Fe₃O₄@Au-20, (ii) Fe₃O₄@AuAg-15:5, (iii) Fe₃O₄@AuAg-10:10, (iv) Fe₃O₄@AuAg-5:15 and (v) Fe₃O₄@Ag-20. (b) Recyclability studies under same conditions using Fe₃O₄@AuAg-10:10. In all cases, [AB] = 50 mM; [NaBH₄] = 25 mM; Total volume of the solution = 20 mL, Catalyst loading = 50 mg.

Hydrogen was also generated using NaBH₄ as the hydrogen source since it is also considered to be one of the potential hydrogen storage compounds.^{4,5} Despite taking half equivalent of NaBH₄, the total hydrogen generated was higher than the case of only AB. The volume of hydrogen generated was ~30 mL with Fe₃O₄@Ag-20 and ~22 mL with Fe₃O₄@Au-20 by ~1200 s (see fig 7.1(b)). Interestingly, when AB and NaBH₄ are mixed together in 2:1 molar ratio, the Fe₃O₄@Ag-20 was found to be highly active that rapidly produced 60 mL of hydrogen by 270 s. After this time, another 5 mL of hydrogen was slowly produced in an additional 450 s (Fig. 7.2 (a)). With Fe₃O₄@AuAg-15:5 alloy, the hydrogen produced was 65 mL by 960 s, which was better than the pure Au catalyst. When the Ag content was increased as in Fe₃O₄@AuAg-10:10 and Fe₃O₄@AuAg-5:15, the rate of hydrogen generation was found to be high and comparable to that of pure Ag catalyst. With both of these catalysts, ~66 mL of hydrogen (close to 100% of theoretical estimate) was generated by ~430 s. Interestingly, the rate of hydrogen generation with all the alloy catalysts remained almost constant throughout the reaction, which was not the case

with pure Ag catalyst that slowed down towards the end of the reaction. The $\text{Fe}_3\text{O}_4@AuAg$ -10:10 catalyst was studied for its kinetics, thermodynamics and magnetic recyclability.

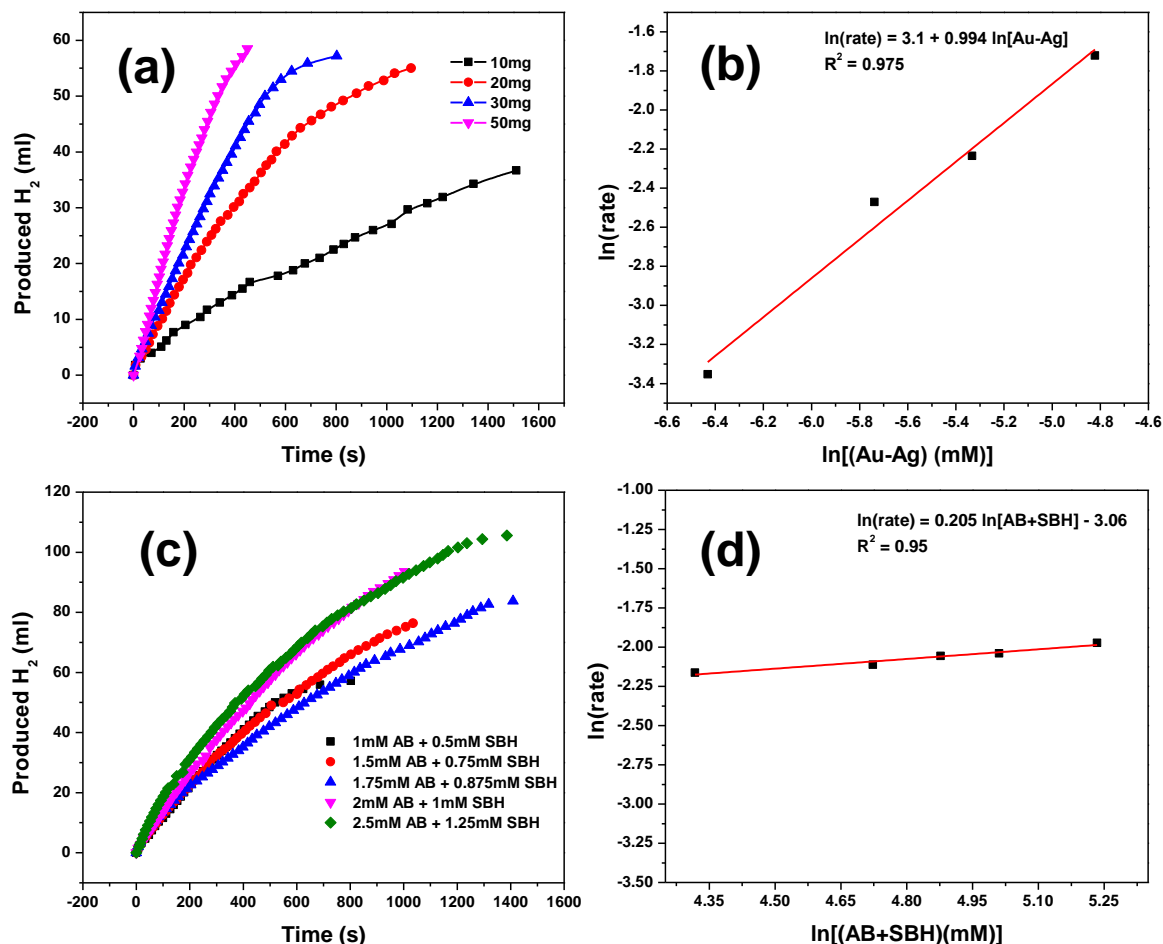


Figure 7.3. Kinetic studies with respect to (a, b) catalyst loading and (c, d) AB + NaBH_4 mixture.

Kinetics experiments were performed in order to determine the order with respect to the concentration of catalyst and the hydrogen source mixture. The reaction was found to follow first order kinetics (slope of 0.994) with the catalyst loading in the range of 10 to 50 mg (see fig 7.3 (a) and (b)) and the reaction was found to follow zero order kinetics (slope of 0.2) with respect to AB/ NaBH_4 mixture (see fig 7.3 (c and d)).⁶⁻⁸ Similar values for order were obtained for SiO_2 based catalysts as well, which indicates that the reaction pathway is identical irrespective of the core component (see fig 7.4 (c,d)). The thermodynamic studies revealed the activation energy to be 42.4 kJ/mol (see fig 7.5 (a and b)).

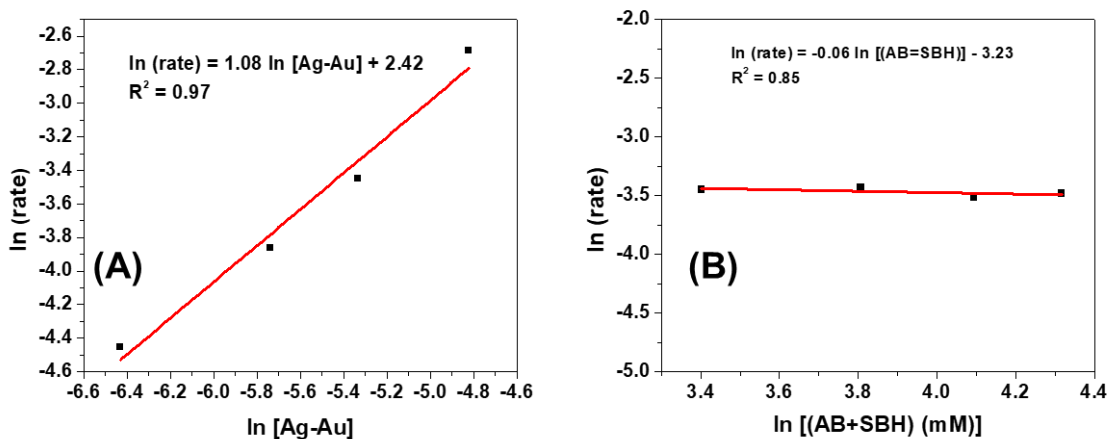
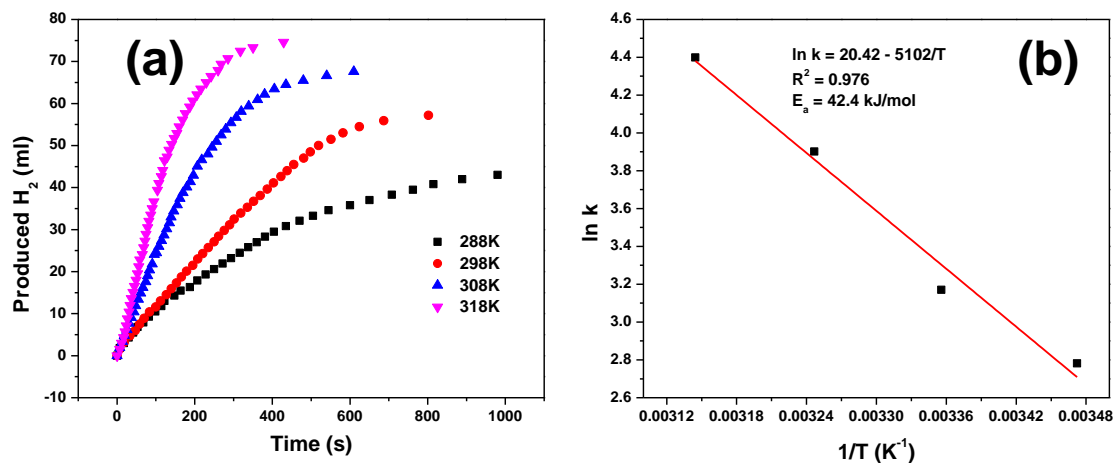


Figure 7.4. Kinetic studies with respect to (A) catalyst loading and (B) AB + NaBH₄ mixture



using Fe₃O₄@AgAu-10:10.

Figure 7.5. Temperature-dependent hydrogen generation studies (a) to estimate the energy of activation from Arrhenius plot (b).

The kinetic and thermodynamic parameters have been found to be similar to the works reported in the literature.⁶⁻⁸ Control experiments were performed, wherein pristine Fe₃O₄, SiO₂, and no-catalyst were employed for the hydrogen generation (see Fig. 7.6). Our results indicate that ~9-12 mL of hydrogen was generated in 600 s in all the three scenarios employed for the

reaction. The higher catalytic activity of the core-shell materials indicates the role of the shell layer composition in the hydrogen generation.

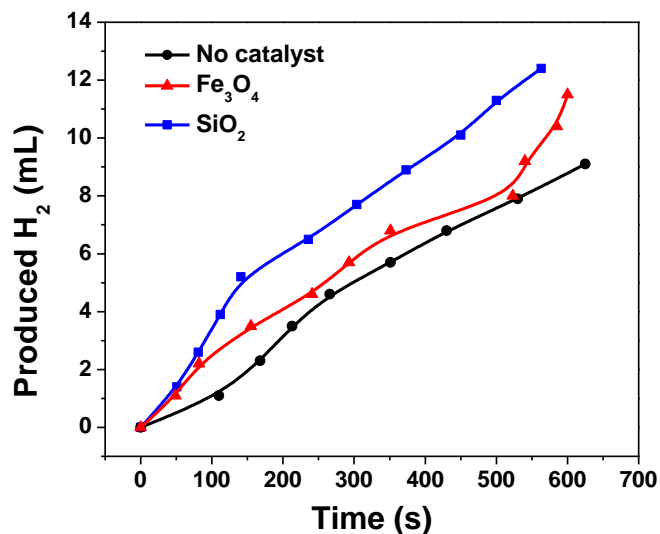


Figure 7.6. Control experiments for hydrogen generation from AB and SBH mixture using pristine Fe₃O₄, SiO₂, and no-catalyst conditions.

The Fe₃O₄@AuAg-10:10 catalyst retained similar activity over the successive cycles and the activity was found to remain very similar even after five cycles (Fig. 7.2(b)). The recycled Fe₃O₄@AuAg-10:10 catalysts were characterized using FE-SEM, HR-TEM and ED-XRF (see S Fig. 7.7). FE-SEM and HR-TEM revealed that the overall morphology of the core-shell nanostructures remained intact. However, along with the core-shell nanoparticles, some additional mass feature was noticed that could be attributed to the polyborazylene byproduct that might have come along with the catalysts (see Fig. 7.8). It is pertinent to mention that the composition of the recovered catalyst by ED-XRF indicates leaching of Ag to the tune of 35.8%, while a minimal leaching of Au to the extent of 8.7% (see Fig. 7.8 (d)). The unexpectedly high leaching of Ag could be attributed to the possible formation of silver-amine borane complex. Although there have been instances in the literature on the combined use of both AB and NaBH₄, the exact role of NaBH₄ in altering the reaction rate is not clearly established.⁹⁻¹³ It is reported that the release of hydrogen from AB is activated by the presence of bases and borohydrides.^{14, 15}

Hence, in the similar line, our results can be attributed to a synergistic mechanism operating between the two hydrogen sources.

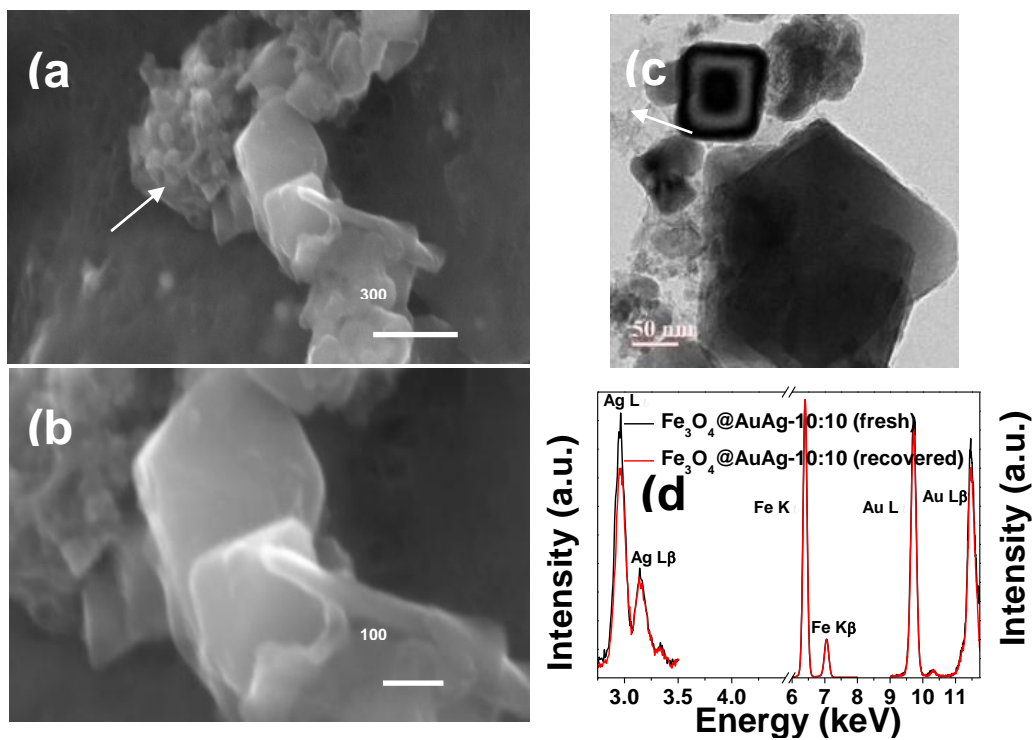
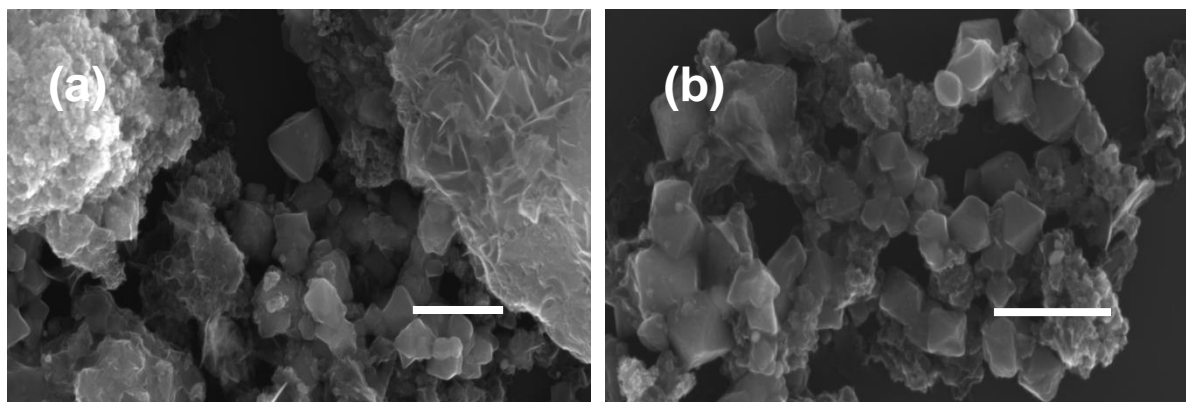


Figure 7.7. FE-SEM (a, b), HR-TEM (c) and ED-XRF (d) analyses on recycled $\text{Fe}_3\text{O}_4@AuAg-10:10$



10:10 alloy catalyst. The arrows indicate the polyborazylene regions.

Figure 7.8. Low magnification FE-SEM images of Fe₃O₄@AuAg-10:10 alloy catalyst after 5 cycles. Scale bar = 500 nm.

7.1.2 Magnetic studies

Since the saturation magnetization (M_s) is an indicator of magnetic recoverability of a catalyst, we performed room temperature vibrating sample magnetometer (VSM) measurements for selected samples and the results are plotted in Fig 7.9. The saturation magnetization (M_s) value of the pristine Fe₃O₄ sample was reported to be ~174 emu/g.¹⁶ The M_s values obtained for Fe₃O₄@Au-10, Fe₃O₄@AuAg-10:10, Fe₃O₄@Ag-10 were 68.5, 82.1 and 98.1 emu/g, respectively. In comparison to the pristine Fe₃O₄, the decrease in M_s value of Fe₃O₄ with the incorporation of Au or Ag can be attributed to the shielding effect of diamagnetic noble metal/alloy shell layer coated over the Fe₃O₄ core. The obtained M_s values indicate that these materials retain sufficient magnetization, which is crucial for the excellent magnetic recoverability and reusability of the catalysts.

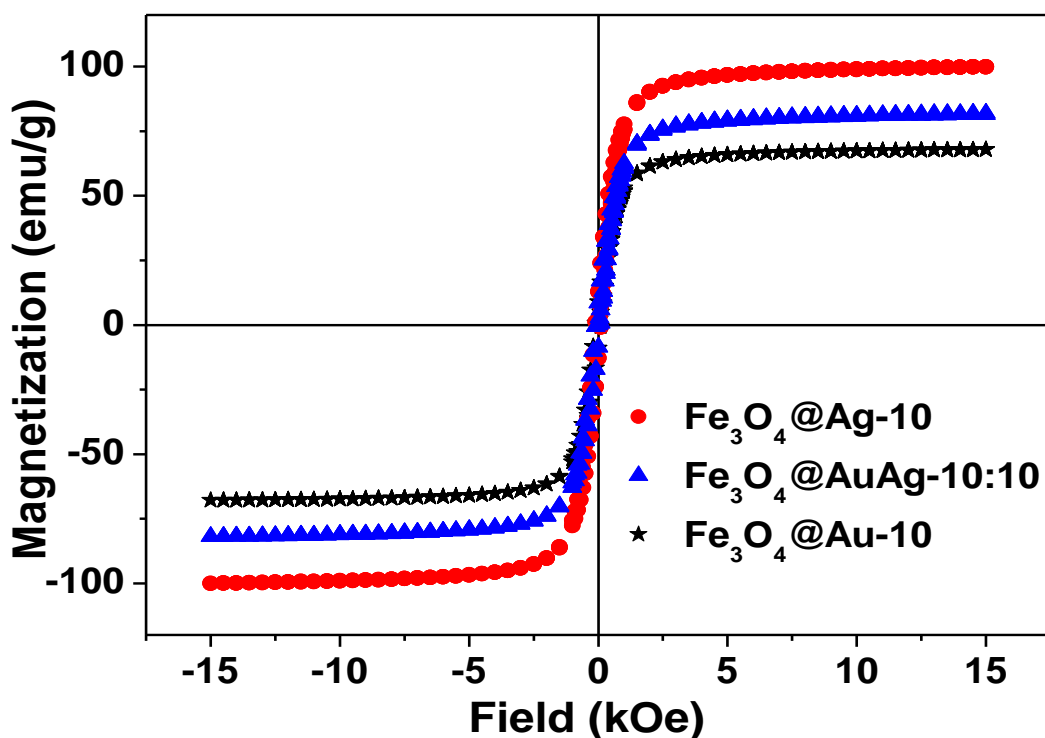


Figure 7.9. Magnetization as a function of external applied magnetic field for three samples as indicated in the figure.

7.2 Conclusions

The $\text{Fe}_3\text{O}_4@\text{Ag}$ and Ag-rich alloy catalysts synthesized in this study have shown high catalytic efficacy for hydrogen generation than $\text{Fe}_3\text{O}_4@\text{Au}$ and Au-rich alloy. Such a high catalytic efficacy has been found to be profound when a mixture of AB and NaBH_4 is used rather than employing the hydrogen sources individually. The magnetic recoverability and recyclability studies on $\text{Fe}_3\text{O}_4@\text{AuAg-10:10}$ catalyst has demonstrated the efficient reusability of the catalysts even after 5 cycles. In general, a solvent-less simple physical grinding of a metal precursor over an oxide core followed by thermolysis is presented as a potential strategy for facile, robust, and cost-effective large scale synthesis of MO@M systems. In addition, the prime merit of this approach is to maintain the metal content in the resulting MO@M systems as per the feed ratio. We believe that this approach will be a paradigm shift for further synthetic explorations on different shell materials such as oxides, sulfides, nitrides, and non-noble metals *via* reduction of an initially formed oxide shell.

7.3 References

1. Stephens, F. H.; Pons, V.; Baker, R. T., Ammonia–borane: the hydrogen source par excellence? *Dalton Transactions* **2007**, (25), 2613-2626.
2. Heldebrant, D. J.; Karkamkar, A.; Linehan, J. C.; Autrey, T., Synthesis of ammonia borane for hydrogen storage applications. *Energy & Environmental Science* **2008**,1 (1), 156-160.
3. Yao, Q.; Lu, Z.-H.; Zhang, Z.; Chen, X.; Lan, Y., One-pot synthesis of core-shell Cu@SiO₂ nanospheres and their catalysis for hydrolytic dehydrogenation of ammonia borane and hydrazine borane. *Scientific reports* **2014**,4, 7597.
4. Liu, B.; Li, Z., A review: hydrogen generation from borohydride hydrolysis reaction. *Journal of Power Sources* **2009**,187 (2), 527-534.
5. Demirci, U. B.; Akdim, O.; Andrieux, J.; Hannauer, J.; Chamoun, R.; Miele, P., Sodium borohydride hydrolysis as hydrogen generator: issues, state of the art and applicability upstream from a fuel cell. *Fuel Cells* **2010**,10 (3), 335-350.
6. Sun, D.; Mazumder, V.; Metin, O.; Sun, S., Catalytic hydrolysis of ammonia borane via cobalt palladium nanoparticles. *ACS nano* **2011**,5 (8), 6458-6464.
7. Metin, O.; Ozkar, S., Hydrogen generation from the hydrolysis of ammonia-borane and sodium borohydride using water-soluble polymer-stabilized cobalt (0) nanoclusters catalyst. *Energy & Fuels* **2009**,23 (7), 3517-3526.
8. Vernekar, A. A.; Bugde, S. T.; Tilve, S., Sustainable hydrogen production by catalytic hydrolysis of alkaline sodium borohydride solution using recyclable Co–Co₂B and Ni–Ni₃B nanocomposites. *international journal of hydrogen energy* **2012**,37 (1), 327-334.
9. Hannauer, J.; Demirci, U.; Geantet, C.; Herrmann, J.; Miele, P., Enhanced hydrogen release by catalyzed hydrolysis of sodium borohydride–ammonia borane mixtures: a solution-state ¹¹B NMR study. *Physical Chemistry Chemical Physics* **2011**,13 (9), 3809-3818.
10. Yan, J. M.; Zhang, X. B.; Han, S.; Shioyama, H.; Xu, Q., Iron- nanoparticle- catalyzed hydrolytic dehydrogenation of ammonia borane for chemical hydrogen storage. *Angewandte Chemie* **2008**,120 (12), 2319-2321.
11. Simagina, V.; Komova, O.; Ozerova, A.; Netskina, O.; Odegova, G.; Kellerman, D.; Bulavchenko, O.; Ishchenko, A., Cobalt oxide catalyst for hydrolysis of sodium borohydride and ammonia borane. *Applied Catalysis A: General* **2011**,394 (1-2), 86-92.

12. Umegaki, T.; Yan, J.-M.; Zhang, X.-B.; Shioyama, H.; Kuriyama, N.; Xu, Q., Hollow Ni–SiO₂ nanosphere-catalyzed hydrolytic dehydrogenation of ammonia borane for chemical hydrogen storage. *Journal of Power Sources* **2009**,*191* (2), 209-216.
13. Umegaki, T.; Takei, C.; Xu, Q.; Kojima, Y., Fabrication of hollow metal oxide–nickel composite spheres and their catalytic activity for hydrolytic dehydrogenation of ammonia borane. *International journal of hydrogen energy* **2013**,*38* (3), 1397-1404.
14. Himmelberger, D. W.; Yoon, C. W.; Bluhm, M. E.; Carroll, P. J.; Sneddon, L. G., Base-promoted ammonia borane hydrogen-release. *Journal of the American Chemical Society* **2009**,*131* (39), 14101-14110.
15. Ewing, W. C.; Marchione, A.; Himmelberger, D. W.; Carroll, P. J.; Sneddon, L. G., Syntheses and structural characterizations of anionic borane-capped ammonia borane oligomers: evidence for ammonia borane H₂ release via a base-promoted anionic dehydropolymerization mechanism. *Journal of the American Chemical Society* **2011**,*133* (42), 17093-17099.
16. Challagulla, S.; Nagarjuna, R.; Ganesan, R.; Roy, S., Acrylate-based polymerizable sol–gel synthesis of magnetically recoverable TiO₂ supported Fe₃O₄ for Cr (VI) photoreduction in aerobic atmosphere. *ACS Sustainable Chemistry & Engineering* **2016**,*4* (3), 974-982.

Chapter8

Synthesis , Characterization and Catalytic catalytic applicability of $\text{Fe}_3\text{O}_4@Pd$ core-shell nanostructures

8.1 Introduction

This chapter deals with the synthesis of $\text{Fe}_3\text{O}_4@\text{Pd}$ nanostructures. The results obtained for structural, chemical, microstructural, magnetic characterization by using TGA-DTA, XRD, XPS, FE-SEM, BET, HR-TEM, and VSM techniques are discussed. The catalytic activity was tested for 4-nitrophenol reduction by sodium borohydride aqueous solution. Magnetic recoverability have also been demonstrated,

The formation of $\text{Fe}_3\text{O}_4@\text{Pd}$ core-shell nanostructures in near quantitative yields through a solid-state approach that involves a simple physical grinding of a metal precursor over Fe_3O_4 core, followed by calcination. The process involves mixing of palladium precursor over the Fe_3O_4 core, which in turn facilitates a continuous shell layer post thermolysis. Palladium is exciting and excellent as a catalyst towards broad areas of industrial and chemical reactions. It is well-known for heterogeneous catalysis in automobile industries,¹ fuel cells,^{2, 3} energy storage^{4, 5} electrochemical redox reactions,⁶⁻⁸ and many organic C-C coupling reactions.⁹⁻¹¹ Few reports are available on Fe_3O_4 supported palladium (Pd) nanoparticles synthesis and their promising catalytic property towards nitro-group reduction using sodium borohydride as a hydrogen source.¹²⁻¹⁴

Among the various applications, the reduction of nitro to amine functionality is an industrially relevant conversion. Aromatic amines find colossal use in the production of various components like dyestuff, rubber-processing, and drugs.¹⁵ These amines find use in the preparation of polyurethane polymers.¹⁶ The nitro to amine conversions takes place at elevated temperatures such as 200-300 °C. A plethora of studies on nitro-group reduction, especially by sodium borohydride, in the presence of various types of catalysts has been well-documented.¹⁷ The supported catalysts are preferred since such a design allows immobilization of catalytically active species at the surface, and thereby, helps prevent their agglomeration.¹⁸ From a sustainable perspective, magnetic recoverability is an important approach that has garnered an enormous attention.¹⁹ Among the various magnetic supports, magnetite can act as excellent support for nanoparticles as it is easily recoverable and reusable after catalysis experiments.

We hypothesized that addition of non-surfactant based metal-based precursor over an oxide core followed by decomposition resulting in metallization and a progressively increasing

the metal precursor content would result in a continuous metal shell formation. Therefore, palladium acetate (Pd-ac) have been chosen as a source of Pd.

8.2 Experimental details

8.2.1 Materials. Commercial Fe_3O_4 obtained from Aldrich was chosen to be the core particles. The commercial Fe_3O_4 had a regular octahedron. The particle dimension was approximately around 250 nm in both core materials. Palladium acetate, $\text{Pd}(\text{OAc})_2$ was also purchased from Aldrich.

8.2.2 Core-shell synthesis. In a typical core-shell synthesis using our solid-state approach, a calculated amount of the metal precursor, Pd-Ac was mixed with the magnetite core followed by thorough grinding for 10 min in order to achieve a uniform coating of the precursor over the Fe_3O_4 core. The obtained mixture was transferred to an autoclave and subjected to calcination at different temperatures for 2 h. An autoclave was used in order to avoid any surface oxidation during metallization. The core-precursor assembly after the calcination step was allowed to cool naturally inside the furnace, thus ensuring a slow cooling, unless otherwise mentioned. The resultant products have been labeled as $\text{Fe}_3\text{O}_4@\text{M-X}$, where M and X represent the metal and the weight percent of its corresponding precursor with respect to the initial Fe_3O_4 content, respectively. For instance, 100 mg of Fe_3O_4 was mixed with 10 mg of $\text{Pd}(\text{OAc})_2$ and decomposed, it results in sample $\text{Fe}_3\text{O}_4@\text{Pd-10}$. The nanostructures were characterized and tested for catalytic activity without any further purification.

8.2.3 Catalysis: In catalytic 4-nitrophenol reduction experiment, 5 mg of the catalyst was added to 10 mL of a solution containing the mixture of 4-nitrophenol (0.143 mM) and NaBH_4 (14.3 mM).

The reduction reaction was performed under pseudo-first order conditions that concentration of NaBH_4 was maintained 100 times more than the concentration of 4-nitrophenol, The reaction was monitored by UV-vis spectrometer by monitoring absorbance of 400 nm peak due to 4-nitrophenolate species.

8.3 Results and Discussion

8.3.1 TGA-DTA studies

The thermal stability of the precursors has been studied using thermogravimetric analysis. The thermal decomposition and the corresponding derivative plot of the precursors are given in the Fig. 8.1. The onset of the thermal decomposition in these precursors was found to be close to 200 °C and the major mass loss was found to occur between 210 and 230 °C. Based on the derivative plot, the lowest calcination temperature in this study had been fixed at 250 °C. The calculated and experimental residual mass of the metals in the corresponding precursors is given in Table 8.1.

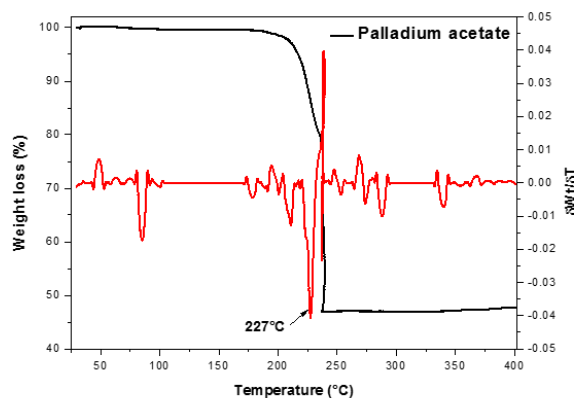


Figure 8.1. Thermogravimetric and differential thermal analyses of the metal precursors used in this study. Black and red represent thermogravimetry and differential thermogravimetry, curves, respectively.

Table 8.1. Calculated and experimental metal content (wt.%) in the Pd precursor used in this study.

Sample Code	Calculated	Experimental
Pd-ac	48	45

8.3.2 XRD studies

In case of $\text{Fe}_3\text{O}_4@\text{Pd}$, the XRD (Fig. 8.2 e-h) patterns revealed a strikingly contrast observation that the Pd (111) peak decreased with increasing loading of the Pd-Ac precursor. In 20% loading of the precursor, the Pd (111) peak intensity became negligible, which completely disappeared with further increment in the precursor loading. This is contradictory to that observed in $\text{Fe}_3\text{O}_4@\text{Au}$ and $\text{Fe}_3\text{O}_4@\text{Ag}$ reported in chapter 4 and 5. Interestingly, at the same time, with 30% loading of the Pd-Ac precursor, the formation of $\alpha\text{-Fe}_2\text{O}_3$ phase was observed, whose relative amount increased at the expense of magnetite with further loading.

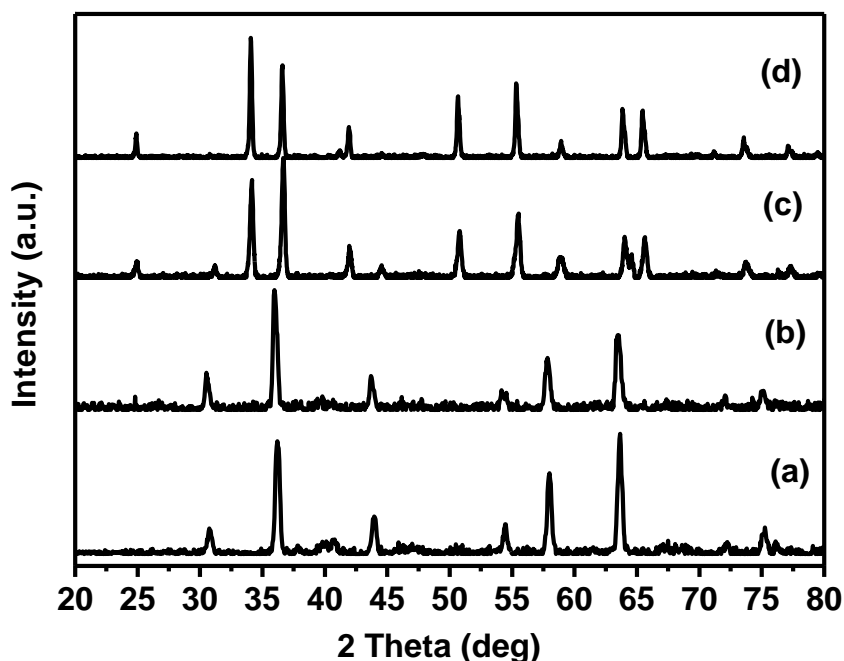
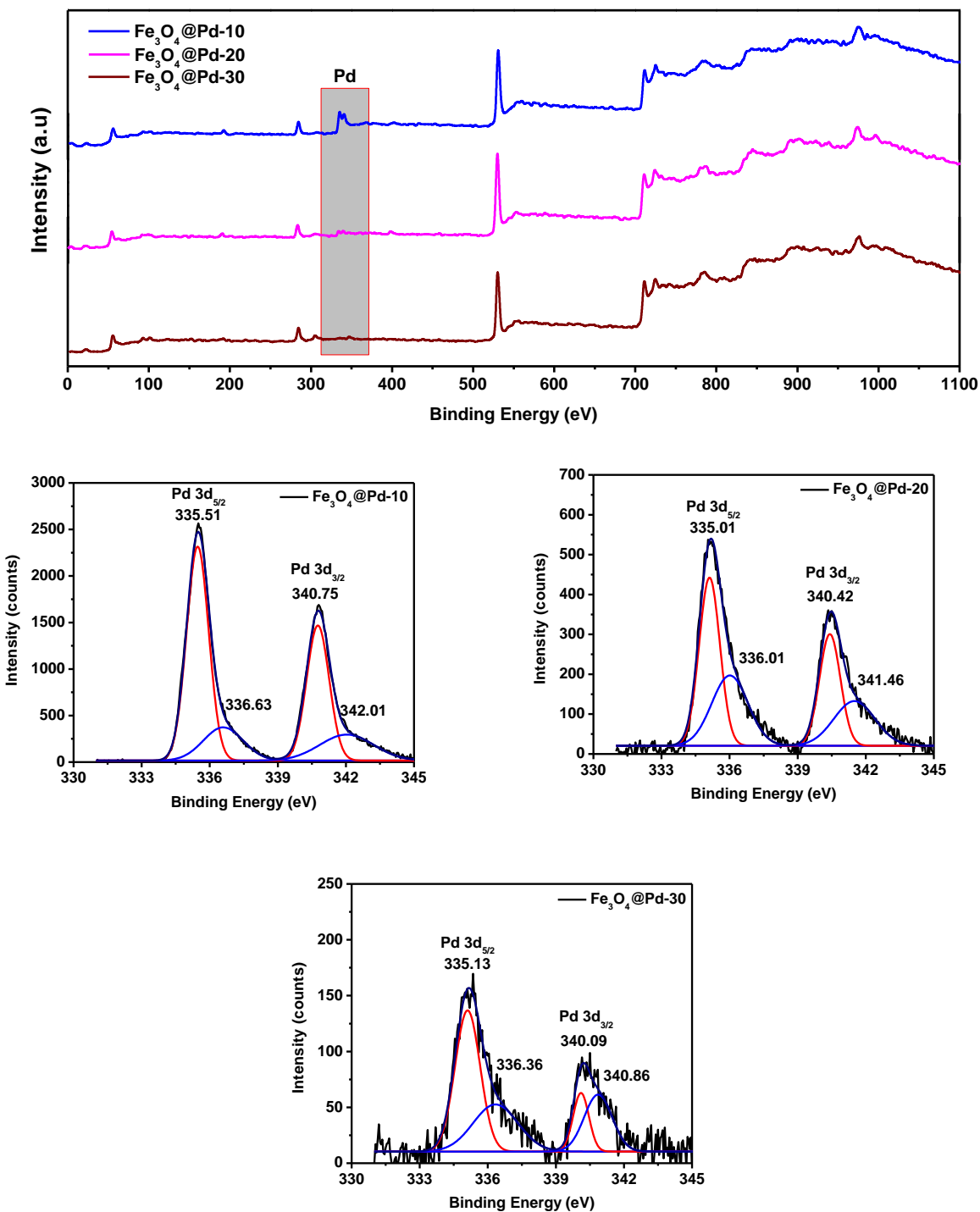


Figure 8.2 XRD patterns of $\text{Fe}_3\text{O}_4@\text{Pd-X}$ obtained after calcination at 250 °C for 2 h. (e) 10 mg, (f) 20 mg, (g) 30 mg and (h) 50 mg of precursor.

We speculate that this observation can be attributed to the interaction between metal and the support. After the discovery of the strong metal-support interaction (SMSI) concept by Tauster *et al.*²⁰ in 1978, further studies revealed that in several systems wherein a noble metal is supported onto an oxide, the support species migrate onto the metal particles and encapsulate them in an oxide matrix.^{21, 22} This effect was initiated and facilitated by the metal-metal bonding between the noble metal and the metal ion present in the support.²³ In our study, the observed

trend in surface oxidation of Fe_3O_4 to $\alpha\text{-Fe}_2\text{O}_3$ with higher loading of Pd-Ac further substantiates the occurrence of metal-support interaction in this system.



8.3.3 XPS studies

Figure 8.3 (a) XPS profile of $\text{Fe}_3\text{O}_4@\text{Pd-X}$ ($X=10,20,30$) and Pd 3d narrow scan spectra for 10, 20 and 30 respectively.

$\text{Fe}_3\text{O}_4@\text{Pd-10}$ was studied for its 3d core level XPS spectrum, which revealed the Pd $3d_{5/2}$ and Pd $3d_{3/2}$ peak values to be 335.4 and 340.7 eV, respectively. The characteristic Pd 3d peak values and their separation of 5.3 eV confirmed the presence of zero valent palladium.²⁴ However, the non-Gaussian profile of these peaks at the tail end warranted their deconvolution that suggests the presence of a small amount of palladium in its +2 oxidation state. On increasing Pd content the fraction of Pd^{2+} was found to increase (Fig. 8.3). On heat treatment at 900 °C for 2 h, the increase in the intensity of XPS peak corresponding to Pd^{2+} is obvious (Fig. 8.4).

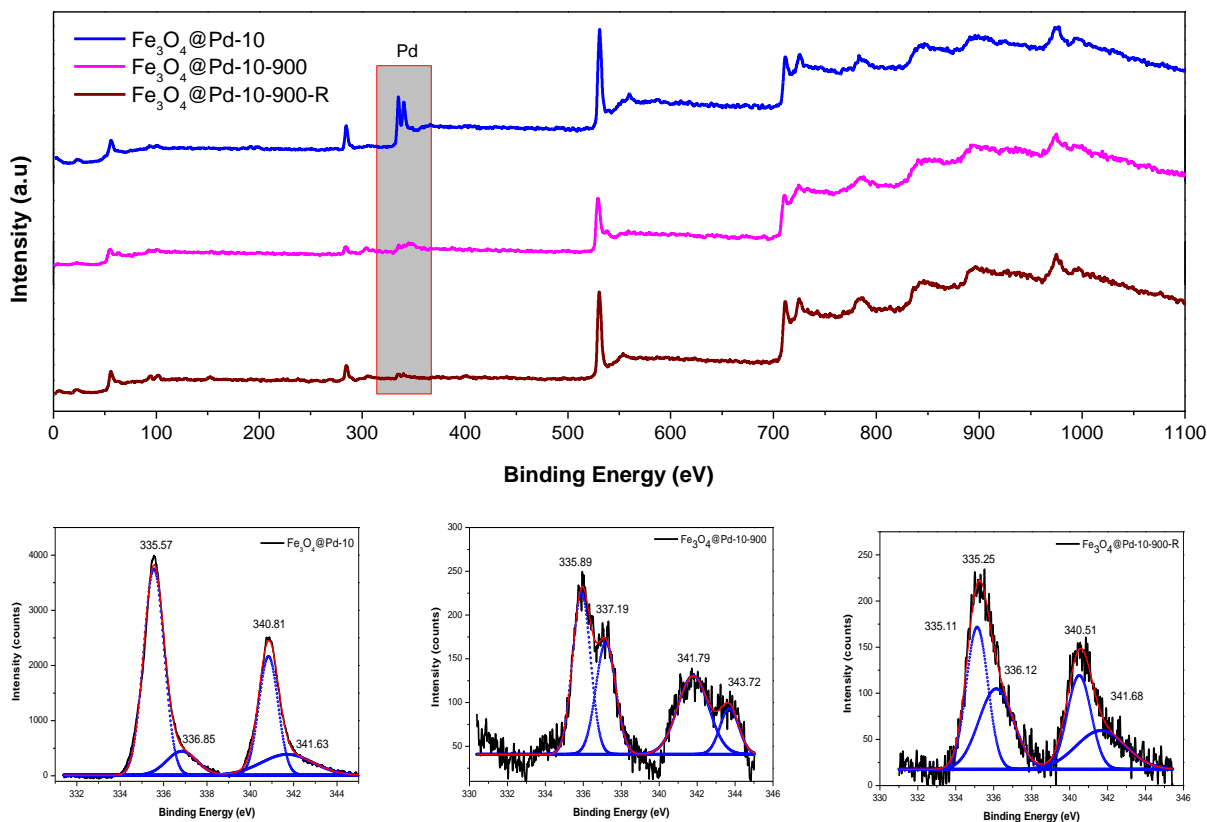


Figure 8.4 (a) XPS profile of $\text{Fe}_3\text{O}_4@\text{Pd-10}$, $\text{Fe}_3\text{O}_4@\text{Pd-10}$ heat treated at 900 °C and the duplicate spectra of the heat treated sample.

8.3.4 FE-SEM studies

We further continued to explore the unique SMSI behavior of palladium, which is markedly different as opposed to gold and silver. The surface morphology of $\text{Fe}_3\text{O}_4@\text{Pd}$ samples with increasing Pd-Ac precursor loading have been explored using FE-SEM analyses and are presented in Fig. 8.5. As can be observed, the $\text{Fe}_3\text{O}_4@\text{Pd}$ -20 was found to possess nanoislands having size in the range of ~ 10 nm. When the weight percent of Pd-Ac was progressively increased, the size of the nanoislands was not increased proportionally, however, the number density of the nanoislands was found to be increasing. This phenomenon was prominent till the Pd-Ac loading was as high as 70 % (Fig. 8.5 (A-E)), above which a considerable amount of coalescence between the nanoislands has been observed. With 80% of the precursor loading (Fig. 8.5 F), complete shell formation was also visible in several places. This strongly validates the SMSI in this system, thereby corroborating the surface oxidation of Fe_3O_4 to $\alpha\text{-Fe}_2\text{O}_3$ with increasing Pd content, as observed with XRD. Thus, in our system, we believe that the surface of Fe_3O_4 gets oxidized during the calcination step to form $\alpha\text{-Fe}_2\text{O}_3$ that encapsulates the Pd nanoparticles, which in turn prevents conjoining of Pd nanoislands to form a continuous shell layer. To study the effect of calcination on the nanoisland structures, the $\text{Fe}_3\text{O}_4@\text{Pd}$ -10 was heat-treated at 500 and 900 °C in air. At 500 °C, the Pd particles were found to be grown in size (Fig. 8.5 G), possibly in the process of lateral spreading. At 900 °C, there were no nanoisland type structures, but flat conjoined magnetite core nanoparticles through possible Pd/ $\alpha\text{-Fe}_2\text{O}_3$ shell was evident (Fig. 8.5 H).

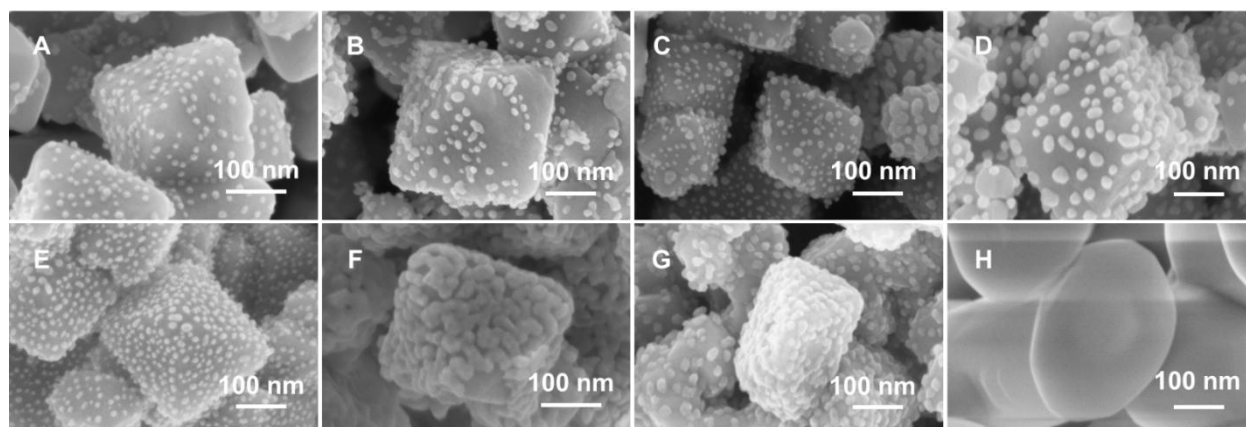


Figure 8.5. High magnification FE-SEM images of $\text{Fe}_3\text{O}_4@\text{Pd}$ -X, where X = normally cooled (A) 20, (B) 30, (C) 50, (D) 60, (E) 70, (F) 80, (G) 10 – heat treated at 500 °C, and (H) 10 – heat treated at 900 °C.

While the metal-mediated aggregation of the core-shell nanostructures with an increase in metal precursor loading was evident in Au and Ag systems, the observations for Pd systems is quite different. For Au and Ag the observations can be interpreted in terms of surface energy, while in Pd the spill-over of iron oxide over Pd play an important role. This is corroborated the observation of XRD results that on increasing Pd content, Fe_2O_3 covering the Pd islands leading to the amorphous like observation.

8.3.5 HR-TEM studies

Further evidence for this SMSI state in our system came from the HR-TEM analysis (Figure 8.6). To verify the presence of oxide coating over the Pd nanoislands, we performed the HR-TEM analysis over $\text{Fe}_3\text{O}_4@Pd-10$ calcined at 250 and 900 °C. The $\text{Fe}_3\text{O}_4@Pd-10$ calcined at 250 °C (Figure 8.6 (A-C)) revealed the presence of Pd nanoislands over Fe_3O_4 core. It can also be observed that an ultrathin oxide coating layer (~2-3 nm) was present over the Fe_3O_4 surface and also encapsulating the Pd nanoislands. The lattice fringe widths determined in the islands was 0.23 nm, which confirmed the presence of Pd as nanoislands in crystalline form at this loading. The $\text{Fe}_3\text{O}_4@Pd-10$ calcined at 900 °C appeared as reddish brown in color, indicating the excessive surface oxidation of Fe_3O_4 . The HR-TEM image of $\text{Fe}_3\text{O}_4@Pd-10$ did not show any metal nanoislands (Figure 8.6 (D-F)), but showed the aggregated nanoparticles whose surface was found to possess a thin shell layer, presumably due to the formation of palladium-iron oxide composite that can be represented as $\text{Fe}_3\text{O}_4@Pd/\alpha\text{-Fe}_2\text{O}_3$.

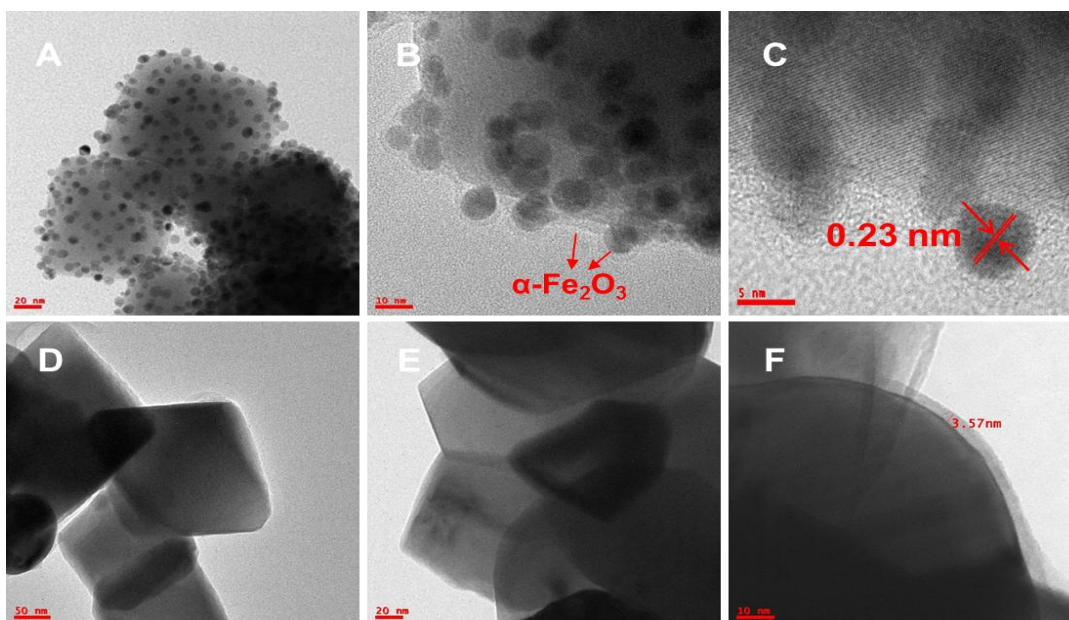


Figure 8.6 HR-TEM images with various magnifications $\text{Fe}_3\text{O}_4@\text{Pd}-10$: (A-C) – heat treated at 250 °C, and (D-F) – heat treated at 900 °C. It is clear that on heat-treatment the nanoislands like structure transforms into a core-shell structure.

8.3.6 BET studies

In case of Pd, the respective surface areas of $\text{Fe}_3\text{O}_4@\text{Pd}-10$ and $\text{Fe}_3\text{O}_4@\text{Pd}-40$ were found to be 17.8 and 14.4 m^2/g . Though the trend in the decrement in surface area with increasing the metal precursor loading is similar to Au and Ag, the absolute values reflect that the surface area values are much higher than the commercial Fe_3O_4 core. This could be attributed to the SMSI state, wherein Pd-nanodomains were formed over the Fe_3O_4 core along with an encapsulated layer of $\alpha\text{-Fe}_2\text{O}_3$. When the $\text{Fe}_3\text{O}_4@\text{Pd}-10$ was calcined at 500 and 900 °C, the surface area values obtained were 13.2 and 4.1 m^2/g , respectively. As observed with FE-SEM, the calcination at 500 °C flattened the nanoislands, but did not result in severe inter-particle aggregation. However, the sample calcined at 900 °C was found to be highly aggregated and therefore resulted in a drastic decrement in the surface area. These results confirm that the structural evolution is different in Pd, when compared to gold and silver.

8.3.7 Magnetic studies:

As the magnetic property would be of interest for several applications, we probed the change in saturation magnetization (M_s) in $\text{Fe}_3\text{O}_4@\text{Pd}-10$ as a function of calcination temperature and the results are plotted in Fig. 8.7. The as-procured commercial Fe_3O_4 possessed a M_s value of ~ 174 emu/g, whereas the $\text{Fe}_3\text{O}_4@\text{Pd}-10$ synthesized at 250 °C possessed M_s value of 161.4 emu/g. Since the Fe_3O_4 to Pd weight ratio in this product is $\sim 95:5$, the M_s value reveals negligible loss in the magnetic property of the Fe_3O_4 core. However, the M_s values of $\text{Fe}_3\text{O}_4@\text{Pd}-10$ calcined at 500 and 900 °C were found to be 28.5 and 0.98 emu/g, respectively. It is obvious that the tremendous decrease in the M_s values can be attributed to the oxidation of Fe_3O_4 to $\alpha\text{-Fe}_2\text{O}_3$. These results suggest that acceptable degree of magnetic properties are retained till a calcination temperature of 500 °C.

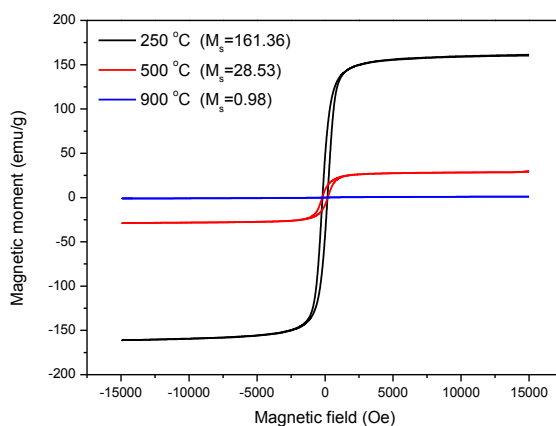


Figure 8.7. Plot of saturation magnetization (emu/g) vs external applied field for Commercial Fe_3O_4 , $\text{Fe}_3\text{O}_4@Pd-10$ – heat treated at 250 °C, $\text{Fe}_3\text{O}_4@Pd-10$ – heat treated at 500 °C, and $\text{Fe}_3\text{O}_4@Pd-10$ – heat treated at 900 °C.

8.3.8 Catalytic studies:

A demonstrative experiment was carried out to check the availability of Pd towards catalysis. The well-known *p*-nitrophenol reduction to *p*-aminophenol in the presence of NaBH_4 was carried out using $\text{Fe}_3\text{O}_4@Pd-10$ (Fig. 8.2.8), and these catalysts demonstrated a decent catalytic activity. The reduction reaction was found to progress well despite the presence of amorphous $\alpha\text{-Fe}_2\text{O}_3$ layer over Pd. Fig. 8.2.9 shows the plot of (C/C_0) vs time for progressive five cycles. The metal-support interaction phenomenon was not found to be universal for all noble metal and oxide combinations, but for selected metals and oxides combinations only. In some cases reported in the literature, the metal-support interaction state has been considered to be beneficial in catalysis. One such example is hydroformylation of ethylene over $\text{Pd}/\text{Nb}_2\text{O}_5$, in which the strong metal-support interaction state (SMSI) is known to catalyze the reaction, but not the non-SMSI state of $\text{Pd}/\text{Nb}_2\text{O}_5$.²⁵ Naumann d'Alnoncourt *et al.* has reported the SMSI state between Pd/FeO_x system and demonstrated it to be beneficial for CO oxidation.²⁶ It is believed that the oxide provides the initial adsorption sites for the reactants, followed by the catalysis over the noble metal surface.

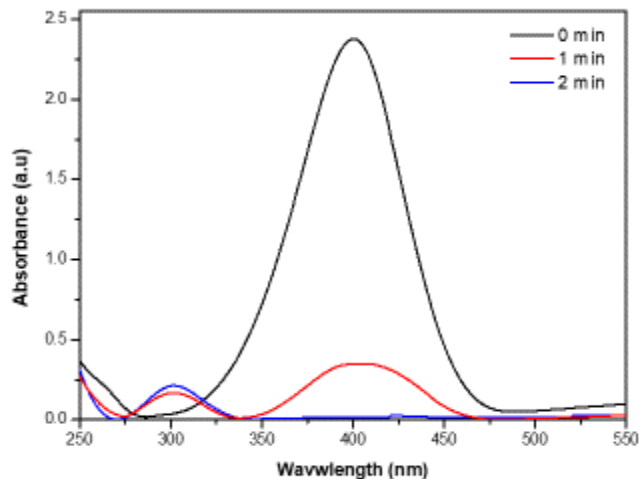


Figure 8.8 Plot of absorbance versus time. The decrease in the absorbance of 400 nm indicate the consumption of 4-nitrophenolate species. The appearance of peak at 300 nm is due to formation of 4-aminophenol product.

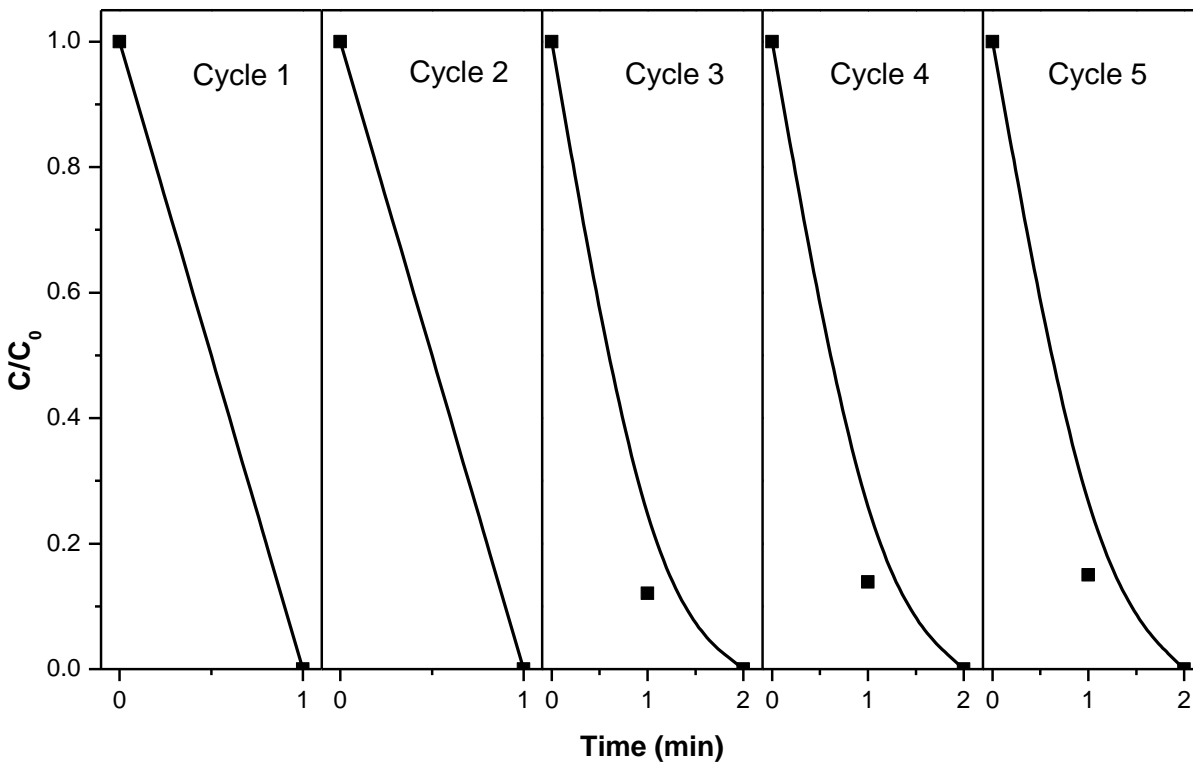


Figure 8.9 Plot of C/C_0 versus time for the five successive cycles.

8.4 Conclusions

We have shown a solid-state synthetic approach to fabricate Fe₃O₄@Pd core-shell nanostructures leading to gram scale synthesis in the laboratory conditions. Extensive characterizations using XRD, XPS, FE-SEM, and HR-TEM analyses have confirmed the successful synthesis of Fe₃O₄@Pd core-shell nanostructures. Furthermore, on increasing Pd content the Pd nanoislands do not coalesce to form a shell but the number density of Pd islands increased. On loading even 1:1 weight ratio of Fe₃O₄ to Pd. Besides, on increasing Pd amount, the formation of α -Fe₂O₃ was observed which was attributed to the interaction of strong metal (Pd) support (Fe₃O₄) interaction. Only on heating to 900 °C, the Pd nanoislands were found to coalesce on the surface. The Pd catalyst exhibited catalytic activity towards 4-nitrophenol reduction. We believe that this approach will be a paradigm shift for further synthetic explorations on different shell materials such as oxides, sulfides, nitrides, and non-noble metals *via* reduction of an initially formed oxide shell.

8.5 References

1. Freund, H. J.; Meijer, G.; Scheffler, M.; Schlögl, R.; Wolf, M., CO oxidation as a prototypical reaction for heterogeneous processes. *Angewandte Chemie International Edition* **2011**,*50* (43), 10064-10094.
2. Bianchini, C.; Shen, P. K., Palladium-based electrocatalysts for alcohol oxidation in half cells and in direct alcohol fuel cells. *Chemical reviews* **2009**,*109* (9), 4183-4206.
3. Mazumder, V.; Sun, S., Oleyamine-mediated synthesis of Pd nanoparticles for catalytic formic acid oxidation. *Journal of the American Chemical Society* **2009**,*131* (13), 4588-4589.
4. Yamauchi, M.; Ikeda, R.; Kitagawa, H.; Takata, M., Nanosize effects on hydrogen storage in palladium. *The Journal of Physical Chemistry C* **2008**,*112* (9), 3294-3299.
5. Horinouchi, S.; Yamanoi, Y.; Yonezawa, T.; Mouri, T.; Nishihara, H., Hydrogen storage properties of isocyanide-stabilized palladium nanoparticles. *Langmuir* **2006**,*22* (4), 1880-1884.
6. Chen, X.; Wu, G.; Chen, J.; Chen, X.; Xie, Z.; Wang, X., Synthesis of “clean” and well-dispersive Pd nanoparticles with excellent electrocatalytic property on graphene oxide. *Journal of the American Chemical Society* **2011**,*133* (11), 3693-3695.

7. Lee, H.; Habas, S. E.; Somorjai, G. A.; Yang, P., Localized Pd overgrowth on cubic Pt nanocrystals for enhanced electrocatalytic oxidation of formic acid. *Journal of the American Chemical Society* **2008**, *130* (16), 5406-5407.
8. Tian, N.; Zhou, Z.-Y.; Yu, N.-F.; Wang, L.-Y.; Sun, S.-G., Direct electrodeposition of tetrahexahedral Pd nanocrystals with high-index facets and high catalytic activity for ethanol electrooxidation. *Journal of the American Chemical Society* **2010**, *132* (22), 7580-7581.
9. Molnar, A., Efficient, selective, and recyclable palladium catalysts in carbon– carbon coupling reactions. *Chemical reviews* **2011**, *111* (3), 2251-2320.
10. Yin, L.; Liebscher, J., Carbon– carbon coupling reactions catalyzed by heterogeneous palladium catalysts. *Chemical Reviews* **2007**, *107* (1), 133-173.
11. Miyaura, N.; Suzuki, A., Palladium-catalyzed cross-coupling reactions of organoboron compounds. *Chemical reviews* **1995**, *95* (7), 2457-2483.
12. Wang, C.; Chen, Y.; Feng, S.; Zhang, N.; Shen, L.; Zhang, K.; Yang, B., The preparation of hollow Fe₃O₄/Pd@C NCs to stabilize subminiature Pd nanoparticles for the reduction of 4-nitrophenol. *New Journal of Chemistry* **2020**, *44* (12), 4869-4876.
13. Liu, S.; Guo, M.-X.; Shao, F.; Peng, Y.-H.; Bian, S.-W., Water-dispersible and magnetically recoverable Fe₃O₄/Pd@ nitrogen-doped carbon composite catalysts for the catalytic reduction of 4-nitrophenol. *RSC advances* **2016**, *6* (80), 76128-76131.
14. Guarnizo, A.; Angurell, I.; Muller, G.; Llorca, J.; Seco, M.; Rossell, O.; Rossell, M., Highly water-dispersible magnetite-supported Pd nanoparticles and single atoms as excellent catalysts for Suzuki and hydrogenation reactions. *RSC advances* **2016**, *6* (73), 68675-68684.
15. Fishbein, L., Aromatic amines. In *Anthropogenic compounds*, Springer: 1984; pp 1-40.
16. Akindoyo, J. O.; Beg, M.; Ghazali, S.; Islam, M.; Jeyaratnam, N.; Yuvaraj, A., Polyurethane types, synthesis and applications—a review. *Rsc Advances* **2016**, *6* (115), 114453-114482.
17. Zhao, P.; Feng, X.; Huang, D.; Yang, G.; Astruc, D., Basic concepts and recent advances in nitrophenol reduction by gold-and other transition metal nanoparticles. *Coordination Chemistry Reviews* **2015**, *287*, 114-136.
18. Munnik, P.; de Jongh, P. E.; de Jong, K. P., Recent developments in the synthesis of supported catalysts. *Chemical reviews* **2015**, *115* (14), 6687-6718.

19. Baig, R. N.; Varma, R. S., Magnetic silica-supported ruthenium nanoparticles: an efficient catalyst for transfer hydrogenation of carbonyl compounds. *ACS Sustain. Chem. Eng* **2013**,*1*, 805-809.
20. Tauster, S.; Fung, S.; Garten, R. L., Strong metal-support interactions. Group 8 noble metals supported on titanium dioxide. *Journal of the American Chemical Society* **1978**,*100* (1), 170-175.
21. Baker, R.; Prestridge, E.; Garten, R., Electron microscopy of supported metal particles: I. Behavior of Pt on titanium oxide, aluminum oxide, silicon oxide, and carbon. *Journal of Catalysis* **1979**,*56* (3), 390-406.
22. Dwyer, D.; Robbins, J.; Cameron, S.; Dudash, N.; Hardenbergh, J., Strong Metal–Support Interactions; Baker, RTK, Tauster, SJ, Dumesic, JA, Eds. American Chemical Society: Washington, DC: 1986.
23. Uchijima, T., SMSI effect in some reducible oxides including niobia. *Catalysis today* **1996**,*28* (1-2), 105-117.
24. Saifullah, M. S.; Ganesan, R.; Lim, S. H.; Hussain, H.; Low, H. Y., Large area sub-100 nm direct nanoimprinting of palladium nanostructures. *RSC advances* **2016**,*6* (26), 21940-21947.
25. Maeda, A.; Yamakawa, F.; Kunimori, K.; Uchijima, T., Effect of strong metal-support interaction (SMSI) on ethylene hydroformylation over niobia-supported palladium catalysts. *Catalysis letters* **1990**,*4* (2), 107-112.
26. d’Alnoncourt, R. N.; Friedrich, M.; Kunkes, E.; Rosenthal, D.; Girgsdies, F.; Zhang, B.; Shao, L.; Schuster, M.; Behrens, M.; Schlögl, R., Strong metal–support interactions between palladium and iron oxide and their effect on CO oxidation. *Journal of catalysis* **2014**,*317*, 220-228.

Chapter 9

Conclusions and future prospects

9.1 Conclusions

In this thesis, we present three aspects of nanoparticle synthesis. 1) A hydrocarbon based reducing agent for the synthesis of Au nanoparticles. The driving force of the Au^{3+} reduction is the reducing molecule attain aromaticity on sourcing H- species, and core-shell nanoparticles by solvent-less solid-state approach by coating a 2) surfactant based precursor, and 3) non-surfactant precursor over a pre-formed core followed by heat-treatment. Such an approach led to the formation of metal-shell coating over oxide core.

The Chapter 1 provides a broad introduction to the various synthetic aspects of gold nanoparticle and core-shell nanoparticles synthesis. Several characterization techniques and applications of the Au nanoparticles and core-shell nanostructures were also explained in this chapter. In chapter 2, the chemicals and characterization tools were listed, which were utilized for the synthesis and analysis of the materials.

Chapter 3 describes the design of a reducing agent and stabilizing ligand for the synthesis of Au nanoparticles was presented. Cycloheptatriene on losing H- converts to tropylium ion and the H- reduces Au^{3+} to Au in 3 minutes. The molar ratio of CHTE to Au^{3+} was 3:1. The tropylium ion formed acts as a weak ligand leading to the formation of Au nanoparticles of size 15 nm. The powder XRD for Au nanoparticles collected after centrifuging the reaction solution clearly indicate the Au phase. The ^1H NMR spectra of the reaction solution also clearly indicate the presence of tropylium ion. A spurious NMR peak at a higher value has been assigned to tropylium ion present on the surface of Au nanoparticles.

In chapter 4 to 6, the results of synthesis of $\text{Fe}_3\text{O}_4@\text{M}$ (M=Au, Ag, AuAg) nanostructures by solid-state approach are presented. A calculated amount of surfactant-based metal precursor was added on to the pre-formed core followed by grinding. The grinding process aided by low melting behaviour of the precursor enable a smooth coating of the precursor onto the core. The resultant mixture was subjected to heat-treatment at 250 °C for 2 h in an autoclave resulting in the formation of core-shell nanoparticles. For testing the applicability of the method $\text{SiO}_2@\text{M}$ (M=Au, Ag, AuAg) core-shell nanostructures were also prepared and characterized for their structural and physical features.

In chapter 4, synthesis and characterization of $\text{Fe}_3\text{O}_4@\text{Au}$ nanostructures have been discussed. For this purpose, Au-TOAB precursor was used which in-turn was prepared by using a reported literature procedure. The Au-TOAB precursor was mixed with pre-formed Fe_3O_4 at room temperature by grinding for 10 min. After grinding process is completed, the resultant mixture was heat-treated at 250 °C for 2 h in an autoclave. The samples were cooled normally to room temperature and the as-synthesized samples were used for characterization purposes and catalysis experiments. Presumably, on decomposition, the Au-TOAB convert to Au which seems to show melting behaviour and thereby forming a metal coating over the Fe_3O_4 core. The ED-XRF shows that the initial feed ratio of metal is maintained in the products. The peak intensity of Au(111) increased with increasing precursor loading. The STEM and HR-TEM images confirmed the presence of the Au shell of thickness ~5-9 nm.

In chapter 5, synthesis and characterization of $\text{Fe}_3\text{O}_4@\text{Ag}$ nanostructures have been discussed. Silver N-lauryl sarcosinate precursor was used which in-turn was prepared by using a simple procedure. The surfactant based silver precursor was mixed with pre-formed Fe_3O_4 at room temperature by grinding for 10 min. After grinding process is completed, the resultant mixture was heat-treated at 250 °C for 2 h in an autoclave. The samples were cooled normally to room temperature and the as-synthesized samples were used for characterization purposes and catalysis experiments. Due to the decomposed gases, Ag which seems to show reduced state and thereby forming a metal coating over the Fe_3O_4 core. The ED-XRF shows that the initial feed ratio of metal is maintained in the products. The peak intensity of Au(111) increased with increasing precursor loading. The STEM and HR-TEM images confirmed the presence of the Ag shell of thickness ~5 nm.

In chapter 6, synthesis and characterization of $\text{Fe}_3\text{O}_4@\text{AuAg}$ nanostructures have been discussed. The precursor used in earlier studies (chapter 4 and chapter 5) were used for Au and Ag sources. The surfactant based precursors were mixed with pre-formed Fe_3O_4 at room temperature by grinding for 10 min. After grinding process is completed, the resultant mixture was heat-treated at 250 °C for 2 h in an autoclave. The samples were cooled normally to room temperature and the as-synthesized samples were used for characterization purposes and catalysis experiments. Both ED-XRF and XRD confirmed the alloy composition. The STEM and

HR-TEM images confirmed the presence of the Ag shell of thickness 5 nm. The SAXS patterns were sensitive to the composition especially at higher “q” confirming the alloy formation.

In chapter 7, the catalytic efficacy of the as-synthesized core-shell nanostructures were studied. The $\text{Fe}_3\text{O}_4@\text{Ag}$ and Ag-rich alloy catalysts synthesized in this study have shown high catalytic efficacy for hydrogen generation than $\text{Fe}_3\text{O}_4@\text{Au}$ and Au-rich alloy. Such a high catalytic efficacy has been found to be profound when a mixture of AB and NaBH_4 is used rather than employing the hydrogen sources individually. The magnetic recoverability and recyclability studies on $\text{Fe}_3\text{O}_4@\text{AuAg}$ -10:10 catalyst has demonstrated the efficient reusability of the catalysts even after 5 cycles.

In chapter 8, we have tested solid-state synthesis approach for non-surfactant based precursor, palladium acetate for the synthesis of $\text{Fe}_3\text{O}_4@\text{Pd}$ core-shell nanostructures. Pd nanoislands were observed to be formed on the surface of Fe_3O_4 . On increasing Pd content in the initial feed the number density of Pd islands increased and also resulted on the formation of a $\alpha\text{-Fe}_2\text{O}_3$ phase. From HR-TEM, an amorphous layer was observed which hindered the coalescence of Pd nanoislands. This observation was attributed to metal support interaction. At high Pd loading and high temperature, the Pd nanoislands coalesce to shell layer. The catalytic efficacy of $\text{Fe}_3\text{O}_4@\text{Pd}$ was tested for 4-nitrophenol reduction reaction and magnetic recoverability was also tested.

9.2 summary

The development of synthetic strategies for nanoparticles and cores-shell nanostructures is a continually progressing and evolving field. In this thesis, a solid-state solvent-less surfactant based metal precursor has been shown to be strategy which is highly scalable, eco-friendly and product composition control as per the initial feed ratio.

Though only a limited number of oxide core and metal precursor have been demonstrated, a numerous other oxides, sulphides, nitrides cores and other metal shells. Furthermore, this approach potentially reserves the possibility of those metal shells via forming their corresponding oxides followed by reduction. Such a strategy would be applicable for the oxides, whose reduction potential lie above that of hydrogen in the Ellingham diagram.

Furthermore, the versatility of the approach was also demonstrated for the cores having different shapes. The foundation behind application of materials is the compatibility. The functionalization and creating colloidal dispersion from core-shell nanostructures prepared by solid-state approach can push the applications of the materials beyond catalysis. As evident, the coating of metal shell over oxide core and controlling the thickness are challenging problems. It would be interesting to apply solid state approach reported in this thesis to metal coating on oxide thin-films. Further in-situ characterization would throw more light on the core-shell interface formation and properties.

List of Publications

1. Large Scale Solid-state Synthesis of Catalytically Active $\text{Fe}_3\text{O}_4@M$ ($M = \text{Au}, \text{Ag}$ and Au-Ag alloy) Core-shell Nanostructures
Srinivasa Rao Nalluri, Ravikiran Nagarjuna, Dinabandhu Patra, Ramakrishnan Ganesan and Gopalan Balaji

Scientific Reports (2019), 9:6603.
2. New gold standard: weakly capped infant Au nanoclusters with record high catalytic activity for 4-nitrophenol reduction and hydrogen generation from an ammonia borane–sodium borohydride mixture†,
Dinabandhu Patra, **Srinivasa Rao Nalluri**, Hui Ru Tan, Mohammad S. M. Saifullah, Ramakrishnan Ganesan and Balaji Gopalan

Nanoscale Advances 2020, 2, 5384–5395
3. Synthesis of Gold Nanoparticles: A Driving force towards aromaticity (under preparation)
Srinivasa Rao Nalluri, Dinabandhu Patra, Satish Bolloju and Balaji Gopalan
4. Catalytically active $\text{Fe}_3\text{O}_4@Pd$ nanostructures prepared by solid-state route (under preparation)
Srinivasa Rao Nalluri, Ravikiran Nagarjuna, Balaji Gopalan and Ramakrishnan Ganesan

Patent awarded:

1. A method for preparing core-shell nanoparticles, **Balaji Gopalan**, Ramakrishnan Ganesan, Nalluri Srinivasa Rao, Ravikiran Nagarjuna, **Indian Patent. Application No. 201611017377; Patent No. 328150. Date of Grant: 26/12/2019**

List of conferences

1. National Conference on Materials for Aerospace Applications, 2014.
BITS-Pilani, Hyderabad Campus during December 22, 2014

Magneto-plasmonic nanostructures for Bio-sensing

N. Srinivasa Rao, Hemanth, Avinash Panda, G. Balaji, Kannan Ramaswamy*

(Poster Presentation)
2. National Conference on Nano and Functional Materials, 2014.
BITS-Pilani, Pilani Campus during December 07-08, 2014

Synthesis, Characterization and Chemical Reactivity of CaO Nanoparticles

A. Rishi Vachaspathy, N. Srinivasa Rao, B. Satish, G. Balaji* (Poster

Presentation)
3. CRSI National Symposium, 2012, BHU-Varanasi, during February 01-03, 2012.
Synthesis of silver nanoparticles by using tartarate reduction method

N. Srinivasa Rao, G. Balaji* (Poster Presentation)

Bibliography of the Candidate:

Mr. Nalluri Srinivasa Rao was born in 1976 in Prakasham district A.P. In year 1999, he completed his Masters in organic chemistry from Andhra University, Vishakhapatnam, Andhra Pradesh. He has 21 years of teaching experience for IIT-JEE advance level and mains and other competitive examinations. In 2012, he joined BITS-Pilani Hyderabad campus for his Ph. D. Since April 2020 onwards, he is also working as a director cum faculty in chemistry in Valley Oak Classes, Hyderabad.

Bibliography of the Supervisor:

Dr. Balaji Gopalan was born on 24th March, 1973 at Kumbakonam, Tamil Nadu, India. After graduation in chemistry, he completed his M. Sc. (Chemistry) at Indian Institute of Technology, Madras in 1995. He completed his Ph. D. from Indian Institute of Technology, Kanpur in 2003 under the supervision of Prof. N. S. Gajbhiye. He was a Humboldt Postdoctoral fellow at Institute of Nanotechnology (INT), FZK Karlsruhe between 2004-2005. He continued as guest scientist 2005-2007. He had his second postdoctoral stint at CAMD, Louisiana State University for 2 years. Since 2010, he is working as a faculty at department of chemistry, BITS-Pilani Hyderabad Campus. He has published 21 papers and has a Indian patent to his credit.